Non-metal Doped TiO_2 Nanocomposites for the Removal of Nuclear Waste from Water

*A thesis submitted in partial fulfillment of the requirements for the degree of Master of Philosophy (*M.Phil.*) in Applied Chemistry and Chemical Engineering, University of Dhaka*

Submitted by

Name: Md. Mehedi Hassan

Registration No: 069

Session: 2019-2020

Department of Applied Chemistry and Chemical Engineering,

University of Dhaka

The thesis titled **"Non-metal Doped TiO_2 Nanocomposites for the Removal of Nuclear Waste from Water**" submitted by Registration No: 069, Session: 2019-2020 has been accepted as a partial fulfillment of the requirements for the degree of Master of Philosophy (M.Phil.) in Applied Chemistry and Chemical Engineering, University of Dhaka.

1. Dr. Md. Ashraful Islam Molla — Supervisor
Professor
Department of Applied Chemistry and Chemical Engineering
University of Dhaka.

2. Dr. Mithun Sarker — Co-Supervisor
Associate Professor
Department of Applied Chemistry and Chemical Engineering
University of Dhaka.

DECLARATION CERTIFICATE

This is to certify that Reg. No. 69/2019-2020, M.Phil. session-2019- 20, Department of Applied Chemistry and Chemical Engineering, University of Dhaka, Dhaka, Bangladesh, has carried out his M.Phil. thesis on "Non-metal doped TiO_2 Nanocomposites for the removal of nuclear waste from water" under our joint supervision. He has successfully completed his research work and ready to present his dissertation, which is required for the partial fulfillment of his M.Phil degree. The candidate did the work submitted here and no part of this thesis has been submitted elsewhere for any degree or diploma. The thesis contains no materials previously published or written by any other person except reference is made in the text of the thesis. We have gone through the final draft of the thesis and recommend its submission for the degree of Master of Philosophy in Applied Chemistry and Chemical Engineering.

ACKNOWLEDGEMENT

First of all, I express my sincere gratitude to the almighty and omnipresent Allah for His mercy in the successful completion of this thesis work.

My special thanks go to my supervisor, Dr. Md. Ashraful Islam Molla, Professor, Department of Applied Chemistry and Chemical Engineering, University of Dhaka. His constant supervision and spiritual encouragement throughout the entire period of my research work were instrumental in putting together this dissertation. His commitment to supervision appeared to me encouraging enough to move the research to the desired goal. Special thanks also go to him for providing all kinds of departmental facilities for my research work.

I am really indebted to my co-supervisor, Dr. Mithun Sarker, Associate Professor, Department of Applied Chemistry and Chemical Engineering, University of Dhaka. His continuous support, encouragement, helpful suggestions, and supervision inspired me to complete my thesis work and to write up my thesis successfully.

I am grateful to all my M.Phil. course Teachers and Professor Dr. Mohammad Nurnabi, Chairman, Department of Applied Chemistry and Chemical Engineering, University of Dhaka, for providing all necessary laboratory facilities for the smooth completion of this dissertation.

I would also like to express my heartwarming thanks to the head, scientist, and research fellow of the Center for Advanced Research in Sciences (CARS), the University of Dhaka, for helping me. It has helped me a lot in doing my thesis work.

The Author

10 July, 2025

ABSTRACT

This study focuses on the synthesis and evaluation of non-metal doped titanium dioxide (TiO_2) nanoparticles for the potential remediation of radionuclide-contaminated water. Undoped TiO_2 and doped TiO_2, e.g., B-doped TiO_2 (B–TiO_2), C-doped TiO_2 (C–TiO_2), N-doped TiO_2 (N–TiO_2) were successfully prepared by the sol-gel method. The resultant nanoparticles were thoroughly characterized by XRD, FESEM, EDX, TEM, FTIR, UV–Vis spectroscopy, DLS, zeta potential measurement, and AAS to study their structural, morphological, optical, and adsorption properties. Furthermore, batch adsorption and photocatalytic experiments using adsorbents were conducted to assess their efficiency in radionuclide removal. While attempting to extract radioactive isotopes from water, real radionuclides were not implemented due to safety, cost, and facility constraints. Instead, the nonradioactive analogs—cobalt, iodine, manganese, and zinc (which have similar radioisotopes, such as $^{60}Co^{2+}$, $^{131}I^{-}$, $^{54}Mn^{2+}$, and $^{65}Zn^{2+}$)—were employed, due to their similarity with the radioactive elements. XRD results revealed that both the doped and undoped TiO_2 were crystalline anatase, and B-doping led to the formation of a small amount of the rutile phase. Both SEM and TEM images showed that the morphology and particle dimension were influenced by doping, with the smallest average particle size being reached for C–TiO_2. The adsorption capacity was evaluated using iodine adsorption and the removal of metal ions. The C–TiO_2 and N–TiO_2 nanocomposites were found to show excellent adsorption properties among the doped samples, which may be due to a higher surface area and improved surface chemistry. The findings indicate that non-metal doping can enhance the photocatalytic and adsorption activity of TiO_2. Thus, these materials are promising candidates for treating radioactive wastewater.

TABLE OF CONTENTS

Contents

LIST OF FIGURES

LIST OF TABLES

CHAPTER 1:

INTRODUCTION

1.1 BACKGROUND

Radionuclides are radioactive isotopes of elements and compounds, which lose energy by emitting radiation in the form of alpha or beta particles, or gamma rays. These isotopes can be naturally occurring or anthropogenic in origin. Natural radionuclides such as uranium isotopes (^{238}U, ^{235}U), thorium-232 (^{232}Th), tritium (^{3}H), etc. Radionuclides are mainly generated inside nuclear reactors through nuclear fission, when heavy nuclei divide into smaller and less stable fragments. The important radionuclides for nuclear accidents are iodine-131 (^{131}I), cesium-137 (^{137}Cs), strontium-90 (^{90}Sr), and plutonium-239 (^{239}Pu). In addition, activated radionuclides are produced during reactor operation as a result of neutron activation of structural materials [1].

The main sources of radionuclide pollution in waterways are discharges from nuclear power plants, the manufacture or testing of atomic weapons, nuclear medicine facilities, and reprocessing plants. Metallic particles and cations, introduced into the reactor coolant system from particulate and cation sources in the solid, have the potential to deposit on the reactor piping and core surfaces, thereby becoming exposed to the neutron flux. This process leads to the creation of activated corrosion products, which are subsequently dissolved or particulate-bound and transported elsewhere in the reactor coolant system. Most of these, including longer-lived radionuclides such as cobalt-60 (^{60}Co), zinc-65 (^{65}Zn), silver-110m (^{110m}Ag), and manganese-54 (^{54}Mn), as well as short-lived isotopes such as cobalt-58 (^{58}Co), iron-59 (^{59}Fe), chromium-51 (^{51}Cr), and antimony-124 (^{124}Sb), are sources of greatest concern. Specifically, cobalt-60 (or ^{60}Co, one of the isotopes produced from the neutron activation of cobalt-59, which occurs naturally) is a significant long-term radiological hazard due to its long half-life and biological uptake [2].

These radionuclides can be released to aquatic environments near the reactor in case of a reactor accident, and they cause serious ecological contamination. Both aquatic organisms and fish are

especially prone to uptake the radionuclides, which can lead to radionuclide concentration levels in the aquatic food chain and pose a potential threat to human health through the ingestion of contaminated seafood. To cope with these environmental threats, nanocomposites have been developed as potential adsorbents for water cleanup from radioactive nuclides. Some nanocomposites exhibit good adsorption capacities and photocatalysis, making them applicable for nuclear waste treatment [3], [4], [5]. Among these, TiO_2 has been the center of attraction due to its chemical stability, low price, environmentally friendly nature, and excellent anti-corrosive properties. In particular, the anatase phase of TiO_2 has a high specific surface area per volume, thereby improving its adsorption capability and photocatalytic degradation [6].

Additionally, TiO_2 exhibits excellent photocatalytic activity under ultraviolet (UV) irradiation, which can effectively degrade organic pollutants and purify radioactive wastewater. But its visible light utilization is extremely confined because of its large band gap (~3.2 eV). To address this problem and improve the functionality of Fe-NC, extensive research has been conducted thus far on non-metallic doping [7], [8].

The photocatalytic activity of the TiO_2 can be improved greatly with the introduction of nonmetal elements, such as phosphorus (P), nitrogen (N), sulfur (S), boron (B), carbon (C), and silicon (Si) to the TiO_2 lattice. These dopants modify the electronic structure of TiO_2, decrease its band gap, create oxygen vacancies, and broaden its light absorption into the visible range. Accordingly, doped TiO_2 offers the advantages of improved charge separation, more photoactive sites, and greater photocatalytic and adsorption performance for removing radionuclides. Therefore, non-metal-doped TiO_2 nanocomposites are a promising sustainable material for the remediation of radionuclide-contaminated water [9], [10], [11], [12], [13], [14].

1.2 CURRENT STATE OF RADIONUCLIDES IN WATER

Radionuclide pollution of the world's water resources has become an environmental and public health concern. They have also been found in rivers, lakes, groundwater, and coastal waters worldwide, raising increasing concern about long-term ecological risks and human exposure [15].

Naturally occurring radionuclides, such as ^{238}U, ^{232}Th, ^{226}Ra, and ^{222}Rn, are introduced into aquatic systems through the dispersal process of geological weathering, erosion, and leaching of uranium and thorium from rocks and soils [16]. Groundwater, especially in regions of high natural radioactivity such as India, Finland, Brazil, and areas of Africa, may contain increasing levels of uranium and radon, sometimes exceeding the World Health Organization (WHO) guideline values for drinking water [17]. Such natural isotopes contribute to the background radiation of populations that use groundwater for drinking, particularly in rural and less-regulated regions. Artificial isotopic contamination has been an ongoing problem in the last century as a result of nuclear power production, nuclear weapons testing, medical isotope application and inadequate disposal of radioactive waste. Some of the significant man-made radionuclides frequently detected in water are ^{137}Cs, ^{90}Sr, ^{131}I, ^{3}H, and ^{239}Pu. Such isotopes are commonly released into the environment during the nuclear fuel cycle, reactor accidents, and leakage from facilities during storage [18].

The most serious such accident that occurred historically was the Chernobyl disaster in 1986, in which huge amounts of radionuclides were emitted and spread over Europe, depositing heavily in rivers and lakes [19]. Nor was the radioactive release into our air and seas so huge in Japan's Fukushima Daiichi disaster (2011) [20]. More than 1 million tons of treated radioactive water are currently being released from the Fukushima site into the ocean, prompting international concern about long-term marine radioactivity and food chain contamination.

There is also a long-term concern that stems from historical atmospheric nuclear weapons tests between 1940 and 1980. The global fallout from these activities was deposited into the hydrosphere. For example, isotopes of tritium and ^{137}Cs from this fallout can still be found in the surface and groundwater in many regions. Furthermore, the various medically applied radioisotopes, such as those used in medical diagnostics (^{131}I, ^{99}Tc) or those used in industrial processes, are mostly discharged into wastewater due to the lack of proper regulation in many countries. Eventually, these radionuclides can enter municipal sewage systems and later flow into natural water bodies, making a continuous contribution to cumulative contamination [21]. Recommended limits for radionuclides in drinking water (e.g., 0.1 Bq/L for ^{137}Cs and 1 Bq/L for ^{3}H have been proposed by international organizations such as the IAEA and the WHO. However, investigations indicate that levels of radionuclides in some developing countries remain above these concentrations in water supplies [22]. High levels of uranium and radium, for example, have been identified in drinking water wells in India, Pakistan, Egypt, and Bangladesh. In some developed nations, however, groundwater aquifers near nuclear institutions or uranium mines have already been found to be contaminated [23].

The accumulation of long-lived radionuclides in water bodies results in the chronic exposure of aquatic ecosystems and human populations. As they become integrated into the aquatic environment, these compounds can be bioconcentrated and/or bioaccumulated by aquatic organisms, eventually biomagnifying through the food chain, ultimately adversely affecting human health through the consumption of contaminated drinking water and seafood. Health problems include a higher rate of cancers, thyroid diseases, bone marrow failure, and loss of reproductive capacity [24].

1.3 AIMS AND OBJECTIVES OF THIS THESIS WORK

- ✓ To develop non-metal doped TiO_2 (B–TiO_2, C–TiO_2, and N–TiO_2) via a simple and scalable sol–gel method.
- ✓ To characterize the synthesized nanocomposites using XRD, FESEM, EDX, TEM, FTIR, UV-Vis spectroscopy, and AAS techniques.
- ✓ To evaluate and compare the adsorption and photocatalytic efficiency of doped and undoped TiO_2 in removing radionuclides from aqueous solutions.
- ✓ To study the influence of different non-metal dopants (B, C, and N) on the structural, morphological, and optical properties of TiO_2.
- ✓ To optimize conditions such as contact time, pH, and dosage for maximum radionuclide removal efficiency.
- ✓ To investigate the underlying photocatalytic mechanism and dopant-specific effects on TiO_2 activity.
- ✓ To assess the stability and potential for reusability of the synthesized nanomaterials in radioactive wastewater treatment.

CHAPTER 2:

LITERATURE REVIEW

2.1 RADIONUCLIDES AND THEIR TYPE

A radionuclide or radioactive nuclide is an unstable and unbalanced nucleus. A nuclide is defined by atomic number and neutrons number. Neutron number has a leading role in determining nuclear stability. A stable nucleus requires a neutron-to-proton ratio with a subtle neutron surplus. The nucleus becomes energetically unstable and loses extra energy in the form of decay processes including gamma ray or subatomic particle emission when this equilibrium is upset. This unstable condition is called a radioactive nuclide or radionuclide. They are also known as radioisotopes in industrial and scientific applications. Radionuclides have various applications in several industries such as agriculture, medicine, and water treatment and can either occur naturally or be artificially produced [25].

2.1.1 NATURAL RADIONUCLIDES

Natural radionuclides can be categorized into three main types depending on how they are formed: primordial radionuclides, secondary radionuclides, and cosmogenic radionuclides [26].

Primordial radionuclides are long-lived isotopes. They have existed since the Earth's formation. Examples include uranium-238 (^{238}U), thorium-232 (^{232}Th), and potassium-40 (^{40}K). These radionuclides are found in rocks, soil, water bodies, and living organisms. These enter natural ecosystems through weathering, erosion, and transport by water or wind. They play a significant role in natural background radiation and can impact ecological and human health if present in concentrations above global averages [27], [25].

Secondary radionuclides are formed from the decay of primordial radionuclides. These decay products, known as daughter nuclides, typically have shorter half-lives. Notable examples include

radium-226 (^{226}Ra), radon-222 (^{222}Rn), and actinium-228 (^{228}Ac). Part of the uranium and thorium decay series, they have essential applications but may also pose environmental and biological risks [5]. Cosmogenic radionuclides form as a result of cosmic rays colliding with and reacting in the Earth's atmosphere. Examples are carbon-14 (^{14}C), beryllium-10 (^{10}Be), and tritium (^{3}H). These isotopes are frequently used in dating and environmental studies [25], [28].

2.1.2 ARTIFICIAL (MAN-MADE) RADIONUCLIDES

Artificial radionuclides are produced through human activities, primarily in the nuclear power and defense sectors. Their presence in the environment primarily results from nuclear reactor operations, weapons testing, and accidents. Nuclear reactors release radionuclides such as tritium (^{3}H), cesium-137 (^{137}Cs), carbon-14 (^{14}C), and strontium-90 (^{90}Sr) during operation and waste disposal, contaminating nearby ecosystems [29]. Atmospheric nuclear testing, especially during the Cold War (1945–1980), dispersed radionuclides like plutonium-239 (^{239}Pu), cesium-137 (^{137}Cs), and tritium (^{3}H) globally. Nuclear disasters, such as those at Chernobyl (1986) and Fukushima (2011), released vast amounts of radionuclides. Cesium-137 (^{137}Cs) was a major contaminant in both events, with long-term effects on soil, water, and biological systems [19], [21]. Iodine-131 (^{131}I), a short-lived isotope, posed immediate health risks following the Chernobyl incident. Other radionuclides, including strontium-90 (^{90}Sr) and ruthenium-106 (^{106}Ru), also caused widespread environmental contamination. Strontium-90 mimics calcium, accumulating in bones and potentially damaging tissues, while ruthenium-106 can disperse across long distances through the atmosphere [30].

Artificial radionuclides also play vital roles in industrial, medical, and research applications. For instance, cobalt-60 (^{60}Co) is utilized in cancer radiotherapy and radiography, americium-241

(^{241}Am) is found in smoke detectors, and iridium-192 (^{192}Ir) is employed in non-destructive material testing [31], [32], [33]. Although these applications are strictly regulated, mishandling or accidents can result in significant environmental and health hazards.

2.2 RISKS OF RADIONUCLIDE CONTAMINATION

Radionuclides released into the aquatic environment represent a serious concern due to their radiotoxicity, chemical reactivity, long half-lives, and bioaccumulation potential. Once introduced into water systems, these substances can migrate, persist, and enter food chains, posing long-term ecological and health hazards. Even at low concentrations, chronic exposure can result in cumulative biological effects, particularly in sensitive populations such as children, pregnant women, and aquatic organisms [34].

2.2.1 HUMAN HEALTH RISKS

Cancer Induction

Ionizing radiation from radionuclides is a recognized carcinogen. Iodine-129 (^{129}I) and Iodine-131 (^{131}I) are taken up by the thyroid gland, where they can cause thyroid cancer, particularly in children and adolescents with developing tissues [13]. Strontium-90 (^{90}Sr) mimics calcium and gets incorporated into bone, raising the risk of leukemia and osteosarcoma. Alpha emitters, such as plutonium-239 (^{239}Pu), when inhaled, can settle in the lungs, liver, and bones, resulting in lung and liver cancers due to high energy and localized damage from alpha particles [35].

Organ Damage

In addition to radiological effects, some radionuclides, like uranium (U), exhibit chemical toxicity. When ingested via contaminated water sources, uranium accumulates in the renal system,

particularly affecting the proximal tubules, and may result in chronic nephritis, kidney dysfunction, and tubular necrosis [36].

Genetic Mutations

Exposure to radiation can result in DNA strand breaks, chromosomal alterations, and point mutations. These genetic changes may lead to mutagenesis, raise the risk of inherited diseases, and cause reproductive issues, such as infertility and miscarriage. In embryos, these mutations can be transmitted as germline defects [37].

Developmental Disorders

Developing organisms, particularly fetuses and infants, are more susceptible to ionizing radiation due to increased mitotic activity and immature repair mechanisms. Prenatal exposure to radionuclides such as cesium-137 (^{137}Cs) and iodine-131 (^{131}I) has been associated with diminished cognitive function, neurological impairment, and lower IQ scores in children. Developmental exposure may also lead to growth retardation and behavioral abnormalities [38].

2.2.2 ECOLOGICAL AND ENVIRONMENTAL IMPACTS

Bioaccumulation and Biomagnification

Radionuclides released into water bodies are taken up by primary producers, such as algae, and subsequently transferred to invertebrates, fish, and ultimately top predators, including humans. This process of bioaccumulation and biomagnification results in increasing radionuclide concentrations throughout the food web. Top-tier species, including fish-eating birds and mammals, are particularly at risk [39].

Reproductive and Developmental Effects in Aquatic Fauna

Experimental studies have shown that exposure to radionuclides like uranium, cesium, and strontium can lead to reduced gamete viability, hormonal imbalances, embryonic deformities, and developmental delays in aquatic species such as zebrafish, amphibians, and crustaceans [40].

Population and Community-Level Effects

Extended pollution affects aquatic community structure by favouring more radiation-tolerant species, generally reducing species diversity and disrupting predator-prey relationships. This may undermine ecosystem services, such as water filtration, nutrient cycling, and food web dynamics, ultimately threatening ecosystem stability [41].

Sediment Contamination and Remobilization

Some radionuclides (e.g., plutonium-239, americium-241, and cesium-137) are strongly attached to sediment grains and can survive in river beds, lakes, and coastal sediments for dozens of years. Environmental disturbances (such as flooding, dredging, or bioturbation) disturb these grains and release the radionuclides into the water column and re-circulate ecological dangers years after the source contamination episode [42].

2.3 MECHANISMS OF RADIONUCLIDE TRANSPORT AQUATIC ENVIRONMENTS

When radionuclides are released into aquatic environments, they undergo various physical, chemical, and biological processes that affect their mobility, speciation, bioavailability, and persistence in the environment. These modes of transport play a crucial role in determining how radionuclides behave in the environment and the potential impacts they may have on human health.

The interaction between these processes determines if the radionuclides get localized or dispersed over great distances.

2.3.1 ADVECTION AND DISPERSION

Advection refers to the transport of radionuclides through the bulk movement of water, typically driven by currents, tides, or river flows. This mechanism facilitates the movement of both dissolved radionuclides and those associated with particulates over considerable distances. On the other hand, dispersion processes – encompassing molecular diffusion and turbulent mixing – lead to the movement of radionuclides from regions where they are concentrated to areas with lower concentrations. Although dispersion can dilute contamination, it often results in broader environmental dissemination, increasing the geographical scope of potential exposure [42].

2.3.2 SORPTION AND DESORPTION

Sorption is a critical process that influences the retention or mobility of radionuclides. It involves two primary mechanisms: adsorption (binding to surfaces) and ion exchange. Cesium-137 (^{137}Cs) is well-known for its strong adsorption onto clay minerals, particularly illite. Uranium (U) shows an affinity for iron and manganese oxides, with its sorption efficiency influenced by pH, redox conditions, and ionic strength [43]. Conversely, alterations in chemical conditions such as acidification, increased competing cations (e.g., potassium or calcium), or organic matter enrichment can initiate desorption, remobilizing radionuclides previously immobilized in sediments or suspended matter [44].

2.3.3 COMPLEXATION WITH LIGANDS

Radionuclides frequently form aqueous complexes with various ligands, significantly enhancing their solubility and transport potential. Carbonates, sulfates, and phosphates create stable complexes with radionuclides such as uranium (UO_2^{2+}), plutonium, and neptunium. Organic ligands, including humic and fulvic acids, can produce soluble organometallic complexes with americium and europium, facilitating mobility even in low-flow environments [45]. Highly mobile species include pertechnetate (TcO_4^-), a technetium compound recognized for its environmental persistence and weak sorption capacity [46].

2.3.4 REDOX-DRIVEN SPECIATION

Redox potential (Eh) significantly influences the chemical forms and behaviors of radionuclides. Under oxidizing conditions, uranium is present as soluble U(VI), while in reducing environments, it precipitates as insoluble U(IV). Plutonium (Pu) can exist in several oxidation states (III, IV, V, VI), each exhibiting unique solubility and mobility traits. In anoxic sediments, redox shifts can convert mobile radionuclides into less soluble variants, facilitating natural attenuation. Nonetheless, redox fluctuations caused by human activities or climate change can lead to the reoxidation and remobilization of these contaminants [47], [48].

2.3.5 COLLOIDAL TRANSPORT

Colloids—particles sized between 1 and 1000 nm—act as a highly effective medium for radionuclide transport. These particles can include:

- Clay minerals
- Iron and manganese hydroxides

➢ Dissolved organic matter

Specific radionuclides, such as plutonium and americium, predominantly exist in colloidal forms within contaminated groundwater, enabling long-distance movement through aquifers and rivers. The ability of colloids to evade natural filtration processes poses significant challenges for remediation strategies and predictive modeling [49].

2.3.6 BIOACCUMULATION AND BIOMAGNIFICATION

Radionuclides can bioaccumulate in aquatic organisms through direct uptake from water or indirectly through the food chain. Strontium-90 (^{90}Sr) mimics calcium, integrating into the bones and exoskeletons of aquatic organisms [50]. Iodine-131 (^{131}I) preferentially accumulates in thyroid tissues, impacting endocrine function [51]. Cesium-137 (^{137}Cs) mimics potassium and can be found in the muscle tissues of fish [52]. Once inside organisms, these radionuclides can biomagnify, increasing concentration at each trophic level. This poses serious long-term risks to predators, including humans, who consume contaminated seafood, thereby extending the impact of radionuclide pollution across terrestrial ecosystems.

2.4 TREATMENT FOR RADIOACTIVE WASTEWATER

With fossil fuels being non-renewable and renewable sources still insufficient to meet global demands, nuclear energy is emerging as a viable alternative [53], [54], [55]. However, the expansion of nuclear power plants has resulted in a significant increase in radioactive wastewater generated from reactor operations and the use of radioisotopes. The composition and radioactivity levels of such waste vary depending on the nuclear processes involved. If left untreated, dissolved

radionuclides can enter the hydro-ecological cycle, contaminating rivers and groundwater and raising the potential for human and ecological exposure [56], [57], [58].

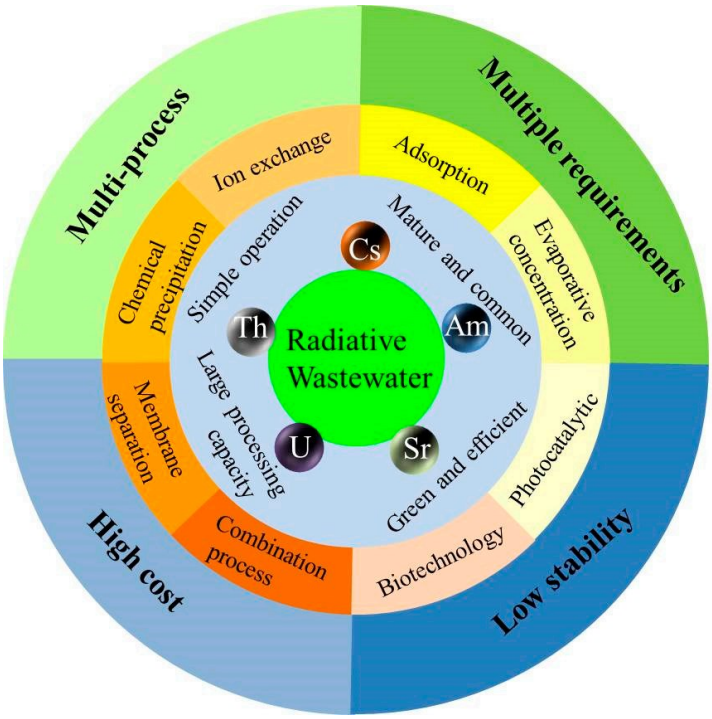

Figure 1: Treatment of radioactive wastewater [59]

Effective treatment of radioactive wastewater is crucial for mitigating environmental and health risks. The primary objective is to remove radioactive components through physical and chemical separation processes. Conventional treatment methods include chemical precipitation [60], electrolysis [61], and sulfide precipitation [62], which aim to extract radionuclides without significantly altering their chemical structure. Other widely used techniques include adsorption [63], [64], ion exchange [65], evaporation solidification [66], and membrane separation [67]. Additional methods involve flocculation, biological absorption, and microbial enrichment, particularly using plant-based or microbial systems [59].

2.4.1 ION EXCHANGE MECHANISM

The ion exchange process works by replacing ions present in a solution with those attached to an ion exchange material, which is usually made of resins or certain inorganic substances. The process is highly applicable in treating wastewater with low salt content, where ionic radionuclides are left after going through initial processes such as flocculation and sedimentation [68]. Organic resins were used conventionally, but low radiation resistance, poor thermal tolerance, and high cost have led to the use of inorganic ion exchangers. Some of the materials used that exhibit improved chemical and radiation stability are zeolites, titanosilicates, and ammonium phosphomolybdates (AMPs). Ion exchange materials can be chemically modified to enhance selectivity. For instance, incorporating sulfur into zeolites significantly increases their affinity for cesium ions (Cs^+). Key properties of an effective ion exchanger include high capacity, environmental stability, and regenerability [69].

2.4.2 CHEMICAL PRECIPITATION

Chemical precipitation continues to be one of the most widely used and cost-effective techniques for treating radioactive wastewater [70]. This process utilizes precipitating agents (e.g., aluminum salts, phosphates, iron salts, soda) to convert radionuclides into insoluble compounds such as hydroxides, carbonates, and phosphates, which can then be separated from the liquid. The effectiveness of this process is influenced by several factors, including the pH level, stirring speed, mixing duration, and the amount of reagent used. For instance, pH significantly affects the solubility of target radionuclides and the formation of precipitates. While effective for many radionuclides, chemical precipitation struggles to remove cesium, ruthenium, and iodine [71].

Specialized agents, such as cuprous chloride, can effectively eliminate radioactive iodine (I^-), even with short reaction times. Flocculation and sedimentation are typically used alongside precipitation to assist in separating the solid phase. However, this process often produces large volumes of radioactive sludge, which poses additional disposal and handling challenges [72].

2.4.3 MEMBRANE SEPARATION

Membrane separation is a versatile method that employs selective materials to separate components based on their size, charge, or other properties. This technology has been widely applied due to its effectiveness, flexibility, and relatively low power consumption [73]. Membranes are grouped according to pore diameters, and a few of them are used for the treatment of radioactive wastewater:

Microfiltration (MF): These cartridges retain bigger particles or macromolecules, typically between 0.1 and 1 μm. MF membranes have widespread use in pretreatment or filtration of large particles produced during radioactive effluent concentration.

Ultrafiltration (UF): With pore sizes ranging from 0.001 to 0.1 μm, these membranes are capable of removing suspended solids and colloidal particles from wastewater. Typically, ultrafiltration (UF) membranes are used as a preliminary treatment step before processes like reverse osmosis (RO).

Nanofiltration (NF): With pore sizes of approximately 1-2 nm, NF membranes are capable of selectively filtering certain ions, particularly multivalent ions, with smaller monovalent ions passing through.

Reverse Osmosis (RO): RO membranes are highly selective, rejecting a great many inorganic ions and organic contaminants. They apply differential pressure to force the solvent across the membrane, excluding most solutes.

In radioactive wastewater treatment, membrane separation proves beneficial in many ways. Unlike other energy sources such as evaporation, membrane separation can detoxify large quantities of contaminants, primarily ions like cesium (Cs^{+}), strontium (Sr^{2+}), and cobalt (Co^{2+}). Membrane systems can be designed for specific wastewater treatment applications. For instance, microfiltration removes suspended and large particles but does not eliminate dissolved radionuclides. Ultrafiltration further removes small colloidal matter and suspended particles, and can be combined with flocculation, for example, to increase the total efficiency of the process. Nanofiltration and reverse osmosis are preferable for removing dissolved ions and radionuclides from wastewater, such as strontium and cesium.

2.4.4 EVAPORATIVE CONCENTRATION

Evaporative concentration is an operation where radioactive wastewater is heated in an evaporator either by electric heaters or by steam to vaporize water. The vapor is finally condensed into concentrate containing non-volatile radionuclides. This concentrated waste can be solidified or further treated for safe disposal. The process reduces the volume of wastewater and effectively addresses waste that is rich in non-volatile radionuclides. It operates without adding chemicals, which minimizes secondary pollution [74].

Mechanical Vapor Recompression (MVR) improves energy efficiency by recycling condensed vapor to preheat incoming wastewater, thereby reducing energy use by up to 88.7% compared to

traditional systems [75]. Solar evaporation, which utilizes porous solar-driven sponge evaporators, has also been examined for energy-efficient operation. Limitations include high energy demand, inefficiency for volatile radionuclides (e.g., iodine, krypton), foam formation in acidic waste, and equipment corrosion, necessitating specialized designs and additional treatment steps [76].

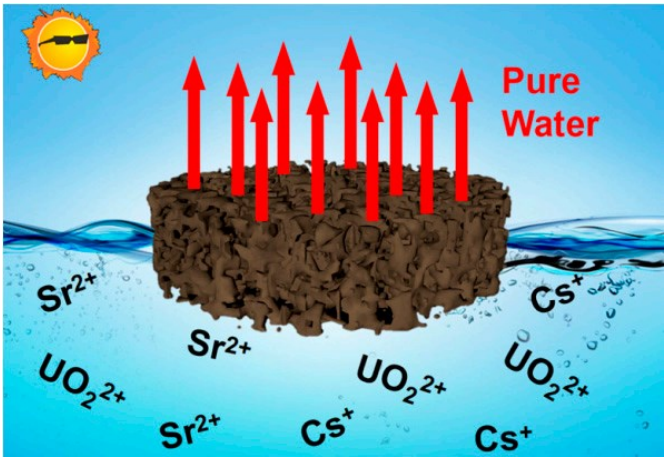

Figure 2: Efficient solar-driven evaporative radioactive wastewater treatment [76]

2.4.5 ADSORPTION

Adsorption removes radionuclides using porous materials classified into inorganic adsorbents (e.g., zeolites, activated carbon, bentonite), biomass-based adsorbents (e.g., cellulose, chitosan), and synthetic polymers (e.g., ion exchange resins) [77]. Zeolite is commonly used for cesium removal because of its low cost and multifunctionality. Recent advances include metal-modified nanocomposites and metal-organic frameworks (MOFs), which offer a large surface area and improved solidity. Examples include CoHCNF@polyaniline and NaCuHCF-functionalized magnetic adsorbents that exhibit strong cesium adsorption capacity. Traditional materials face challenges such as slow kinetics, low selectivity, and limited reusability. Modified clays have demonstrated improved uranium (UO_2^{2+}) removal, addressing some of these limitations [77].

2.4.6 BIOTECHNOLOGY

Biotechnology employs plants and microorganisms to treat radioactive wastewater through biotransformation, biosorption, bioaccumulation, sedimentation, and solubilization [78]. It is eco-friendly, energy-efficient, and prevents secondary pollution. Microbial colonies from uranium-rich environments exhibit high radionuclide removal rates, up to 92% for uranium and 100% for ^{241}Am and ^{137}Cs. Bacillus subtilis has proven effective in removing strontium (Sr^{2+}) from low-level radioactive waste [79]. Despite its advantages, limitations exist, including microbial sensitivity to radiation, which restricts application in high-radiation contexts. Nevertheless, biotechnology remains a cost-effective and sustainable option for radioactive wastewater management.

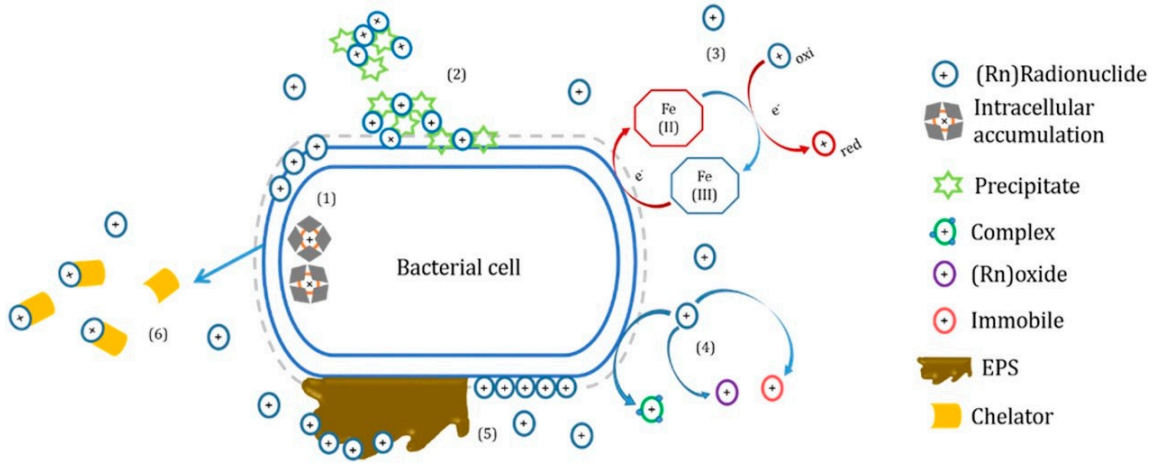

Figure 3: The mechanism of biological treatment of low-level radioactive waste liquid [78]

2.5 NANOTECHNOLOGY IN NUCLEAR WASTE MANAGEMENT

One of the major challenges linked to the advancement of nuclear power and weaponry is managing nuclear waste, which requires efficient recycling techniques and secure disposal

solutions. Nuclear waste is typically divided into low-level, intermediate-level, and high-level types, each needing its own distinct treatment and disposal approach [80]. Although conventional techniques have shown relative effectiveness, they come with drawbacks such as the potential for leakage, environmental contamination, and high monitoring costs [81], [82], [83]. As researchers seek more effective and sustainable methods, nanotechnology has surfaced as a potential breakthrough in the field of waste management [84], [85]. Nanomaterials provide low-cost, high-efficiency pollutant removal and reusable capabilities [86]. Previously utilized in fields like medical science and catalysis, nanomaterials are now regarded as superior for wastewater treatment due to their nanoscale size, large surface area, high reactivity, mobility, mechanical strength, porosity, hydrophilicity, dispersibility, and hydrophobicity [87], [88], [89]. Due to their large surface area relative to volume and distinctive physicochemical characteristics, nanomaterials greatly enhance the processes of containing, treating, and tracking radioactive waste [90], [91]. They have effectively removed heavy metals (e.g., Pb, Mo), organic and inorganic pollutants, and harmful microbes [92], [93], [94]. Nanomaterials such as nanoparticles (NPs), nano-adsorbents, and nanostructured barriers have shown promise in enhancing radioactive atom isolation, capture, and stability, providing a promising approach to mitigate risks in radioactive waste treatment [95], [96].

2.5.1 CLASSIFICATION OF NANOMATERIALS

Nanostructured materials are categorized based on their dimensional attributes, pore size, and structural composition. These classifications help in identifying suitable materials for specific applications in nuclear waste treatment and other fields.

2.5.1.1 CLASSIFICATION BASED ON DIMENSIONS

Zero-dimensional (0D) nanostructures consist of discrete nanoparticles (NPs), such as quantum dots, where all dimensions remain at the nanoscale and are spatially confined [97]. One-dimensional (1D) nanostructures include forms like nanowires, nanotubes, and nanorods. Because of their notably high aspect ratios, these materials are essential in the development of nanoelectronics and the manufacturing of sensors [98]. Two-dimensional (2D) nanostructures comprise thin films, nanosheets, and nanoplatelets, which are widely researched for their potential in flexible electronics and membrane separations [99]. Three-dimensional (3D) nanomaterials consist of interconnected 0D, 1D, and 2D components, forming polycrystalline, fibrous, or multilayered networks that are often used in composites and catalytic systems [100].

2.5.1.2 CLASSIFICATION BASED ON PORE SIZE

Microporous materials (pore diameter < 2 nm): Characterized by small pores and suitable for filtering tiny molecules and gases. Examples include Na-Y zeolites and natural clays [101], [102].

Mesoporous materials (2–50 nm): These materials accommodate larger molecules, making them ideal for adsorption and catalysis. Examples include MCM-41, SBA-15, and mesoporous carbon [103], [104].

Macroporous materials (> 50 nm): Known for their large pore sizes, they are suitable for biomolecular interactions and serve as support matrices. Examples include carbon microtubes and porous gels [104], [105].

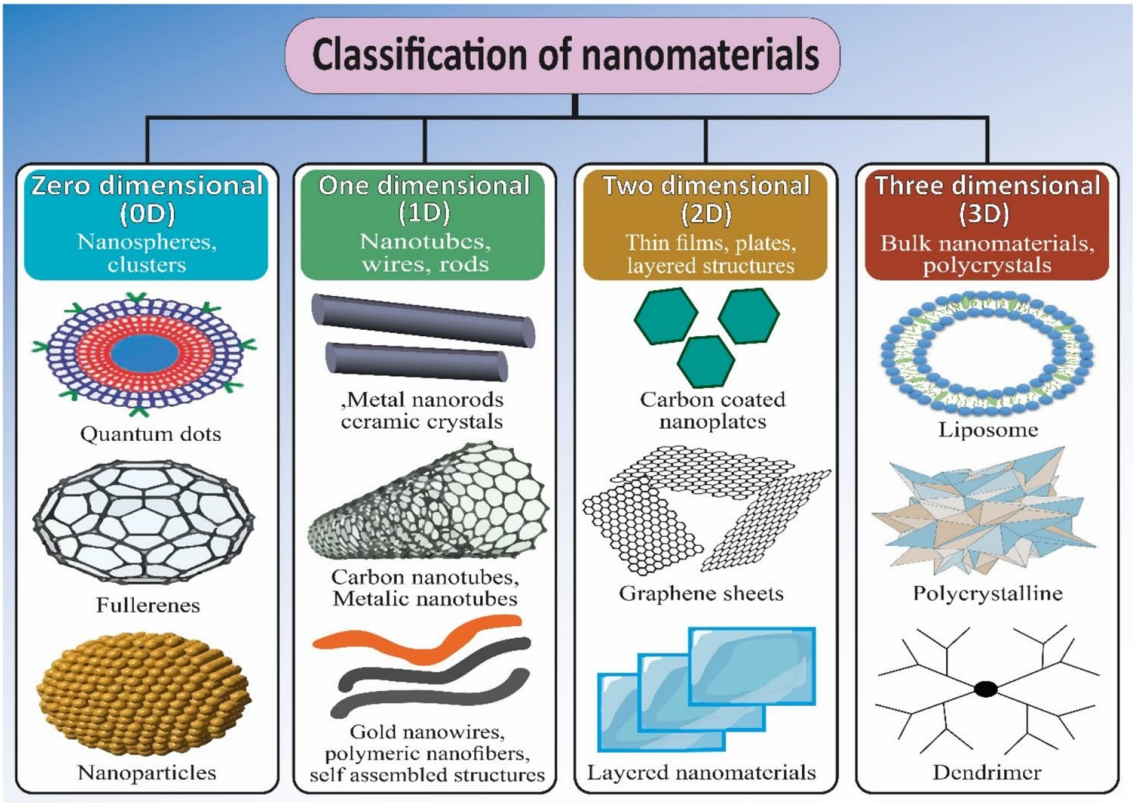

Figure 4: Classification of Nanomaterials based on dimensions [100]

2.5.1.3 CLASSIFICATION BASED ON STRUCTURE AND COMPOSITION

Carbon nanomaterials: Composed solely of carbon, this group includes materials such as graphene, carbon nanotubes (CNTs), fullerenes, carbon nanofibers, and carbon black, which are extensively valued for their mechanical durability and electrical conductivity [106], [107].

Metal and metal-oxide nanomaterials: They are known as inorganic nanomaterials, this category encompasses metallic nanoparticles (e.g., gold (Au), silver (Ag)) and metal oxides (e.g., iron oxide (Fe_3O_4), zinc oxide (ZnO)), with applications in sensing, adsorption, and magnetic separation [108], [109].

Organic nanomaterials: Composed of organic molecules, sometimes including inorganic cores, they are generally softer and more chemically tunable, with forms such as dendrimers and polymeric nanoparticles [110], [111].

2.5.2 CATEGORIES OF NANOMATERIALS USED IN RADIOACTIVE WATER DECONTAMINATION

2.5.2.1 CARBON-BASED NANOMATERIALS

2.5.2.1.1 CARBON NANOTUBES (CNTs)

Carbon nanotubes (CNTs) possess a high specific surface area, distinctive tubular nanostructures, and unsaturated carbon atoms that achieve stability by interacting with different atomic species [112]. These properties, along with high chemical stability under acidic conditions and superior heat and radiation resistance compared to organic exchange resins, make CNTs highly suitable for radioactive water treatment [113]. CNTs have been shown to effectively remove americium-243 [^{243}Am(III)] from aqueous media [114]. Multi-walled carbon nanotubes (MWCNTs), in particular, can adsorb uranium (U(VI)), facilitated by cation exchange between UO_2^{2+} and surface functional groups such as carboxyl (−COOH), carbonyl (−C=O), and hydroxyl (−OH) [115], [116]. The surface functional distribution and charge potential of MWCNTs depend on pH, affecting the adsorption of europium [Eu(III)] [117], [118]. Likewise, the adsorption of thorium [Th(IV)] is influenced by both CNT dosage and solution pH, with surface complexation being the primary mechanism [119]. CNTs function as electrically controlled ion exchangers, aiding in the elimination of radioactive cesium [Cs(I)] ions from wastewater. A novel electrochemical separation method using CuHCF/MWCNT hybrids has demonstrated selective removal of Cs(I), achieving a maximum adsorption capacity of 310 mg/g [120].

2.5.2.1.2 GRAPHENE OXIDE (GO)

Graphene oxide (GO) is a two-dimensional carbon-based nanomaterial structured in a hexagonal structure made up of sp^2-hybridized carbon atoms. It features oxygen-containing functional groups, such as carboxyl (–COOH), hydroxyl (–OH), carbonyl (–C=O), and hydroxymethyl (–COH), which act as active sites for binding radionuclides [121]. Boasting a specific surface area as large as 2630 m^2/g, GO offers considerable promise for the adsorption of radionuclides.

GO can be modified with different types of materials to improve its adsorption efficiency, dispersion, and resistance to aggregation, while promoting synergistic effects in complex wastewater environments. For instance, GO synthesized using a modified Hummers' method has shown considerable capacity to remove radionuclides such as Am(III), Th(IV), Pu(IV), U(VI), Sr(II), Tc(VII), and Np(V) from aqueous solutions [122]. The adsorption of U(VI) onto GO reaches a maximum capacity of 299 mg/g at pH 4.0, primarily through inner-sphere surface complexation rather than ion exchange [123], [124]. A comparison among GO, carboxylated GO (HOOC-GO), and reduced GO (rGO) revealed that their U(VI) adsorption capacities follow the order GO > HOOC-GO > rGO, emphasizing the importance of hydroxyl, carboxyl, and epoxy groups in improving sorption efficiency [125].

2.5.2.2 NANOSIZED METAL OXIDES

2.5.2.2.1 SILVER OXIDES (Ag_2O)

Silver oxide (Ag_2O) has a limited surface area and tends to aggregate, which reduces its effectiveness for radionuclide removal when used alone. However, attaching Ag_2O nanoparticles to substrates with large surface areas, such as $Mg(OH)_2$, enhances performance. The Ag_2O@$Mg(OH)_2$ nanocomposite showed removal efficiencies of 99.39% for UO_2^{2+} and 96.82%

for I^- within five minutes [126]. The nanoplate-like $Mg(OH)_2$ supports Ag_2O while stabilizing the solution's pH, effectively addressing the pH sensitivity of previous Ag_2O systems [127]. Furthermore, TiO_2-NAg_2O nano-adsorbents employed in a multi-stage micro-column system achieved removal rates of 94.7% for ^{60}Co and 92.0% for ^{65}Zn in simulated low-level radioactive wastewater [128].

2.5.2.2.2 IRON OXIDES (Fe_3O_4)

Iron oxide nanofibers and artificially produced hematite are capable of removing 90% of ^{131}I and 70% of ^{51}Cr from water through electrostatic adsorption [129]. These materials retain high selectivity for iodine, even in complex matrices containing Mn(II), Co(II), Ni(II), or Zn(II). In 1M HCl, removal efficiencies remain at 60.3% for ^{51}Cr and 54.9% for ^{131}I, indicating significant acid tolerance. Ferromagnetic Fe_3O_4 enables magnetic separation following treatment [130]. The Fe_3O_4@PPy nanocomposite demonstrated an iodide (I^-) adsorption capacity of 1627 mg/g at ambient temperature and can be conveniently separated using a magnetic field [131]. Likewise, Fe_3O_4@SiO_2 exhibited selective adsorption of U(VI) ions, achieving a capacity of 52 mg/g, and showed outstanding ability for regeneration [132].

2.5.2.2.3 MESOPOROUS SILICA

Mesoporous silica is valued for its high surface area, mechanical durability, and resistance to chemicals and radiation [133]. Materials such as MCM-41 and MCM-48 have demonstrated effective U(VI) adsorption through template-ion exchange [134]. Functional modifications enhance selectivity and capacity. For instance, MSU-H mesoporous silica modified with carboxymethylated polyethyleneimine (CMPEI) adsorbed U(VI) at a capacity of 153 mg/g at pH

4.0, reaching equilibrium in 10 minutes. After four months of treatment with polyacrylic acid, only about 1% of U(VI) was desorbed [135]. A uranyl ion-imprinted mesoporous silica (UIMS) also showed strong performance under radioactive and acidic conditions, with a capacity of 80 mg/g, rapid kinetics, and excellent stability and reusability [136].

2.5.2.2.4 TITANIUM DIOXIDE (TiO_2)

Nano-sized TiO_2 and titanate nanostructures are highly effective at removing radioactive cations from wastewater because of their resistance to radiation, chemical exposure, high temperature, and physical stress. For instance, nano TiO_2 demonstrates an adsorption capacity of 141±2 mg ^{99}Mo(VI) per gram, along with high radiochemical purity (≥97%) for TcO_4^- and radionuclide purity (≥99.99%) for 99mTc [137]. Wang investigated how nano TiO_2 adsorbs 60Co(II) ions in the presence and absence of humic substances [138]. The formation of inner-sphere complexes on the surface of nano TiO_2 promoted the adsorption of Pu(VI), regardless of the ionic strength [139]. The uptake of 60Co(II) ions varied with pH, suggesting that chemical adsorption or surface complexation played a major role [138]. Tan et al. noted that Eu(III) adsorption by nano TiO_2 occurred swiftly at pH six and slowly at pH 2–4 [140]. Furthermore, 94% of Th(IV) removal occurs via Ti–O–Th formation on nano TiO_2 at pH 4 [141]. Functionalizing nano TiO_2 with polyfunctional groups like TiO_2/PAAm–SSS led to an increased surface area, abundant functional sites, and improved efficiency in removing radionuclides. The experimentally observed adsorption capacities for radioactive Cs(I), Co(II), and Eu(III) were 120, 100.9, and 85.7 mg/g, respectively [142]. Nano TiO_2 possess a bigger surface area, porosity, stability, and ion exchange capability. After radioactive ion adsorption, titanate materials transition to a defined crystalline phase, which immobilizes nuclides and reduces secondary pollution risk. Crystalline silicotitanate products, like

IE910 and IE911, effectively remove 137Cs(I) from nuclear waste [143]. Moreover, titanate nanomaterials such as $Na_2Ti_3O_7$ and $Na_{1.5}H_{0.5}Ti_3O_7$ have been engineered to treat wastewater contaminated with radioactive isotopes like $^{137}Cs(I)$, $^{90}Sr(II)$, and $^{226}Ra(II)$. [144]. An important development is the Fe_3O_4@titanate core–shell nanocomposite, which demonstrates an adsorption capacity of 118.4 mg/g for Ba(II) [145]. They are highly effective in extracting radionuclides from wastewater which is polluted by nuclear leaks, and the treated water can be retrieved efficiently with the use of a basic magnetic separator.

2.6 STRATEGIES TO IMPROVE TiO_2 PERFORMANCE FOR RADIONUCLIDE REMOVAL

2.6.1 DOPING TiO_2 WITH METAL AND NON-METAL ELEMENTS

Increasing the photocatalytic property of TiO_2 through doping with different metal or non-metal elements is one of the earliest and most effective strategies. Doping change the electronic properties and bandgap of TiO_2, improving its photocatalytic efficiency under both UV range and visible light range. As a result, TiO_2 becomes more effective at degrading organic pollutants and removing inorganic contaminants, such as radionuclides, through adsorption, reduction, or complexation mechanisms.

2.6.1.1 METAL DOPING:

Metal doping of TiO_2 involves either the substitution of Ti^{4+} sites by metal cations or the induction of metal nanoparticles on the TiO_2 surface. These metal dopants alter the electronic structure, optical properties, and surface characteristics of TiO_2, thereby changing its photocatalytic behavior

[146]. The primary mechanisms through which metal doping enhances TiO_2 photocatalytic activity are as follows:

Bandgap Modification

A key way metal doping increases photocatalytic action of TiO_2 is by narrowing the bandgap. Transition metals like Pt, Ag, and Cu modify the energy levels of TiO_2's band gap. These impurity levels serve as electron donors or acceptors. As a result, this facilitates charge separation and reduces the excitation energy of electrons. As a result, these metals shift the optical absorption edge of TiO_2. This allows TiO_2 to be triggered under visible range illumination. Thus, TiO_2 has become much more functional in utilizing sunlight for photocatalytic purposes [147].

Enhanced Charge Separation

Generally, photocatalytic action involves photon-induced electron-hole generation on the TiO_2 surface. While these charge carriers help degrade pollutants, recombination between charges occurs very quickly, limiting TiO_2 efficiency. Metal doping enhances charge separation, addressing this issue. Metal dopants act as electron traps, capturing free electrons. Also, it prevents electrons from coalescing with holes. This prolongs the lifetime of electron–hole pairs, enabling them to participate more effectively in photocatalytic processes [148].

For example, an ideal metal dopant would be platinum (Pt) because of its high electron affinity. When doping TiO_2 with Pt, electrons are captured from the conduction band of TiO_2, which hinders recombination and ultimately maximizes photocatalytic activity [149].

Formation of Surface Plasmon Resonance (SPR)

If metal nanoparticles, such as Au, Ag, or Cu, are placed on the surface of TiO_2, they show surface plasmon resonance (SPR). Plasmon resonance simply means that the conducting electrons in metal

nanoparticles oscillate in concert with the impinging light. Plasmon resonance leads to the absorption of visible light and the formation of hot electrons, which are finally transferred to TiO_2. This good absorption and electron transference enable photocatalytic degradation of pollutants. However, significant effects are found during doping of TiO_2 with noble metals (Ag or Au) [150].

Enhanced Surface Area and Active Sites

Integrating metal nanoparticles with TiO_2 not only expands its surface area but also introduces extra active sites, enhancing its capacity to adsorb pollutants. Metals known for their noble characteristics, such as platinum, palladium, and gold, can create a stable interface with TiO_2, enhancing the surface assimilation of organic pollutants, inorganic pollutants, and radionuclides. An increased number of active sites boosts the overall photocatalytic performance of TiO_2, enabling it to break down a wider range of pollutants more effectively [151].

Modification of Surface Charge Distribution

The modification of TiO_2 surface properties by metal doping also alters the charge distribution, making it more or less attractive to interacting contaminants. Being noble in nature, metals like platinum or palladium can alter the TiO_2 surface potential to the advantage of adsorption of targeted pollutants. By modification of the surface charge distribution, doping of metal increases the affinity of TiO_2 toward pollutants and their subsequent photocatalytic degradation [152].

2.6.1.1.1 EFFECTS OF METAL DOPING ON TiO_2's PHOTOCATALYTIC PERFORMANCE

In general, how well TiO_2 works as a photocatalyst when doped with metals really depends on the specific metal used, how much of it is added, and the methods used to prepare it. Some essential considerations concerning metal doping of TiO_2 are:

Platinum (Pt) Doping

One of the most widely used metal dopants on TiO_2 is platinum. Adding platinum to TiO_2 helps boost its photocatalytic efficiency. It encourages better separation of electron-hole pairs and enhances its capacity to absorb visible light, making it more effective. Platinum nanoparticles or atoms act as electron traps, preventing recombination and thereby boosting the photocatalytic efficiency. TiO_2 doped with Pt exhibits markedly enhanced degradation of dyes, organic contaminants, and radionuclides such as Cesium-137 and Strontium-90. Additionally, Pt-doped TiO_2 shows higher stability under extended irradiation. That's why Pt-doped TiO_2 is suitable for continual environmental remediation processes [153].

Silver (Ag) Doping

Ag is a commonly used dopant for TiO_2 because it can improve the photocatalytic activity owing to the SPR effect. Silver nanoparticles are used on TiO_2 surface, where they absorb visible light and generate hot electrons that transfer into TiO_2's conduction band, thereby boosting the photocatalytic breakdown of harmful compounds. Additionally, the surface plasmon resonance (SPR) effect enhances TiO_2's ability to degrade organic pollutants efficiently, like dyes, and inorganic contaminants, such as radionuclides. It was found that the Ag-doped TiO_2 can enhance the adsorption of pollutants induced by visible light and could be applied in environmental research in which sunlight or low-energy light is employed [154].

Copper (Cu) Doping

Researchers have focused on increasing photocatalytic property of Cu-doped TiO_2, specifically for visible light photocatalysis. Cu-ions are helpful in trapping electrons. That's why they help inhibit charge recombination, thereby increasing photocatalytic performance of TiO_2. So, Cu-doping is

an efficient catalyst in organic pollutant degradation, such as phenols and pesticides. Copper is also capable of removing metal ions from wastewater and removing radionuclides. Additionally, Cu-doped TiO_2 is also more stable and recyclable, both of which are crucial in environmental cleanups [155].

Iron (Fe) Doping

Fe-doped TiO_2 has been of interest as it has the ability to increase photocatalytic property, especially in visible range. Iron ions (Fe) can substitute for Ti^{4+} within the TiO_2 lattice, introducing new electronic states into the bandgap that reduce its energy and enable photocatalytic activity under visible light [156]. Additionally, Fe-doped TiO_2 has been shown to improve the degradation of organic pollutants and heavy metals, including uranium (U) and various radionuclides [157].

2.6.1.2 NON-METAL DOPING:

Non-metal doping typically entails replacing oxygen atoms in the TiO_2 structure with non-metal elements such as nitrogen, sulfur, carbon, phosphorus, or fluorine. These substitutions influence TiO_2's electronic configuration, surface characteristics, and optical behavior. Although the exact ways non-metal doping enhances TiO_2 photocatalytic performance are complex, it generally occurs by:

Bandgap Narrowing

A common approach to increasing TiO_2's photocatalytic property using non-metal doping is by narrowing its bandgap. Since TiO_2's bandgap restricts its photodecomposition to ultraviolet (UV) light, reducing this gap allows for better utilization of visible light. This creates energy levels in the non-metal donors as crushed levels in the bandgap, requiring less activation energy from the valence band to excite electrons. For example, nitrogen doping in TiO_2 (TiO_2:N) introduces

impurity states close to the valence band, which facilitates absorption in the visible range light. If the bandgap drops, TiO_2 will regain significantly more from the solar spectrum, since it can now be photovoltaic in the visible region too [147].

Modification of the Electronic Structure

Non-metal dopants modify electronic configuration of TiO_2 by generating localized energy states within the bandgap or shifting the locations of the valence band edges and conduction band edges. Nitrogen-doped TiO_2 (TiO_2:N) exhibits an altered conduction band edge that enhances its capacity to absorb visible light. Adding non-metal dopants will increase the electron density in the TiO_2 system. This is good for charge transfer processes and therefore for photocatalytic activity as well [158].

Defect States and Oxygen Vacancy Formation

Incorporation of non-metal elements into the TiO_2 framework introduces the defect states and oxygen vacancies as active sites for the photocatalytic reaction. Oxygen vacancies are also electron traps that depress electron-hole recombination, producing hydroxyl radicals and superoxide ions, two reactive oxygen species known for the mineralization of organic and radioactive wastes [159].

Enhanced Charge Separation

The charge separation in TiO_2 can be affected by the non-metal additives. Non-metal dopants create impurity states and modify electron density, aiding in the separation of electron-hole pairs generated when TiO_2 is illuminated. This separation is vital for enhancing photocatalytic property, as recombination of electrons and holes significantly limits performance. Therefore, non-metal doping enhances charge mobility and reduces recombination losses [152].

2.6.1.2.1 EFFECTS OF NON-METAL DOPING ON TiO_2's PHOTOCATALYTIC PERFORMANCE

Different non-metal dopants affect the photocatalytic activity of TiO_2 depending on the type of dopant, the quantity used, and the synthesis technique. The following are some of the primary influences these dopants can have on TiO_2 performance.

Nitrogen (N) Doping

Nitrogen is commonly used for TiO_2 modification. By just replacing oxygen, nitrogen generates localized states in the TiO_2 lattice and modulates its bandgap, so changing its structure. N doping requires visible light to help excite electrons with reduced energy. Many groups have shown that this change greatly improves the breakdown of toxins, including heavy metals and organic compounds. For example, nitrogen enhanced the bulk electron density, which finally raised charge transferability and reduced electron-hole recombination times. The consequence shows that nitrogen-doped TiO_2 displays strong productivity in breaking down pollutants under visible light, making it suitable for air and wastewater treatment. The photocatalytic effectiveness of N-doped TiO_2 largely depends on the nitrogen concentration within its lattice, as a narrower bandgap and enhanced light absorption directly influence its performance. [160].

Sulfur (S) Doping

Popular among non-metal doping techniques is sulfur-doped TiO_2 (TiO_2:S). Sulfur increases TiO_2's capacity to absorb visible light by adding fresh electronic states, much as nitrogen does. Under visible light, sulfur substitute oxygen atom in TiO_2 to produce localized states that support electron excitation. Furthermore, sulfur doping helps to create oxygen vacancies, active sites for photocatalytic reactions. Studies show that sulfur-doped TiO_2 breaks down radioactive contaminants, heavy metals, and organic pollutants rather well. Furthermore, underlining TiO_2's

potential for practical applications, sulfur doping improves its stability and durability under continuous light exposure [161].

Carbon (C) Doping

Carbon, such as sp^2-hybridized carbon (graphitic carbon-like) and sp^3-hybridized carbon, may be doped within the TiO_2 lattice. The carbon dopant narrows the bandgap of TiO_2, making it possible for TiO_2 to photosensitize with more visible light, thus improving its energy conversion ratio. Conversely, carbon atoms act as electron donors, enhancing TiO_2's electrical conductivity and facilitating charge transfer. Furthermore, by incorporating TiO_2 with carbon, the pollutant adsorption capability of TiO_2 is promoted, which is an important criterion for air and water purification. C-doped TiO_2 has demonstrated outstanding activity under visible light and has effectively accelerated the breakdown of various organic contaminants. This, too, indicates that a broad range of radioactive elements can be stripped away, including, almost certainly, strontium as well as cesium. In general, C doped into TiO_2 may be a promising way to improve its photo-catalytic activity and stability in severe conditions (acidic/basic media) [162].

Phosphorus (P) Doping

Although phosphorus doping in TiO_2 is less frequently covered in research, it has shown notable enhancement in photocatalytic performance. Phosphorus atoms can integrate into the TiO_2 crystal structure and form Ti–P bonds. These Ti–P bonds effectively reduce band gap width and boost the material's absorption of visible range. Additionally, phosphorus encourages the formation of oxygen holes in the TiO_2 structure, which serve as active centers for the photocatalytic breakdown of contaminants. Phosphorus-doped TiO_2 has been demonstrated to be an effective photocatalyst

for eliminating both organic and inorganic pollutants, encompassing various organic compounds, heavy metals, and radioactive contaminants. [163].

Fluorine (F) Doping

F is considered a good photocatalyst for improved photocatalytic activity. The substitution of oxygen atoms in TiO_2 by fluorine produces defect states that enhance visible light absorption. The doping of fluorine improves the electronic properties of TiO_2, increases charge separation, and reduces effective charge recombination. Also, fluorine-doped TiO_2 is more stable. The material has demonstrated outstanding photocatalytic capabilities in degrading a wide range of organic pollutants and heavy metal contaminants. This leaves its ability for visible light absorption and for enhancing charge transfer properties, which is attractive for environmental remediation protocols [164].

2.6.2 FABRICATION OF TiO_2 NANOCOMPOSITES

2.6.2.1 TiO_2-GRAPHENE NANOCOMPOSITES

Graphene and graphene oxide are commonly employed to enhance TiO_2-based photocatalysts because they have excellent electric properties, a giant surface area, and metallic characteristics that facilitate efficient charge separation. The composite of TiO_2 and graphene forms a nanocomposite, which can effectively absorb a wider range of light, even visible light, and greatly enhance the photocatalytic activity [164].

Graphene/TiO_2 nanocomposites have been demonstrated to be effective adsorbents for various radionuclides such as Cs, U, and Sr from radioactive wastewater [165]. Graphene's extensive specific surface area gives abundant active sites for adsorbing radionuclides, and its layered

structural property promotes charge transfer, thereby reducing electron-hole recombination. Furthermore, the adsorption-treatment process demonstrated that the interface formed between GO and TiO_2 could enhance the stability of the composite, making it more suitable for long-term wastewater treatment.

2.6.2.2 TiO_2-CNTs NANOCOMPOSITES

Carbon nanotubes (CNTs) are extensively used to enhance photocatalytic properties of TiO_2. They have exceptional mechanical strength, high electrical property, and a giant surface area. As the composites are included in TiO_2, they will promote e-transport while the charge separation effect, both of them, can dramatically improve the activity of TiO_2 [166]. Composites of TiO_2 and CNTs have been successfully applied in the elimination of radionuclides, including cesium (Cs-137), cobalt (Co-60), and uranium (U-238). CNTs constitute the electron reservoir that forbids the recombination and promotes the decay of radionuclides. The elevated surface area of CNTs contributes to the composite's enhanced adsorption capacity when treating contaminated water [166].

2.6.2.3 TiO_2-ZEOLITE NANOCOMPOSITES

Zeolites are microporous substances characterized by extensive surface area and strong ion-exchange capabilities. Zeolites can be used in combination with TiO_2 to increase radionuclide adsorption and to promote the photodegradation process. Composites combining TiO_2 gel and zeolite have demonstrated enhanced efficiency in removing radionuclides like cesium (Cs) and strontium (Sr), attributed to the ion-exchange properties of zeolite alongside the photocatalytic activity of TiO_2 [167].

Zeolites can also secure TiO_2 to prevent it from aggregating and maintain a good surface area for pollutant adsorption. In addition, the ion exchange site can also interact with radionuclide ions in the zeolite, enhancing the removal efficiency of the composite [167].

2.6.2.4 TiO_2-POLYMER NANOCOMPOSITES

TiO_2 can be made a composite with polymeric materials (i.e., polyaniline, PANI), polypyrrole (PPy), and polythiophene (PTh) to improve the photocatalytic properties. The stability, dispersion, and charge transformation can be enhanced by introducing a polymer to TiO_2, making it considerably more available for photocatalysis [168]. In these composites, polymers serve as a stable matrix that prevents TiO_2 particle aggregation, thereby boosting photocatalytic efficiency. Additionally, polymer chains can interact with radionuclide ions, enhancing the composite's adsorption capacity and facilitating the degradation of radionuclides such as uranium (U) and thorium (Th). [168].

CHAPTER 3:

EXPERIMENTAL

3.1 MATERIALS

Before starting the experimental work, some critical considerations for material handling and environmental control are addressed:

- Utilized high-purity raw materials for synthesis and characterization.
- Maintained an appropriate work environment during synthesis.
- Took precautions with hydrophilic raw materials to prevent environmental exposure.
- Avoided compromise of material properties through controlled handling and storage.

3.1.1 TITANIUM DIOXIDE

The primary precursor of TiO_2 is:

Titanium (IV) Isopropoxide (TTIP)

3.1.2 DOPED TITANIUM DIOXIDE

The primary precursors for the doped TiO_2 materials are:

1. **For B-doped TiO_2 (B–TiO_2)**:
    - Boric Acid (H_3BO_3) as the boron dopant.
2. **For C-doped TiO_2 (C–TiO_2)**:
    - Glucose ($C_6H_{12}O_6$) as the carbon dopant.
3. **For N-doped TiO_2 (N–TiO_2)**:
    - Urea (NH_2CONH_2) as the nitrogen dopant.

3.2 MATERIAL SYNTHESIS

3.2.1 SYNTHESIS OF UNDOPED TiO_2 NANOPARTICLES

Initially, undoped titanium dioxide (TiO_2) nanoparticles were synthesized by the sol–gel process followed by calcination. In this case, no dopant was added in this preparation. 10 mL of titanium (IV) isopropoxide (TTIP) was used as the titanium precursor in a beaker. To this, 20 mL of ethanol and 5 mL of deionized water were added slowly under continuous stirring to ensure proper hydrolysis and condensation. The solution was heated at 50 °C with stirring. The mixing process lasted 3 hours, until the solution had turned into a powdery gel. The powdery gel was transferred in powder form to a crucible. The crucible was placed in an oven at 80°C for one hour to remove residual ethanol. After one hour of drying, the material was calcined at 450°C in an air atmosphere for 3 hours to form TiO_2 nanoparticles.

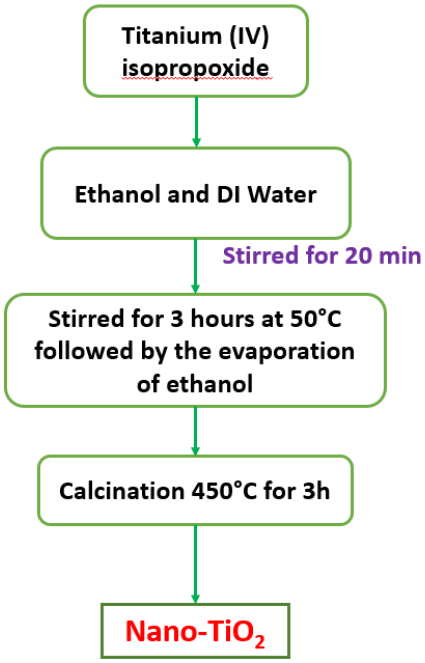

Figure 5: Sol-gel synthesis process of Nano-TiO_2 (Undoped)

3.2.2 SYNTHESIS OF 5% B-DOPED TiO_2 NANOPARTICLES

5% boron-doped TiO_2 nanoparticles were also synthesized using the sol-gel method with a calcination step. 0.34 grams of boric acid (H_3BO_3) was dissolved in 40 mL of ethanol in a beaker. 10 mL of titanium (IV) isopropoxide (TTIP), 20 mL of ethanol, and 5 mL of deionized water were then added slowly to the boric acid solution, with continuous stirring, to ensure homogeneous mixing and proper hydrolysis of the reagents. The solution was heated at 50°C with stirring. The mixing process lasted 3 hours, until the solution had turned into a powdery gel. The powdery gel was transferred in powder form to a crucible. The crucible was placed in an oven at 80°C for one hour to remove residual ethanol. After one hour of drying, the material was calcined at 450°C in an air atmosphere for 3 hours to form B-doped TiO_2 nanoparticles.

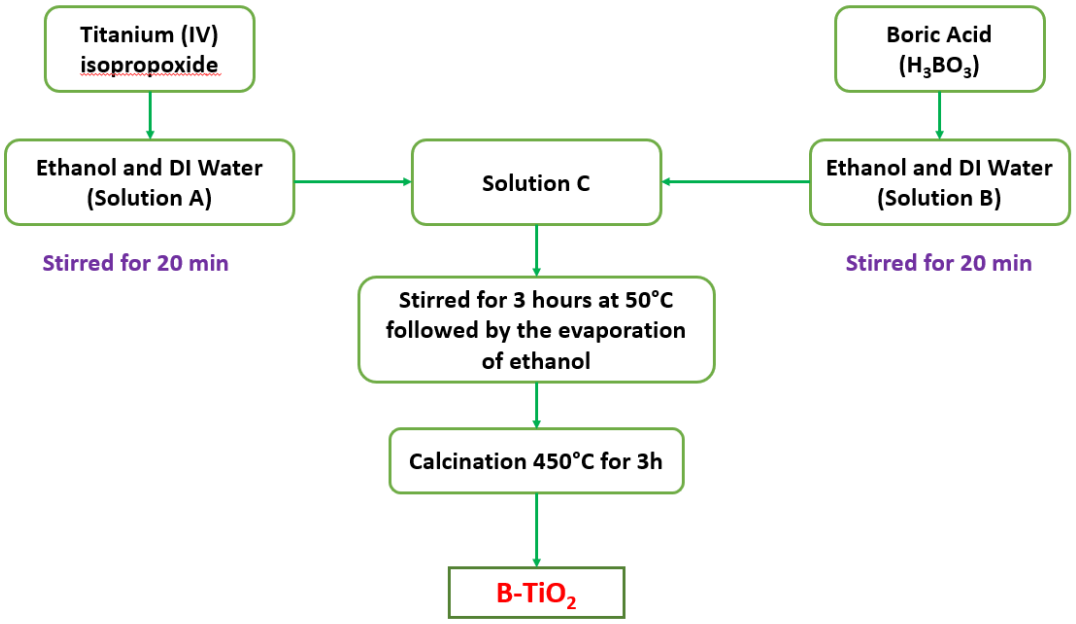

Figure 6: Sol-gel synthesis process of B-doped TiO_2

3.2.3 SYNTHESIS OF 5% C-DOPED TiO_2 NANOPARTICLES

5% carbon-doped TiO_2 nanoparticles were also synthesized using the sol-gel method, which included a calcination step. 0.325 grams of glucose ($C_6H_{12}O_6$) were dissolved in 40 mL of ethanol in a beaker to prepare the carbon precursor solution. 10 mL of titanium (IV) isopropoxide (TTIP), 20 mL of ethanol, and 5 mL of deionized water were then added slowly to the glucose solution, with continuous stirring, to ensure homogeneous mixing and proper hydrolysis of the reagents. The solution was heated at 50°C with stirring. The mixing process lasted 3 hours, until the solution had turned into a powdery gel. The powdery gel was transferred in powder form to a crucible. The crucible was placed in an oven at 80°C for one hour to remove residual ethanol. After one hour of drying, the material was calcined at 450°C in an air atmosphere for 3 hours to form C-doped TiO_2 nanoparticles.

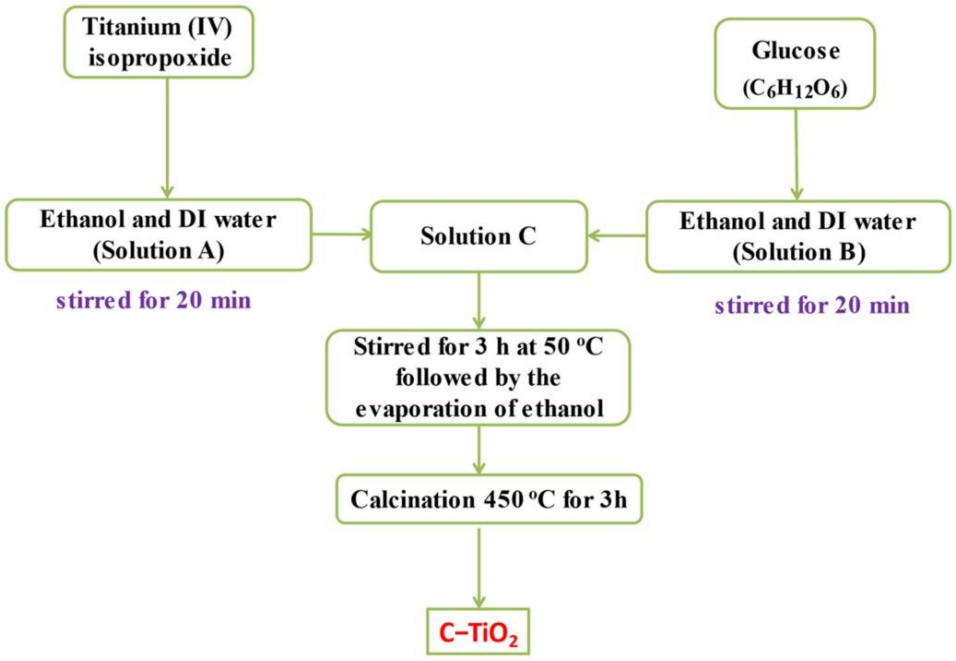

Figure 7: Sol-gel synthesis process of C-doped TiO_2

3.2.4 SYNTHESIS OF 5% N-DOPED TiO_2 NANOPARTICLES

Similarly, 5% nitrogen-doped TiO_2 nanoparticles were synthesized by the sol–gel process. Initially, 0.365 grams of urea (NH_2CONH_2) were dissolved in 40 mL of ethanol in a beaker to prepare the nitrogen precursor solution. Subsequently, 10 mL of titanium (IV) isopropoxide (TTIP), 20 mL of ethanol, and 5 mL of deionized water were added slowly to the urea solution under continuous stirring to ensure uniform mixing and proper hydrolysis. The reaction mixture was then heated and stirred at 50°C for 2–3 hours, until a powdery, gel-like substance formed. The resulting powder was transferred to a crucible and placed in an oven at 80°C for 1 hour to remove any residual ethanol content. Finally, the dried powder was calcined at 450°C for 3 hours in an air atmosphere to obtain the 5% N-doped TiO_2 nanoparticles.

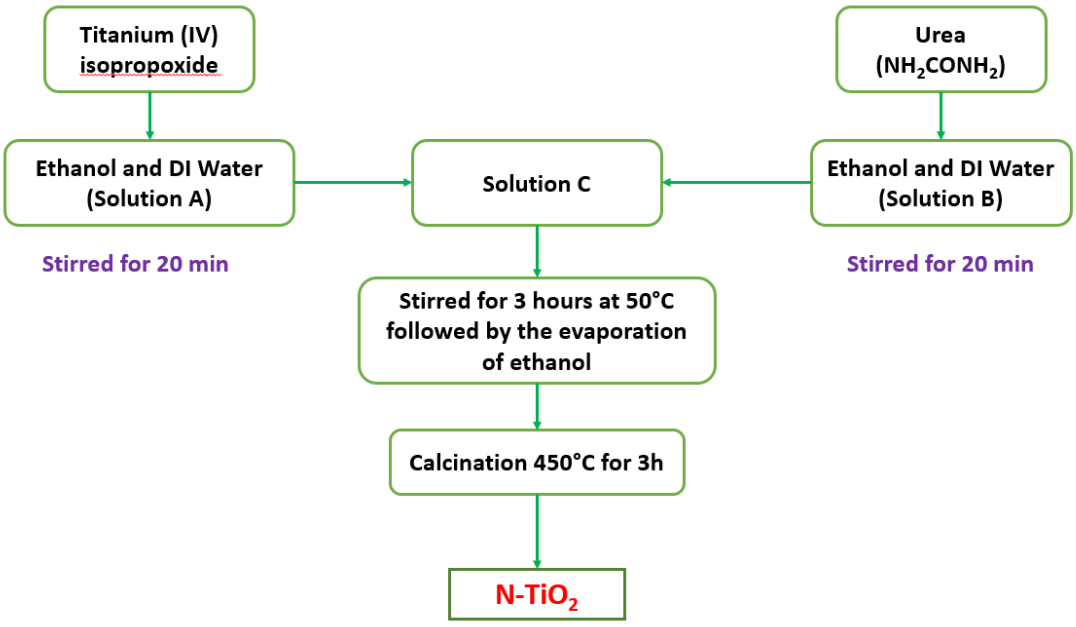

Figure 8: Sol-gel synthesis process of N-doped TiO_2

3.3 CHARACTERIZATION OF NANOMATERIALS

3.3.1 X-ray Diffraction (XRD) Analysis

X-ray diffraction analysis with the XRD (Ultima IV, Rigaku Corporation, Akishima, Japan) facility was conducted to characterize the crystal structures and phases of the prepared fine powders. The high-intensity Cu-K_α (λ = 1.5406 Å) radiation was focused on the sample in the scanning range from 10° to 80°.

X-ray diffraction (XRD) is a critical and relevant methods for identifying the atomic structure, phase composition, lattice constants, crystallite diameter, strain, and dislocation density of crystalline materials. XRD is classified as a non-destructive method. Its working principle is based on the application of Bragg's Law, which can be written as $2d_{hkl}\sin\theta = n\lambda$, (n=0,1,2…). Following this test, the diffraction patterns will always contain several peaks at various angles. These patterns are recognized based on their intensity and angle relations using the database of known structures. Sintering tends to cause some additional peaks to space due to impurities and/or undergo certain structural transformations. The average crystallite size (d) of synthesized powders in most cases is calculated from XRD patterns, applying the Scherrer formula: $d= K\lambda/\beta\cos\theta$, where k (the shape factor) is dimensionless and around 0.9, λ is the copper X-ray wavelength of 1.5406ºÅ, θ is the Bragg angle for the diff. peak and β is the FWHM of the peak.

3.3.2 SEM-EDX Analysis

The morphology and grain size of pellet samples were analyzed using a field emission scanning electron microscope (FE-SEM: JEOL JSM 7600F) operated at an acceleration voltage of 5 kV. Scanning electron microscopy (SEM) generates high-resolution images by directing a focused

electron beam across the sample surface. As these electrons interact with the atoms in the sample, they emit signals that reveal details about the sample's composition, surface topography, and other characteristics. The technique is very respected for its ability to produce three-dimensional images, magnification and high depth of field.

Energy Dispersive X-ray Spectroscopy (EDX) is an analytical method used to identify the elemental makeup of a sample and is commonly combined with SEM. When the sample is exposed to an electron beam, it emits characteristic X-rays that are detected and analyzed by the EDX system. Each element emits X-rays at unique energies, which allow for precise identification and quantification. In our study, EDX was utilized to verify the effective incorporation of dopants within the sample.

Figure 9: Field Emission Scanning Electron Microscope (FE-SEM: JEOL JSM 7600F)

3.3.3 TEM Analysis

Transmission Electron Microscopy (TEM) is a sophisticated characterization method in which the internal structure of a material can be probed at the nanoscale. In the current study, TEM analysis was performed on a ThermoFisher Scientific TEM (Model: Talos F200X G2). In contrast to Scanning Electron Microscopy (SEM), which primarily scans the surface, TEM operates by passing a high-energy electron beam through a very thin specimen. As electrons interact with the internal structure, they produce atomic to nanometer resolution images. Grain boundary observations, defects, lattice fringes, and crystallinity can be observed.

Selected Area Electron Diffraction (SAED), in combination with Transmission Electron Microscopy (TEM), was also employed to examine the crystallographic characteristics of the samples. In SAED, the diffracted electrons from crystal planes form ring or spot patterns, enabling the determination of interplanar distance and crystal structure. The presence of several concentric rings in SAED patterns suggests the presence of polycrystalline materials.

HR-TEM images were also analyzed by the Fast Fourier Transform (FFT) method utilizing the Digital Micrograph software. The FFT method transforms real-space lattice images into frequency-space information, thereby enabling the calculation of interplanar spacing and the indexing of individual crystal planes. Such analysis provides sufficient evidence of crystallinity and can identify any second phases in the nanoscale level.

TEM, when coupled with SAED and FFT, is a strong set of tools to investigate both the structural and crystallographic properties of nanomaterials and hence is extremely useful in materials science and solid-state electrolyte studies.

3.3.4 FTIR Analysis

Fourier-Transform Infrared Spectroscopy (FTIR) is a widely utilized analytical instrument to identify chemical bonds and functional groups in a material. FTIR measurement was conducted in the current study using a Shimadzu FTIR-8400S spectrophotometer (Shimadzu Corporation, Japan) to investigate the surface chemistry and nature of bonding of the synthesized samples. Spectra were recorded in wavenumber range 4000–400 cm^{-1}, and resolution was 4 cm^{-1}, and one spectrum was recorded with the summation of 30 scans for quality signal.

For sample preparation, 1 mg of finely powdered material was carefully blended with 100 mg of spectroscopic-grade potassium bromide (KBr) using an agate mortar and pestle. This homogeneous mixture was then compressed into a clear pellet using a hydraulic press, ensuring consistent transmission of infrared radiation through the sample.

FTIR functions by transmitting infrared light through a sample and measuring the intensity of absorption at various wavelengths. The absorption peaks in the FTIR spectrum correspond to the vibrational modes of chemical bonds within the material. Distinct functional groups—like hydroxyl (–OH), carbonate (CO_3^{2-}), or metal-oxygen (M–O) bonds—absorb IR radiation at characteristic frequencies, allowing their identification.

3.3.5 DLS Particle Size Distribution and ZETA Potential Analysis

Dynamic Light Scattering (DLS) was also used to find the particle size distribution and zeta potential of the as-synthesized samples using a Malvern Zetasizer (Model: ZEN3600, Malvern Instruments Ltd., UK). DLS measures the Brownian motion of suspended particles in a liquid and their hydrodynamic diameter from light scattering fluctuations.

To measure it, the sample was diluted as an aqueous dispersion with ultrasonication to avoid agglomeration. The instrument measures the intensity of scattered light to calculate the average particle size and size distribution, presenting the results as an intensity-weighted histogram.

Zeta potential measurements were also performed with the same instrument to assess the colloidal stability and surface charge of the particles. Higher absolute zeta potential values signify improved dispersion stability, resulting from stronger electrostatic repulsion among particles. The significance of this analysis is identifying the interaction behavior and stability of suspended nanoparticles in aqueous media, especially in aqueous applications.

3.3.6 UV-VIS Analysis

Ultraviolet–Visible (UV–Vis) spectroscopy was conducted using a HITACHI U-2900 spectrophotometer in order to find the optical adsorption characteristic and iodine adsorption property of the prepared TiO_2 samples, undoped and doped. The experiments were conducted between 190 and 400 nm.

All samples were placed in iodine solution, and UV–Vis spectra 60 minutes post-adsorption were measured to estimate the decrease in concentration of iodine. The distinctive absorption peak of iodine was tracked, with the reduction in its intensity used to evaluate the samples' adsorption capacity.

In addition, iodine adsorption plots for all the samples were obtained to examine their adsorption efficiency. Through this, surface activity and adsorption capacity of undoped and doped TiO_2 samples were achieved, which is needed in determining their effectiveness in adsorbing iodine from an aqueous solution.

3.3.7 AAS Analysis

Atomic Absorption Spectroscopy (AAS) was performed using a 240FS AA spectrometer (Agilent Technologies) to quantify the adsorption of metal ions onto the as-synthesized samples. AAS is highly sensitive for trace detection of metal ions in solution because of their light characteristic absorption.

For the adsorption experiment, previously known metal ion solution concentrations (e.g., Mn^{2+}, Co^{2+}, Zn^{2+}) were equilibrated with the doped and undoped TiO_2 samples. Following a fixed contact time, unadsorbed metal ion concentration in the solution was analyzed by AAS at their respective resonance wavelengths.

Adsorption efficiency was calculated by varying the concentration from the starting to the final. This approach gave exact and consistent data to screen the samples for their ion removal capacity, which is essential to determine their possible use in environmental remedial purposes.

CHAPTER 4:

RESULTS AND DISCUSSIONS

4.1 XRD

Figure 10 shows XRD patterns for the undoped TiO_2, B-doped TiO_2, C-doped TiO_2, and N-doped TiO_2 samples prepared using the sol-gel method. The undoped TiO_2 powder produced diffraction peaks at 25.367º, 37.053º, 37.909º, 38.667º, 48.158º, 54.051º, 55.204º, 62.28º, 62.867º, 68.976º, 70.479º, 75.277º, and 76.247º, corresponding to the crystallographic planes (101), (103), (004), (112), (200), (105), (211), (213), (204), (116), (220), (215), and (301), respectively.

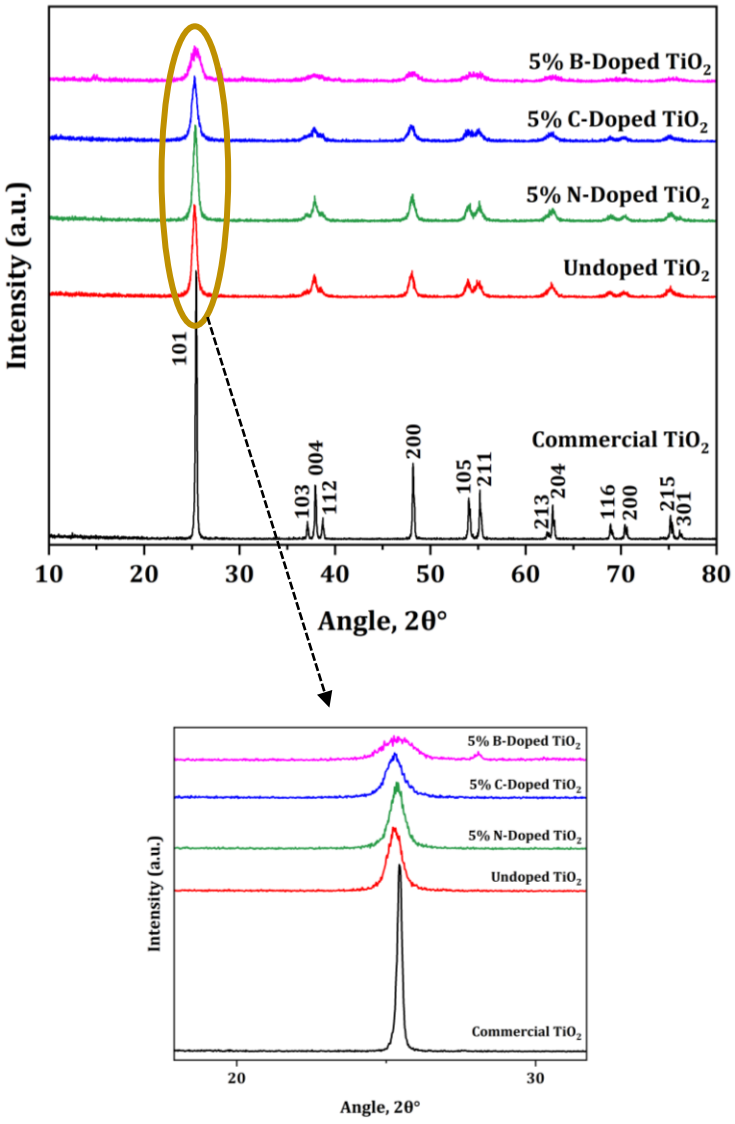

Figure 10: XRD Patterns of Commercial TiO_2, Undoped TiO_2, B-doped TiO_2, C-doped TiO_2, and N-doped TiO_2

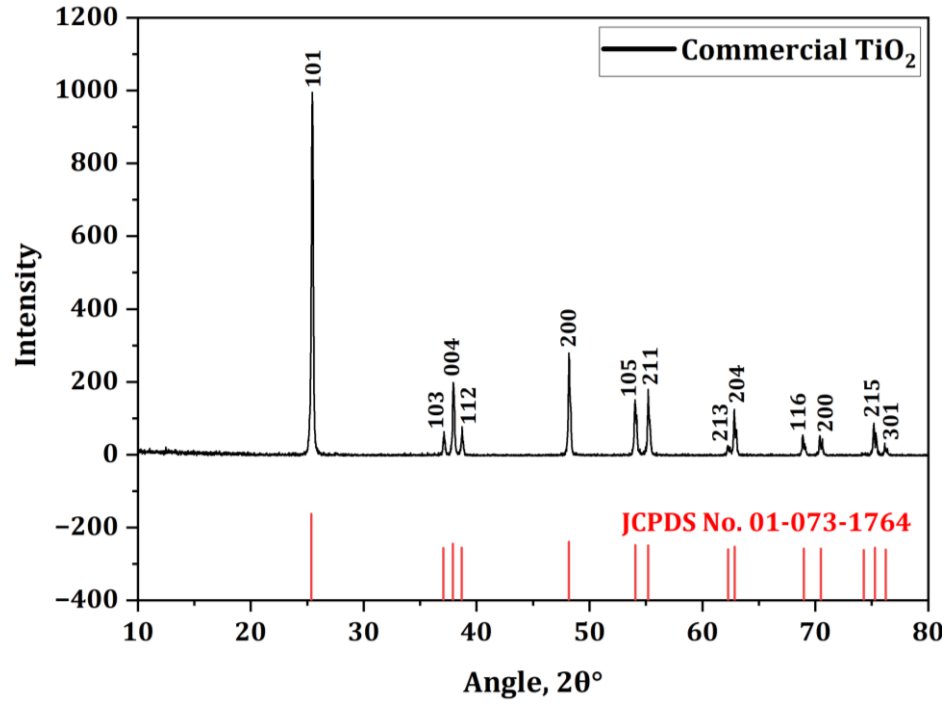

Figure 11: XRD Pattern of Commercial TiO_2 Compared with Standard Reference

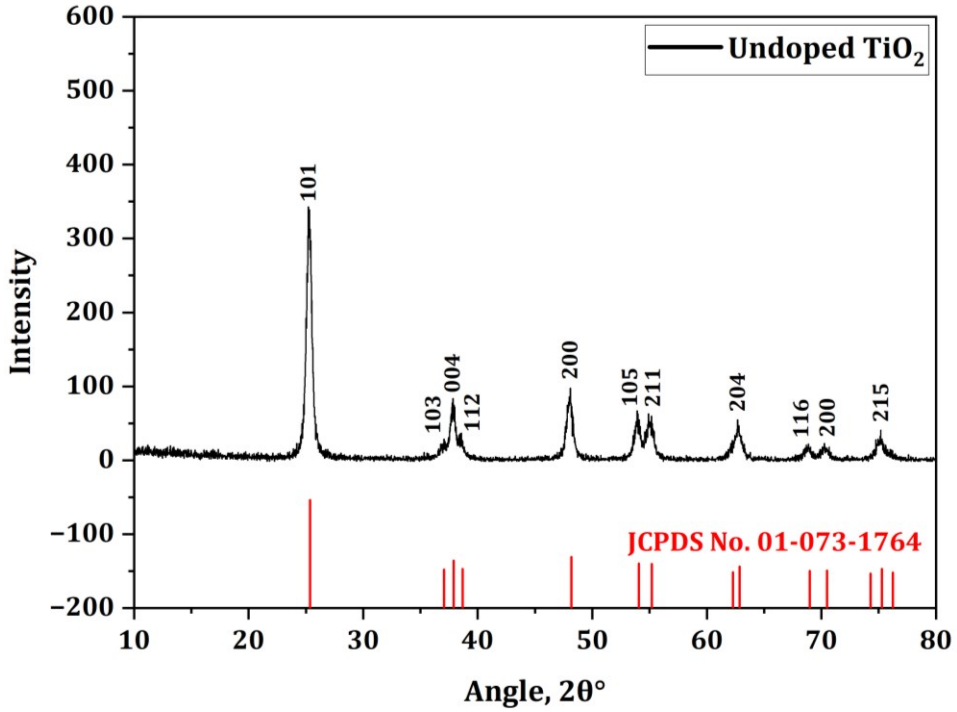

Figure 12: XRD Pattern of Undoped TiO_2 Compared with Standard Reference

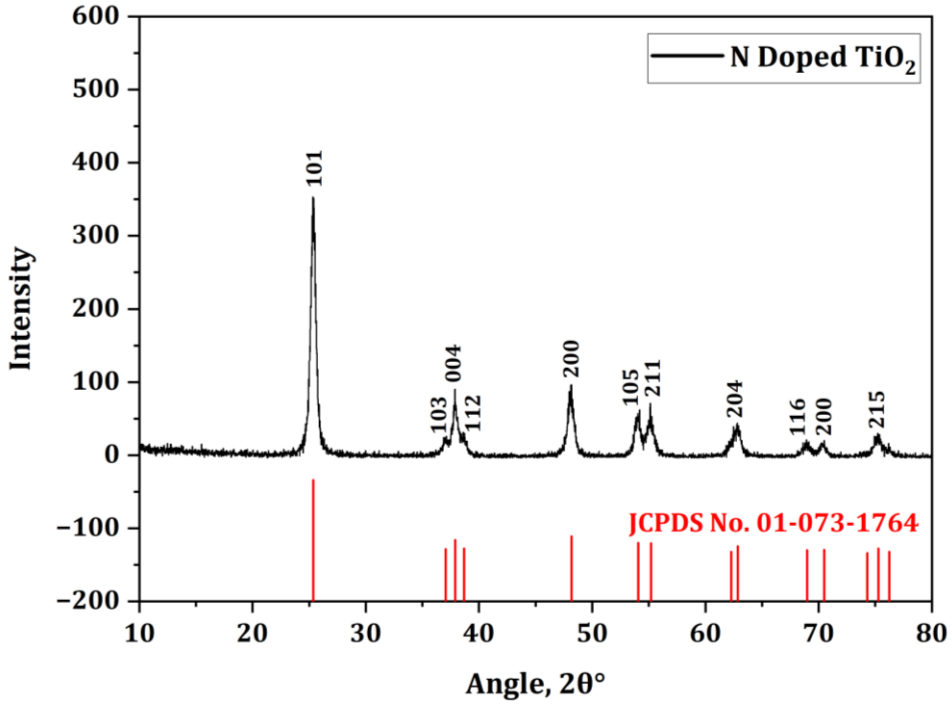

Figure 13: XRD Pattern of N-Doped TiO_2 Compared with Standard Reference

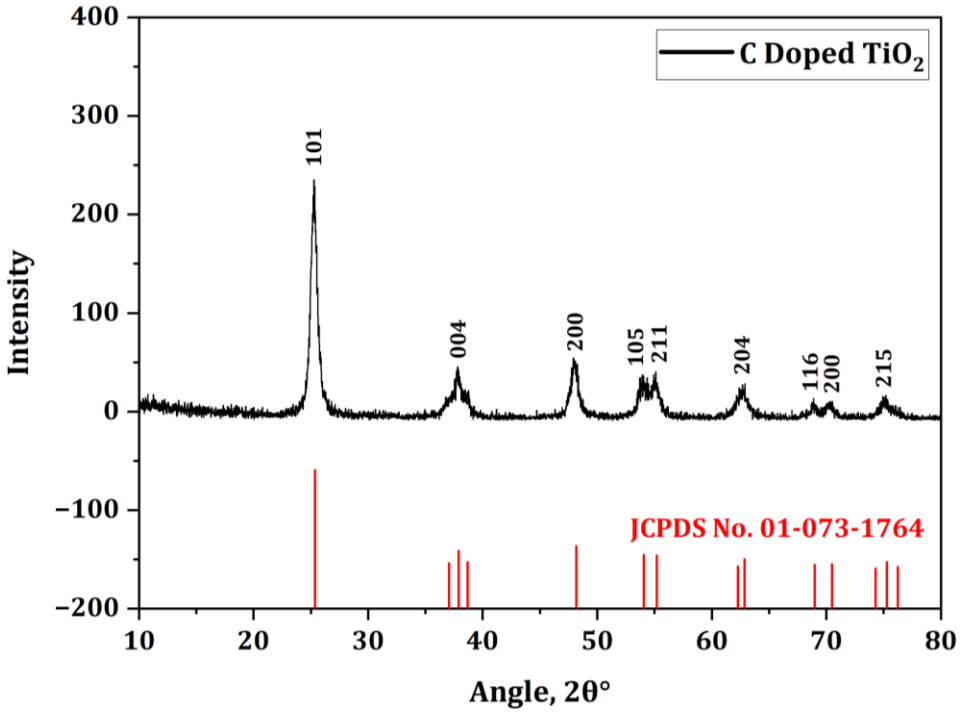

Figure 14: XRD Pattern of C-Doped TiO_2 Compared with Standard Reference

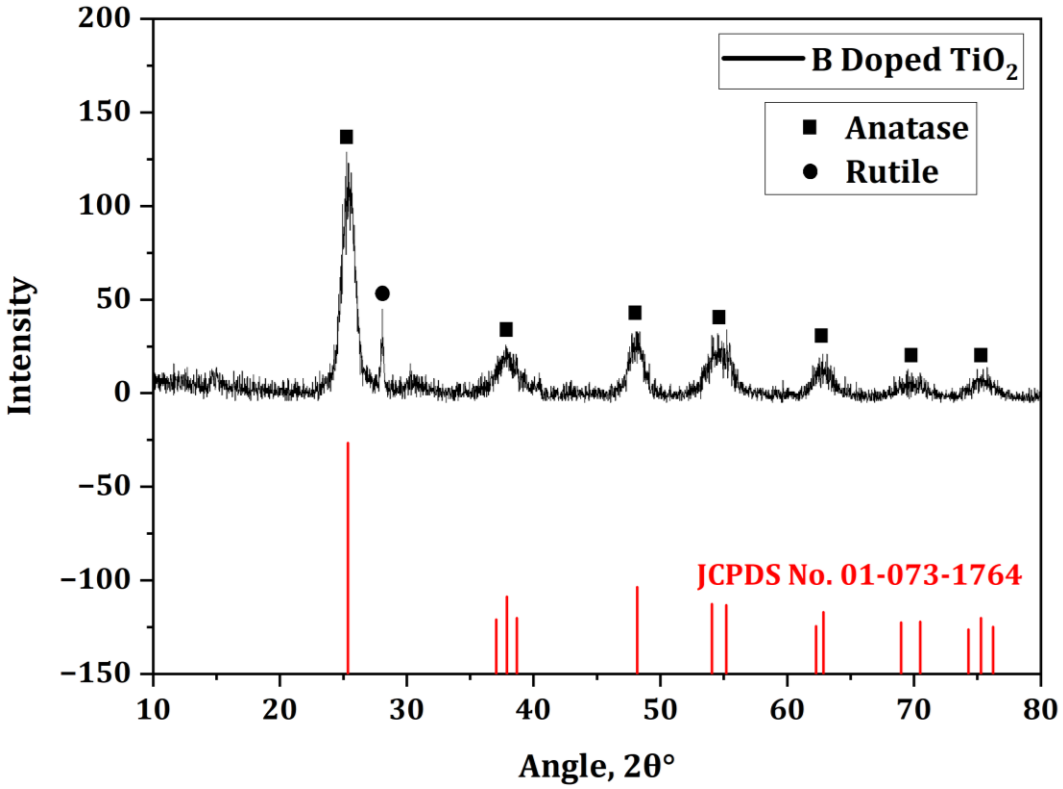

Figure 15: XRD Pattern of B-Doped TiO_2 Compared with Standard Reference

The peaks' positions and corresponding planes closely align with JCPDS card No. 01-073-1764 (TiO_2). In addition, the N-doped and C-doped samples display identical crystallographic planes with only slight positional variations. This validates that the synthesized undoped, N-doped, and C-doped TiO_2 samples feature a tetragonal crystal structure and anatase phase characterized by the I41/amd space group. So, it suggests that C and N are successfully doped without leading to the formation of any new phases. However, the B-doped TiO_2 sample shows an extra peak at 28.08º due to the rutile phase formation shown in Fig. 15.

The XRD pattern of the base and doped samples displays several sharp peaks, indicating they are polycrystalline powders. The most notable peak is associated with the crystal plane (101) at an angle of 25.367º. These sharp peaks indicate a high level of crystallinity in the material.

The degree of crystallinity from the XRD graph was also determined for five samples. The following equation is used to calculate the degree of crystallinity:

$$\text{Crystallinity} = \frac{\text{Area of crystalline peaks}}{\text{Area of all peaks (crystalline + amorphous)}} \times 100\%$$

Also, the crystallite size, strain, and dislocation density were calculated using Origin Software.

Table 1: Crystallite Size, Strain, and Dislocation Density of All Samples

Samples	Crystallinity, %	Crystallite Size, D nm	Micro Strain, ($\varepsilon \times 10^{-3}$)	Dislocation Density, δ ($\times 10^{-3}$ nm^2)
Commercial TiO_2	80.1275	32.96	2.48	0.921
Undoped TiO_2	75.3275	11.08	7.73	8.14
N-Doped TiO_2	60.9070	10.96	7.91	8.31
C-Doped TiO_2	60.1704	9.32	9.61	11.51
B-Doped TiO_2	58.0982	6.99	16.44	20.47

4.2 SEM

The surface morphology and particle size of undoped and doped TiO_2 nanomaterials were analyzed using Scanning Electron Microscopy (SEM), as shown in Figure 16. The SEM images reveal that all samples, including undoped TiO_2 and B-, C-, and N-doped TiO_2, display a generally spherical shape with noticeable particle agglomeration. The undoped TiO_2 (Figures a and b) features relatively uniform grains, suggesting a narrow size distribution, which aligns with the histogram data indicating an average particle size of about 98.14 nm.

Minor morphological changes were detected for doped samples due to the addition of non-metal dopants. B-doped TiO_2 (Figures c and d) shows larger, more aggregated particles with a broader size distribution and an average size of 156.04 nm, the largest of all the samples. This indicates that boron doping encourages grain growth or agglomeration during synthesis. Conversely, C-doped TiO_2 (Figures e and f) exhibits a more intricate structure with smaller, less agglomerated particles, resulting in a reduced average particle size of 86.93 nm. N-doped TiO_2 (Figures g and h) shows grains that are moderately larger and more aggregated than those in C-doped TiO_2, with an average size of 124.34 nm. The particle size histograms (Figure 17) reinforce these findings, following a lognormal distribution in all samples. The differences in particle size associated with various dopants can be linked to their effects on nucleation and growth kinetics during synthesis. The SEM analysis verifies the successful production of TiO_2 nanoparticles and highlights the morphological impact of non-metal doping.

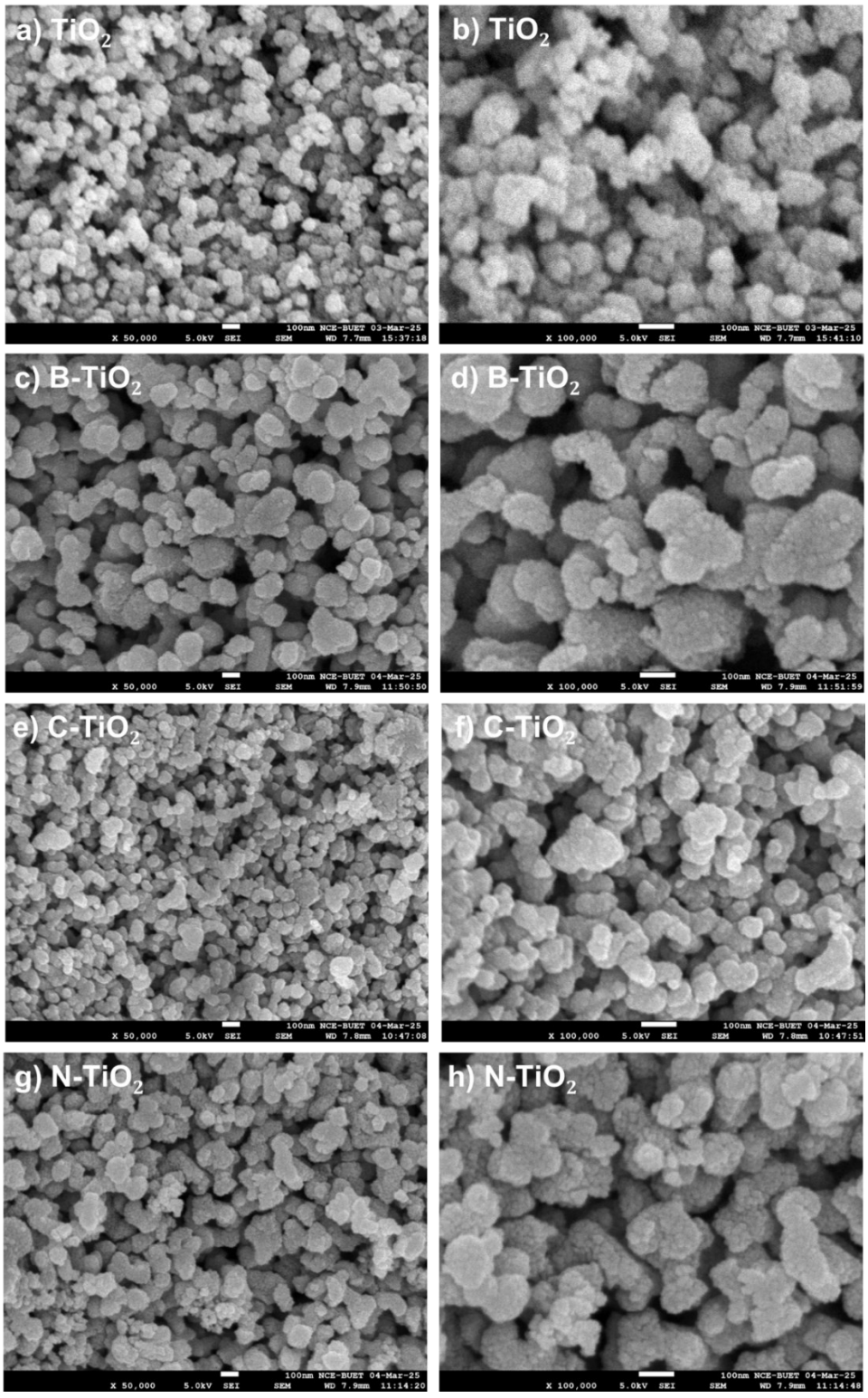

Figure 16: SEM images of TiO_2 at (a) 50,000x, (b) 100,000x; B-TiO_2 at (c) 50,000x, (d) 100,000x; C-TiO_2 at (e) 50,000x, (f) 100,000x; N-TiO_2 at (g) 50,000x, (h) 100,000x.

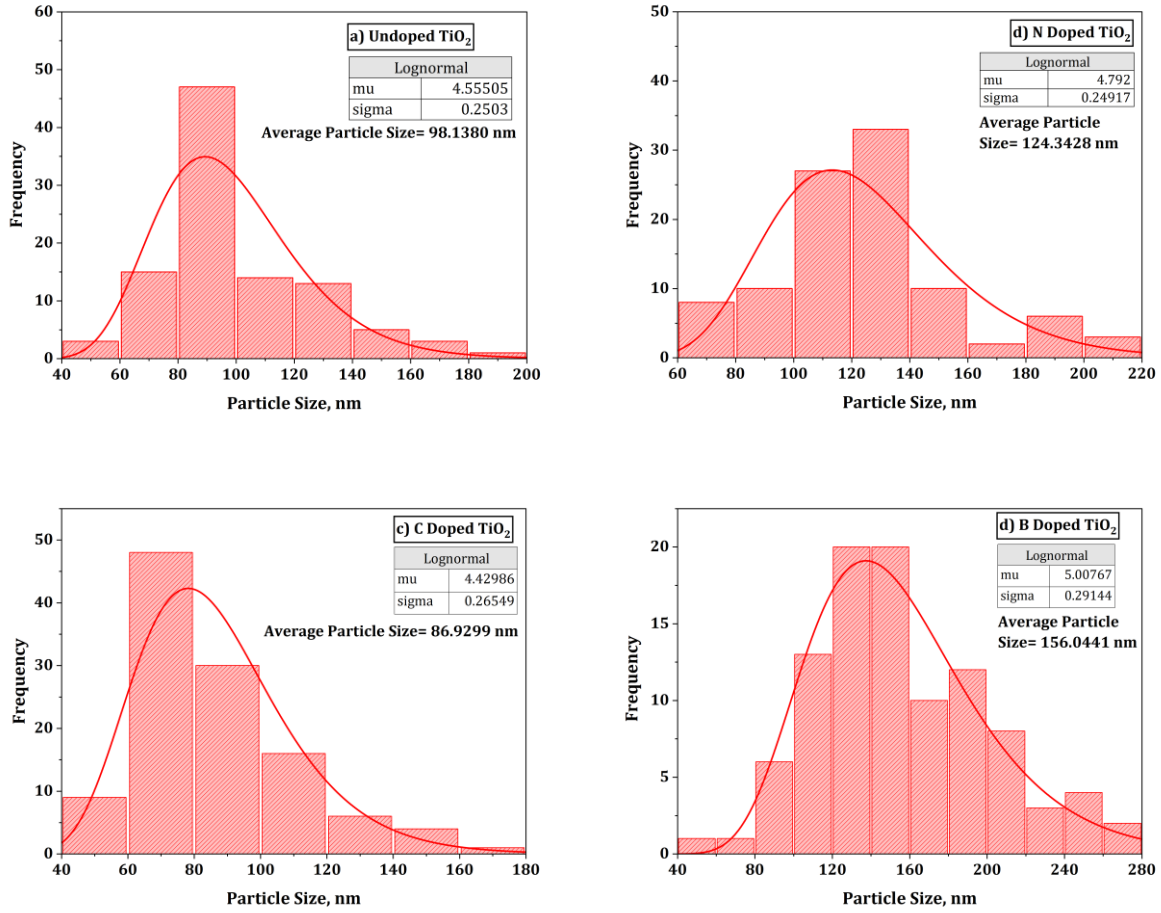

Figure 17: Size distribution histogram of (a) TiO_2, (b) N-TiO_2, (c) C-TiO_2, and (d) B-TiO_2

4.3 EDX

Energy Dispersive X-ray Spectroscopy (EDX) was employed to assess the elemental composition of both pristine and doped TiO_2 samples, specifically those doped with boron (B), carbon (C), and nitrogen (N). Figure 18 and Tables 2–5 display the spectra and the corresponding atomic/weight percentages. In the EDX spectrum for undoped TiO_2 (Figure 18a), peaks for titanium (Ti) and oxygen (O) are evident, confirming that the base TiO_2 material is pure. Table 2 indicates that the atomic percentage of titanium consistently ranges from 45.60% to 50.96%, while oxygen spans

from 49.04% to 54.40%, reflecting a nearly stoichiometric composition. For boron-doped TiO_2 (Figure 18b and Table 3), the EDX spectrum does not show any distinct boron peak. The elemental analysis table also lists blanks for both the atomic and weight percentages of boron across all points sampled, implying that boron is not detectable using EDX, likely due to its low atomic number and the detection limitations of the EDX system. Nonetheless, titanium and oxygen are recorded within the expected compositional range. The EDX spectrum for carbon-doped TiO_2 (Figure 18c) displays a significant C Kα peak near 0.28 keV.

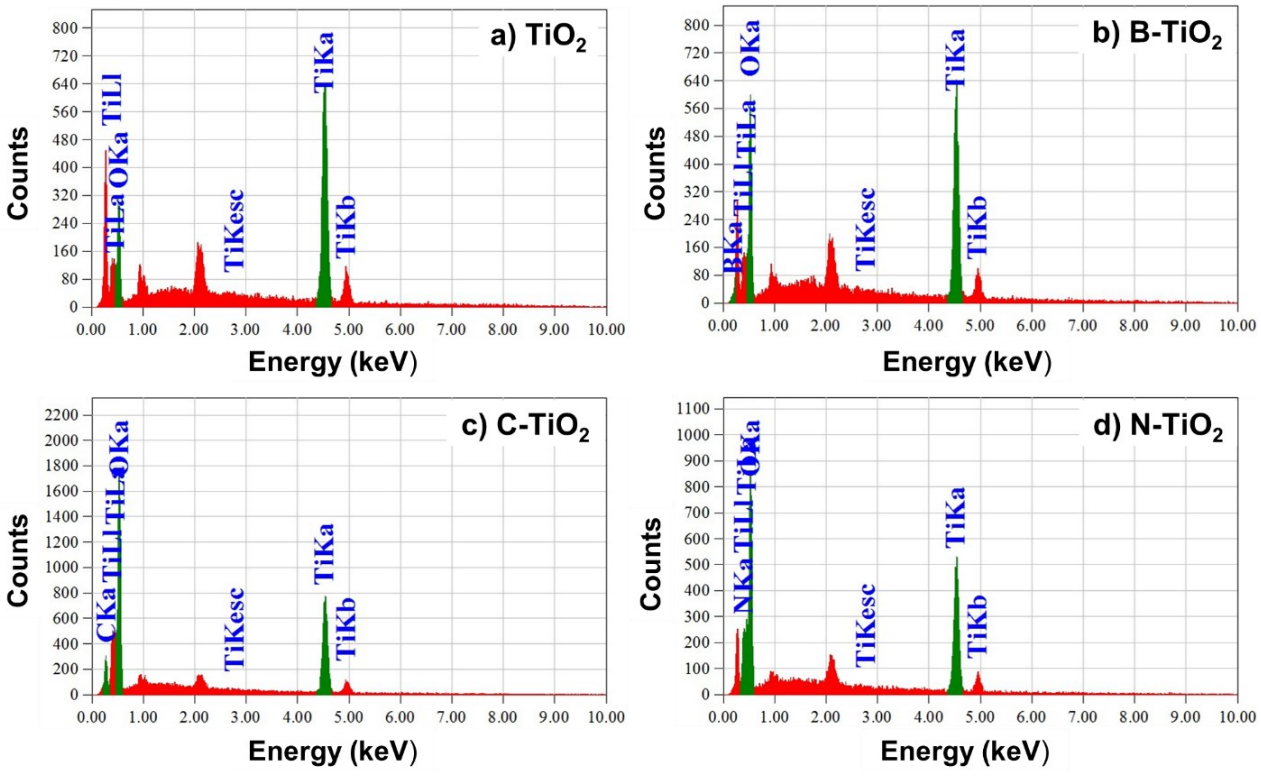

Figure 18: EDS Spectra of (a) TiO_2, (b) B-TiO_2, (c) C-TiO_2, and (d) N-TiO_2

This is corroborated by the quantitative data in Table 4, which indicates that the carbon content ranges from 10.02% to 12.62% (atomic%) and 5.51% to 7.12% (weight%), demonstrating successful carbon detection via EDX, likely owing to its greater detectability compared to boron

and nitrogen. The percentages of titanium and oxygen remain consistent with those found in a typical TiO_2 matrix. For nitrogen-doped TiO_2 (Figure 18d and Table 5), the EDX spectrum shows no nitrogen peaks, and the nitrogen content is recorded as undetectable in the table. This again illustrates that nitrogen, like boron, is challenging to detect using EDX due to its low atomic number, with its characteristic X-rays falling outside the effective detection range of the instrument utilized.

Table 2: EDX data of Undoped TiO_2

Elements	**Titanium**		**Oxygen**	
Spectrum	Atomic %	Weight %	Atomic %	Weight %
Point 1	45.60	71.51	54.40	28.49
Point 2	50.96	75.68	49.04	24.32
Point 3	49.29	74.43	50.71	25.57
Point 4	47.71	73.20	52.29	26.80
Point 5	47.63	73.14	52.37	26.86

Table 3: EDX data of 5% B-doped TiO_2

Elements	**Boron**		**Titanium**		**Oxygen**	
Spectrum	Atomic %	Weight %	Atomic %	Weight %	Atomic %	Weight %
Point 1	✕	✕	32.11	58.61	67.89	41.39
Point 2	✕	✕	33.93	60.59	66.07	39.41
Point 3	✕	✕	31.28	57.68	68.72	42.32
Point 4	✕	✕	39.43	66.09	60.57	33.91
Point 5	✕	✕	34.53	61.22	65.47	38.78

Table 4: EDX data of 5% C-doped TiO_2

Elements	Carbon		Titanium		Oxygen	
Spectrum	Atomic %	Weight %	Atomic %	Weight %	Atomic %	Weight %
Point 1	10.63	5.87	19.35	42.62	70.02	51.51
Point 2	12.08	6.75	18.72	41.73	69.20	51.51
Point 3	12.62	7.12	18.15	40.84	69.24	52.04
Point 4	10.02	5.51	19.56	42.90	70.42	51.59
Point 5	10.44	5.77	19.25	42.45	70.31	51.78

Table 5: EDX data of 5% N-doped TiO_2

Elements	Nitrogen		Titanium		Oxygen	
Spectrum	Atomic %	Weight %	Atomic %	Weight %	Atomic %	Weight %
Point 1	✕	✕	26.34	51.71	73.06	48.29
Point 2	✕	✕	24.01	48.61	75.99	51.39
Point 3	✕	✕	24.79	49.67	75.21	50.33
Point 4	✕	✕	25.48	50.59	74.52	49.41
Point 5	✕	✕	27.26	52.88	72.74	47.12

4.4 TEM

Figure 19 shows the morphology and particle distribution of:

[A] Undoped TiO_2: Particles are agglomerated, showing irregular shapes with sizes roughly around 20–30 nm. The particles appear as dense clusters.

[B] B–TiO_2: The B-doped TiO_2 particles also form aggregates but seem slightly larger and more interconnected than undoped TiO_2, suggesting that boron doping influenced particle growth and aggregation behavior.

[C] C–TiO_2: The C-doped TiO_2 shows smaller but more uniformly dispersed particles than other samples, with relatively less agglomeration, indicating that carbon doping restricted grain growth effectively during synthesis.

[D] N–TiO_2: Nitrogen-doped TiO_2 shows aggregated particles with moderately uniform sizes, similar to undoped TiO_2 but with more precise particle boundaries.

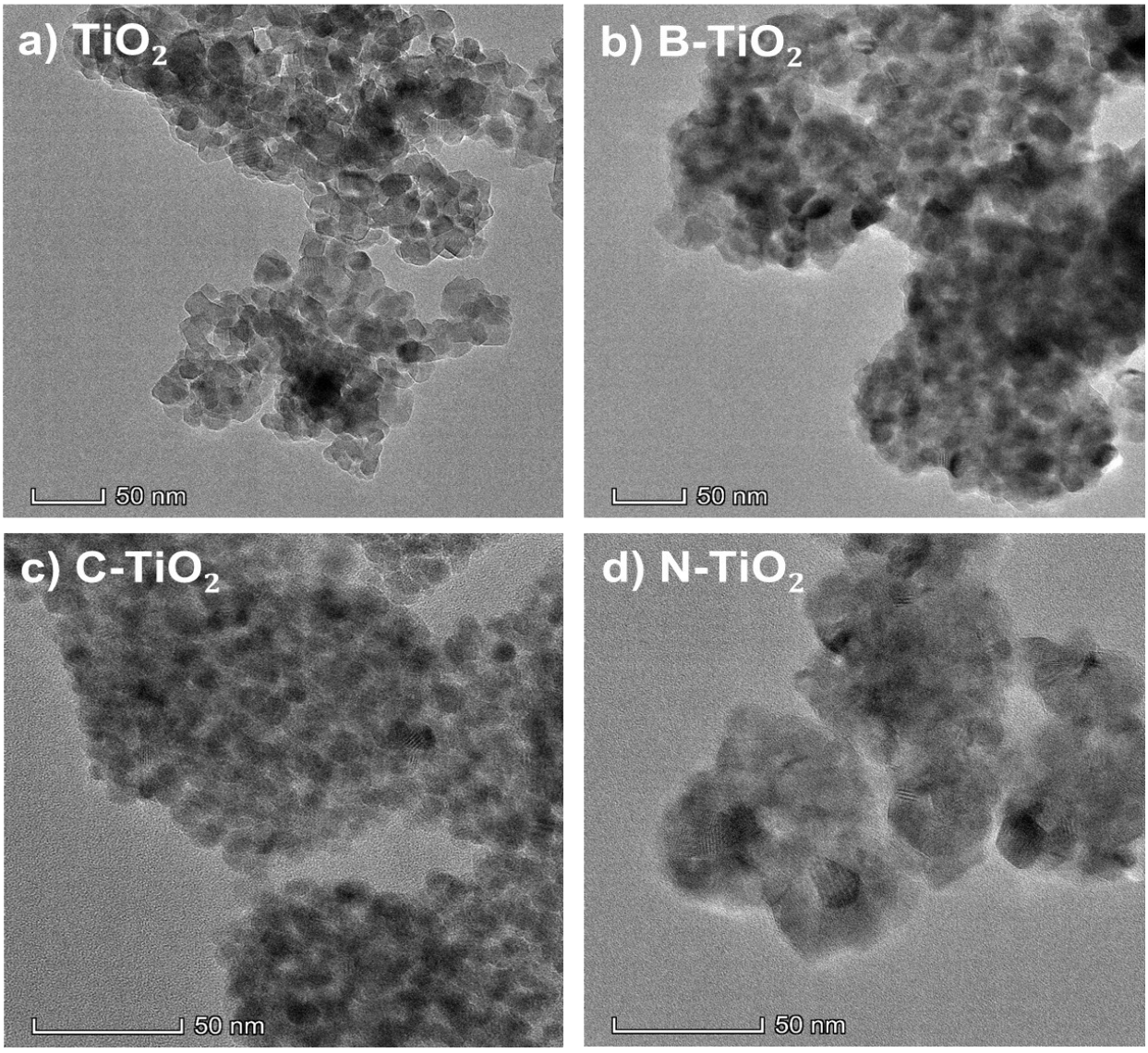

Figure 19: TEM pattern of (a) TiO_2, (b) B-TiO_2, (c) C-TiO_2, and (d) N-TiO_2 nanocomposites

Figure 20(a-d) illustrates the selected area electron diffraction (SAED) patterns for undoped TiO_2, N-doped TiO_2, C-doped TiO_2, and B-doped TiO_2, respectively. The multi-crystalline nature of the samples, as confirmed previously with XRD analysis, is shown by the concentric circles with bright spots at different positions. ImageJ software was used to measure the circles' diameters and subsequently determine the interplanar spacing (d-spacing) values of those rings. The measured interplanar distances for undoped-TiO_2, $d_1 = 0.3410$ nm, $d_2 = 0.2315$ nm, $d_3 = 0.1847$ nm, and d_4

= 0.1638 nm, d_5= 0.1448 nm, d_6= 0.1313 nm, d_7= 0.1250 correspond to the crystal planes (101), (112), (200), (211), (204), (220), and (301) respectively, using JCPDS card number. Similarly, for N-doped TiO_2, C-doped TiO_2, and B-doped TiO_2 crystal planes (101), (112), (200), (211), (204), (220), and (301) are observed.

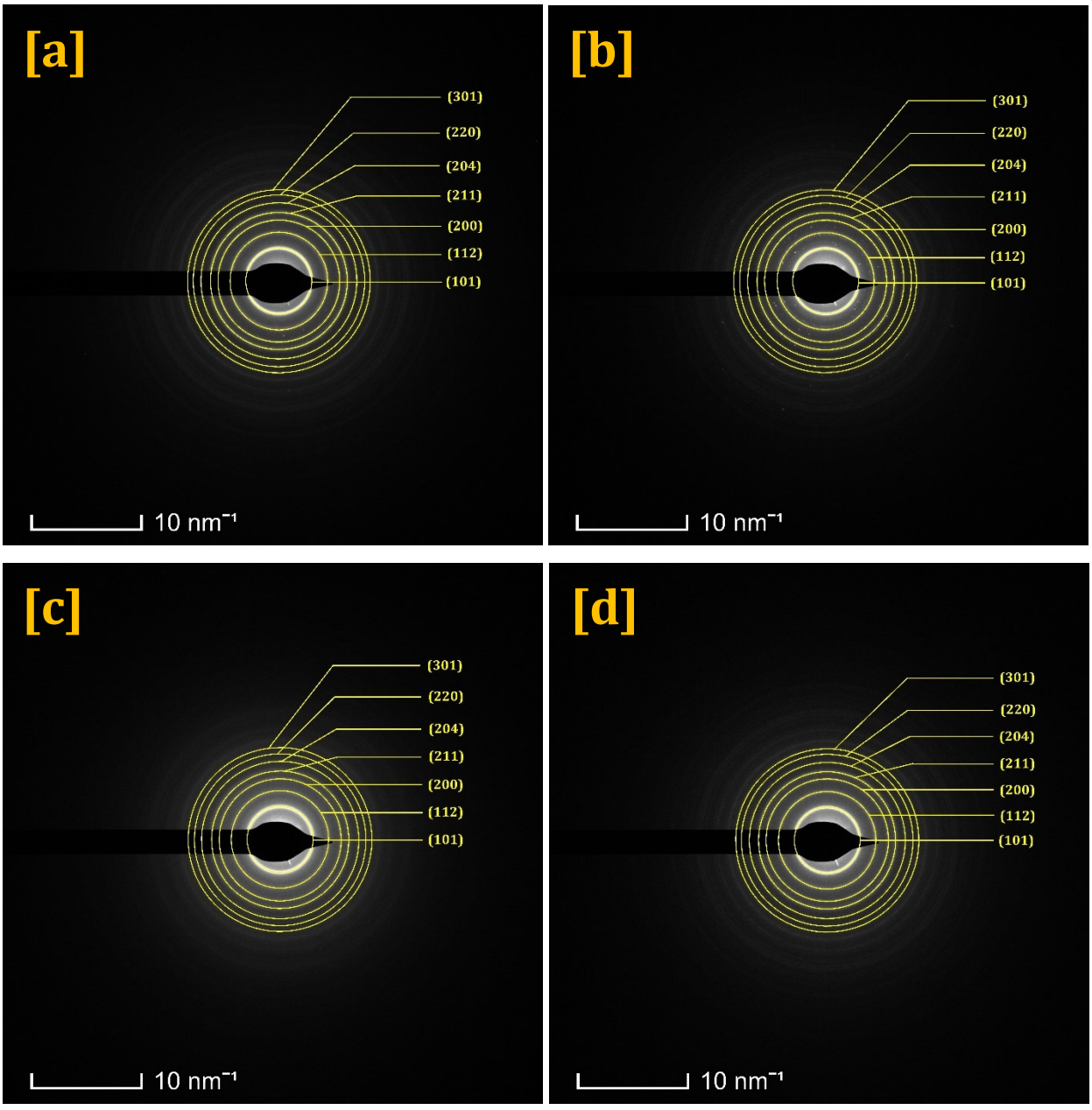

Figure 20: SAED patterns of undoped TiO_2, N-doped TiO_2, C-doped TiO_2, B-doped TiO_2 (a-d) respectively

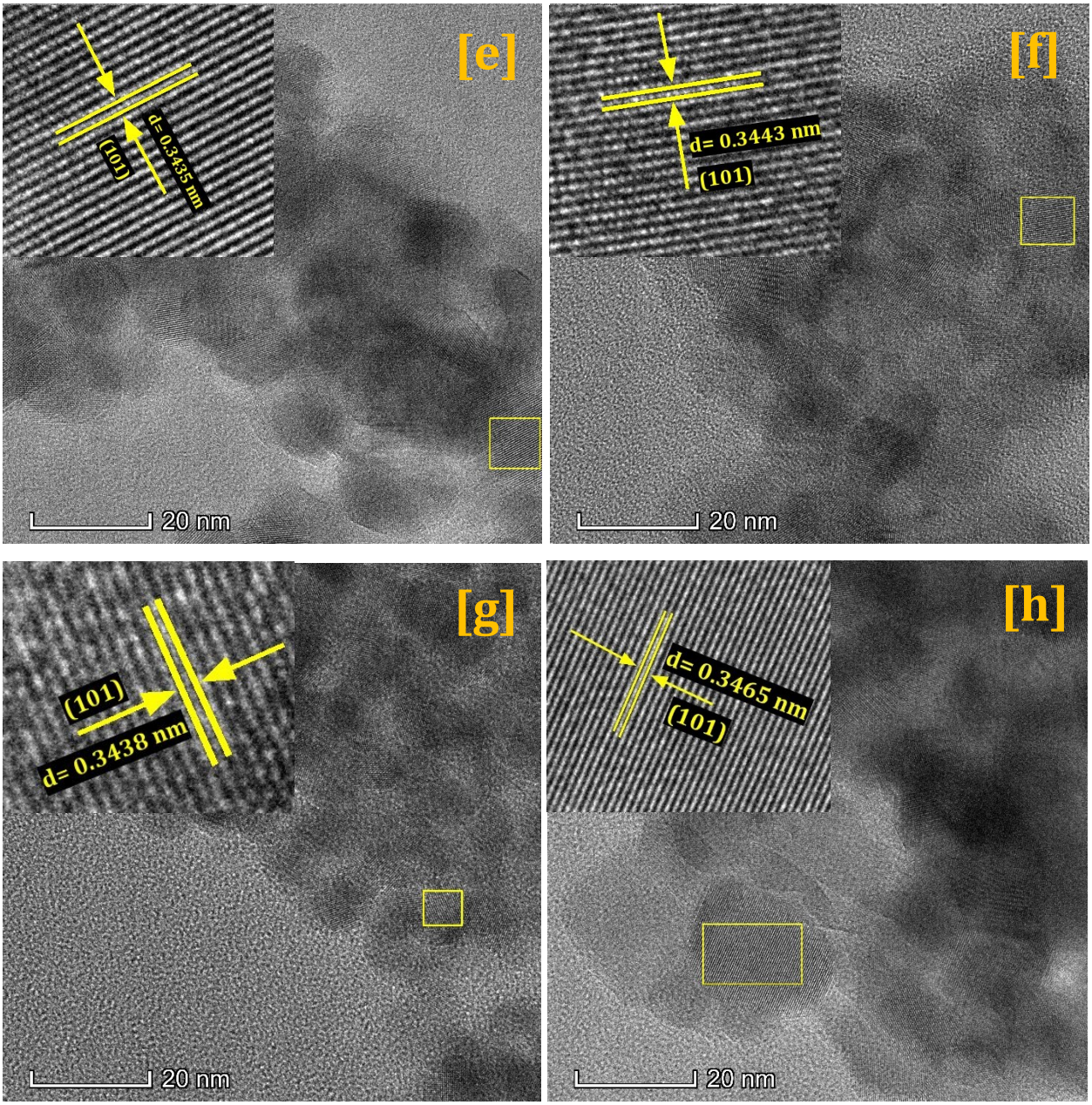

Figure 21: Lattice Fringes of undoped TiO_2, N-doped TiO_2, C-doped TiO_2, B-doped TiO_2 (e-h) respectively

The typical TEM images of undoped TiO_2, N-doped TiO_2, C-doped TiO_2, and B-doped TiO_2, along with visible lattice fringes, are shown in Figure 21(e-h). For the HR-TEM image analysis, the images were processed using the Fast Fourier Transform (FFT) technique via the Digital Micrograph tool. The interplanar spacing was determined from the FFT images, and several planes

were indexed with the aid of the JCPDS card No. 01-073-1764. These indexed planes are also compatible with the corresponding SAED patterns.

4.5 FTIR

The FTIR spectrum presented in the figure 22 offers a detailed comparison of the transmittance characteristics of several Titanium Dioxide (TiO_2) samples, including commercial TiO_2, undoped TiO_2, and TiO_2 doped with 5% nitrogen (N), boron (B), and carbon (C). The x-axis represents the wavenumber (cm^{-1}), and the y-axis indicates the transmittance percentage, which reveals information about the molecular vibrations and bond structures within the materials. Commercial TiO_2, represented by the black line, shows typical peaks corresponding to Ti-O stretching and bending vibrations, which are characteristic of the standard TiO_2 lattice structure. This spectrum serves as a reference for the other samples. In contrast, the undoped TiO_2 (represented by the red line) shows distinct spectral shifts, indicating that the nanoscale material undergoes different structural interactions compared to the bulk form. The increased surface area and smaller particle size of undoped TiO_2 contribute to these shifts, which may influence the material's surface chemistry, reactivity, and interaction with light. Further, the doping of TiO_2 with various elements such as nitrogen, boron, and carbon introduces noticeable alterations in the FTIR spectra, signaling changes in the material's bonding structure and electronic properties. For instance, the 5% N-doped TiO_2 (blue line) exhibits a shift in the vibrational modes, likely due to the incorporation of nitrogen into the TiO_2 lattice. This nitrogen doping can introduce new electronic states, affecting the bandgap and enhancing the material's photocatalytic activity under visible light. Similarly, 5% B-doped TiO_2 (orange line) shows distinct shifts that may be attributed to the formation of Ti-B

bonds, which alter the TiO_2 network and improve the photocatalytic performance by reducing recombination rates of photogenerated electron-hole pairs. The C-doped TiO_2 (magenta line) also exhibits spectral changes, likely due to the creation of Ti-C bonds, which modify the material's electronic structure and can improve photocatalytic efficiency, particularly for visible light-driven reactions. These variations in the FTIR spectra indicate that doping TiO_2 with nitrogen, boron, or carbon significantly impacts the material's atomic and molecular structure, which in turn influences its photocatalytic properties. The observed shifts in the spectral peaks suggest that the doping process modifies the electronic environment around TiO_2, creating new active sites and altering the bandgap. Additionally, the FTIR analysis provides essential insights into the role of different dopants in fine-tuning TiO_2's properties for these applications, highlighting the importance of tailoring the material's composition to optimize its performance in various environmental processes.

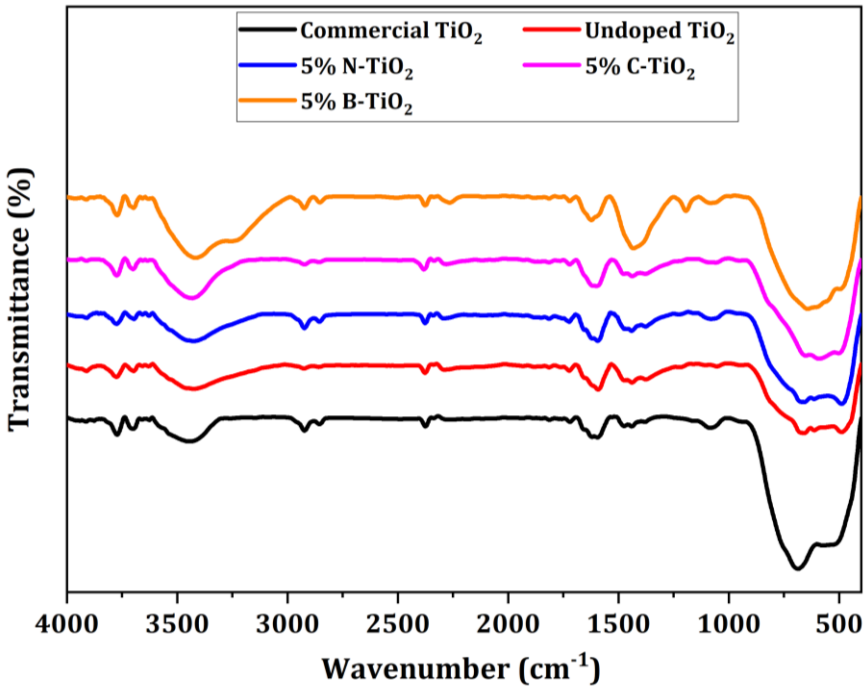

Figure 22: FTIR curve of commercial TiO_2, undoped TiO_2, 5% B-doped TiO_2, 5% C-doped TiO_2, and 5% N-doped TiO_2

4.6 DLS PARTICLE SIZE DISTRIBUTION AND ZETA POTENTIAL

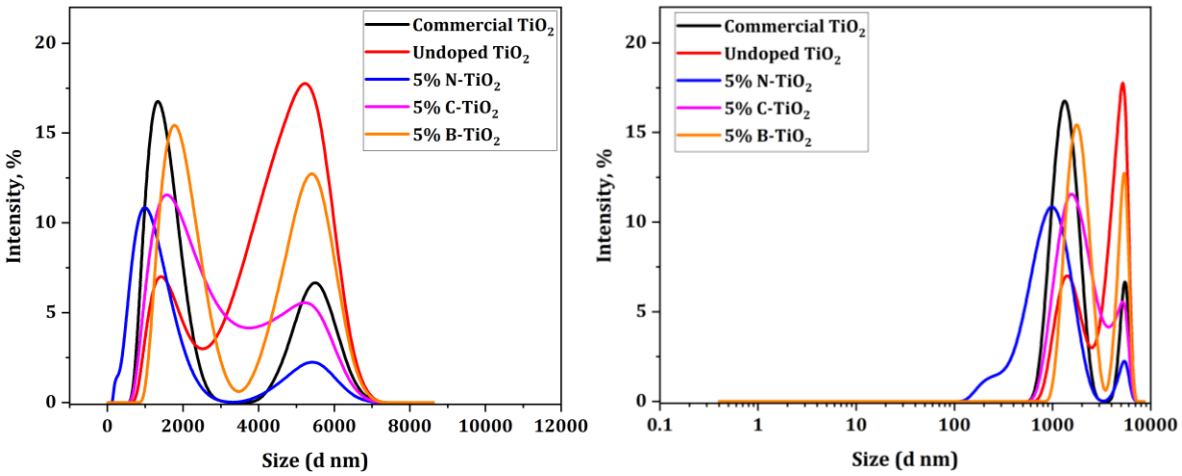

Figure 23: DLS Particle Size Distribution of Commercial, Undoped TiO_2, and Doped TiO_2 Samples in normal scale (left) and log scale (right)

Dynamic Light Scattering (DLS) measurements yield important information on the hydrodynamic particle size distribution of commercial, undoped, and non-metal-doped (B, C, and N) TiO_2 samples. Figure 23 shows that the size of commercial TiO_2 is above all the range of published data, with considerable peaks around 2000-4000 nm, showing the presence of bigger agglomerated particles. On the other hand, undoped-TiO_2 has a significant size reduction and higher homogeneity, marked by a shift of the peak below ~1000 nm, and hence uniform dispersion and nano-sized particles forming a nanostructured material. Doping also reshapes the distribution of the particle size; in particular, N-doped TiO_2 (5% N-TiO_2) has the smallest average size of all (as can be seen both by the narrow peak and the shift of the peak to lower sizes) and the narrowest distribution, followed by C-, and B-doped TiO_2 samples. Lower particle size, such as that of undoped- and doped TiO_2, generally means a higher surface area, which is advantageous in adsorption processes as it offers an increase in the number of active sites onto which metal ions can interact.

[a] Commercial TiO_2

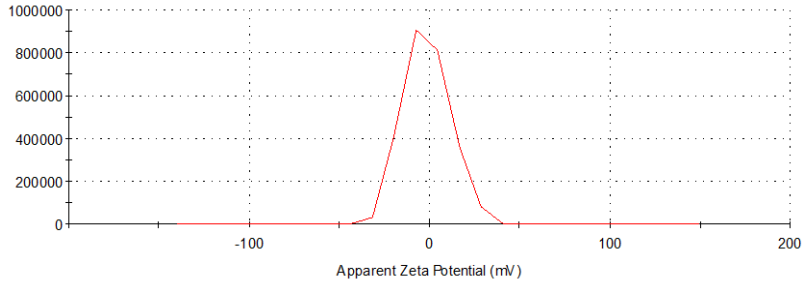

[b] Undoped TiO_2

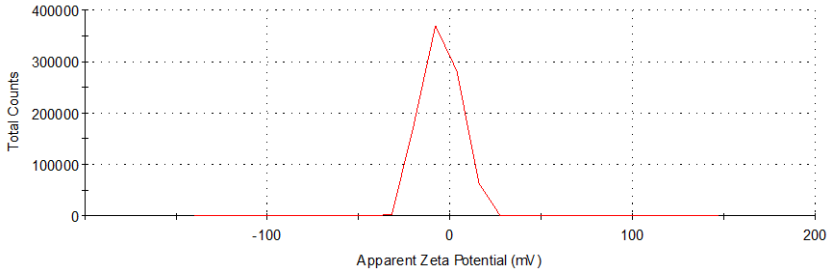

[c] 5% N-TiO_2

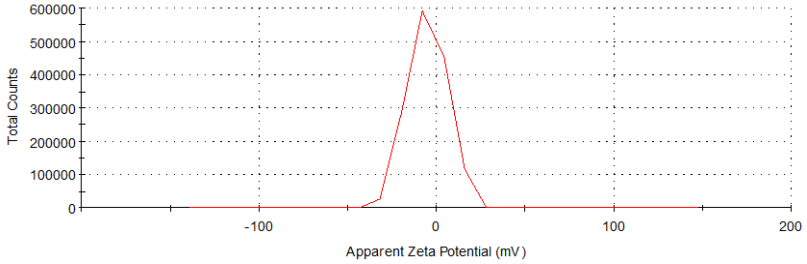

[d] 5% C-TiO_2

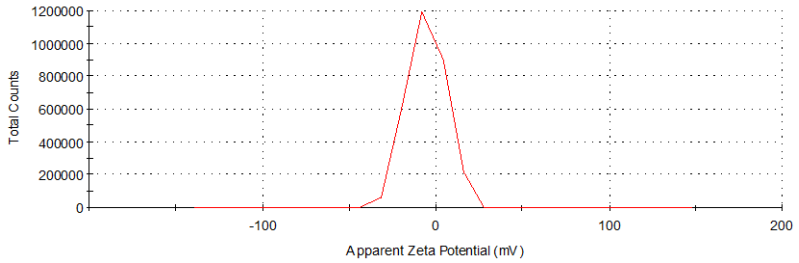

[e] 5% B-TiO_2

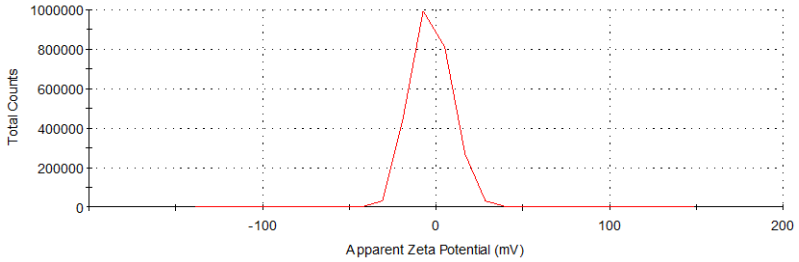

Figure 24: Zeta Potential Curve of [a] Commercial TiO_2, [b] Undoped TiO_2, [c] 5% N-doped TiO_2, [d] 5% C-doped TiO_2, [e] 5% B-doped TiO_2

Table 6: Zeta Potential and Conductivity of All Samples

Sample	Conductivity (mS/cm)	Zeta Potential (mV)
Commercial TiO_2	0.027	-1.33
Undoped TiO_2	0.0175	-5.14
5% N-Doped TiO_2	0.0152	-4.86
5% C-Doped TiO_2	0.015	-5.34
5% B-Doped TiO_2	0.00851	-2.71

Commercial TiO_2

The Zeta potential of commercial TiO_2 is measured at -1.33 mV, which indicates a relatively low surface charge. This suggests that the commercial TiO_2 suspension is less stable compared to the others, with more negative values, but it can remain stable under certain conditions. The conductivity is 0.027 mS/cm, which is the highest among all the samples, suggesting that commercial TiO_2 has relatively good electrical conductivity, possibly due to its larger particle size and easier flow of ions.

Undoped TiO_2

Undoped TiO_2 exhibits a more negative Zeta potential of -5.14 mV, indicating significantly better colloidal stability compared to the bulk form. The smaller particle size and greater surface area have an enhanced stabilizing effect due to increased repulsive forces between particles. Furthermore, undoped TiO_2 has a conductivity of 0.0175 mS/cm, which is lower than that of

commercial TiO_2. This loss of conductivity is likely due to smaller particles hindering ion movement and surface conductivity.

5% N-doped TiO_2

For 5% N-doped TiO_2, the Zeta potential measured is -4.86 mV, showing moderately negative value resulting in reasonable stability in suspension. As previously discussed, the doped nitrogen does increase some defect states or charge carriers on the surface, which affects the overall particle charge balance and stability of the system. Conductivity also decreases slightly to 0.0152 mS/cm, which is even lower than that of undoped TiO_2. This comes as no surprise since doping always impacts materials by changing their electronic structure, leading to altered electrical properties.

5% C-doped TiO_2

The Zeta potential of 5% C-doped TiO_2 is -5.34 mV, more negative than that of N-doped. The higher negative value indicates that carbon doping stabilizes the TiO_2 particles by increasing the surface charge, which may also increase the repulsive force between the particles. The conductivity of C-doped TiO_2 is 0.015 mS/cm, which is comparable to that of N-doped TiO_2. This suggests that carbon doping has a similar effect on the electrical conductivity because the doping of carbon atoms changes the charge transport properties.

5% B-doped TiO_2

The lowest value of the Zeta potential, indicating a negative charge (-2.71 mV), is observed for the 5% B-TiO_2 doped sample, which corresponds to lower stability in suspension compared to the other doped samples. Boron doping may result in a smaller alteration in the surface charge of TiO_2 than nitrogen or carbon doping; thus, it can generate a less stable suspension. The electrical

conductivity of B-doped TiO_2 is 0.00851 mS/cm, which is the minimum for all the samples. This suggests that B doping could decrease its electrical conductivity, which could probably be attributed to a modified electronic structure with reduced electrons available for conduction.

4.7 UV-VIS

The adsorption behavior of iodine on various TiO_2-based samples—including commercial TiO_2, undoped TiO_2, and non-metal doped TiO_2 (N, C, B doped)—was investigated using UV-Visible (UV-Vis) absorption spectroscopy. The aim was to evaluate the iodine adsorption efficiency of the synthesized photocatalysts. The efficiency for this adsorption was calculated using this equation:

$$\text{Efficiency} = \frac{C_0 - C_t}{C_0} \times 100\%$$

Where C_0 = Initial Concentration

C_t = Concentration after certain time

Table 7: Iodine ion adsorption efficiency for all samples

Sample	Time	I Removal Efficiency (%)
Commercial-TiO_2	10	3.597
	20	6.521
	30	14.311
	40	21.086
	50	27.282
	60	32.972
Undoped-TiO_2	10	4.645
	20	9.78
	30	17.692
	40	25.714
	50	32.637
	60	35.604
B-TiO_2	10	5.658
	20	10.255
	30	18.326
	40	27.138
	50	34.505
	60	37.208
C-TiO_2	10	6.426
	20	12.541
	30	19.372
	40	27.398
	50	35.908
	60	38.745
N-TiO_2	10	8.976
	20	17.843
	30	26.477
	40	33.883
	50	40.867
	60	45.28

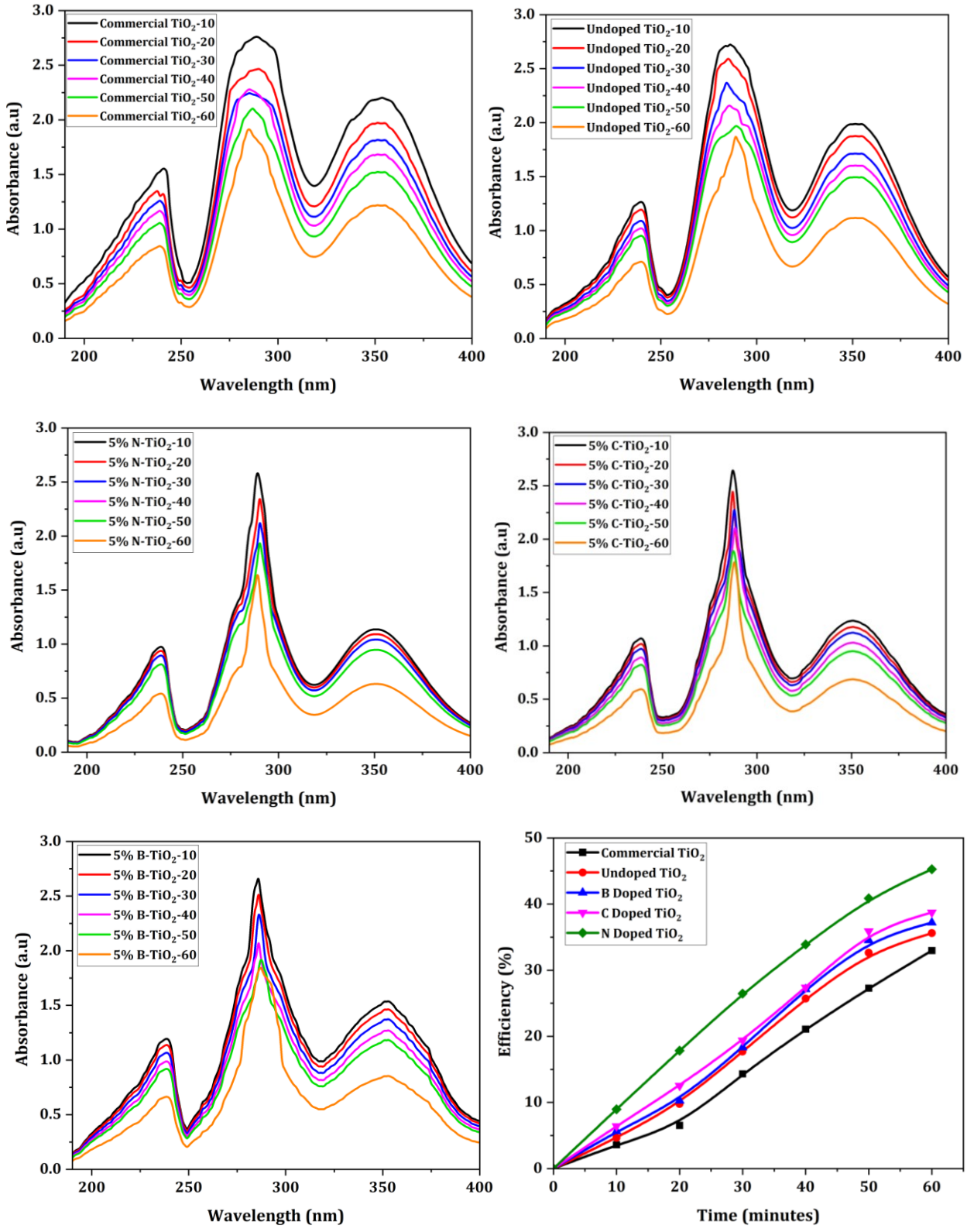

Figure 25: UV-Vis of all samples for iodine for 60 minutes and iodine adsorption curve for all samples

Although direct adsorption spectroscopy is a typical method for evaluating iodine adsorption, this technique requires specific light sources or configurations—most notably, an iodine-specific lamp or appropriate calibration setup that can accurately monitor iodine species in solution. Due to the unavailability of such components, particularly the iodine lamp, adsorption spectroscopy could not be conducted in the present lab setting.

Therefore, UV-Vis spectroscopy was adopted as an alternative method to monitor the reduction in absorbance intensity corresponding to iodine's characteristic peaks (typically in the UV region). The UV-Vis absorbance spectra were recorded before and after the adsorption process. A notable decrease in intensity over time signifies the adsorption of iodine onto the surface of TiO_2-based samples.

All spectra show strong absorbance in the 200–400 nm range, with intensity decreasing as adsorption time increases or doping increases. Doped TiO_2 samples, particularly N-doped TiO_2, demonstrated the most significant reduction in absorbance intensity, suggesting superior iodine adsorption performance. The efficiency plot (Figure 25, right panel) clearly shows N-TiO_2 achieving the highest iodine removal efficiency over time compared to other samples.

4.8 ION ADSORPTION EFFICIENCY OF DOPED AND UNDOPED TiO_2

Figure 26 illustrates the time-dependent adsorption efficiency of various TiO_2 materials, including commercial, undoped, and non-metal doped (B, C, and N), for four different metal ions: Co^{2+}, I^-, Mn^{2+}, and Zn^{2+}. Although the primary objective of this research is to remove radionuclides from wastewater, actual radioactive isotopes were not utilized in this study due to safety, availability,

and facility limitations. Instead, non-radioactive analogues of these radionuclides—cobalt, iodine, manganese, and zinc—were chosen, as they closely mimic the chemical behavior and adsorption characteristics of their radioactive counterparts (e.g., $^{131}I^{-}$, $^{60}Co^{2+}$, $^{54}Mn^{2+}$, $^{65}Zn^{2+}$). This surrogate approach is widely accepted and scientifically valid for assessing the adsorption potential of materials intended for radionuclide remediation. The efficiency for this adsorption was calculated using this equation:

$$\text{Efficiency} = \frac{C_0 - C_t}{C_0} \times 100\%$$

Where C_0= Initial Concentration

C_t= Concentration after certain time

Table 8: Zn, Mn, and Co ion adsorption efficiency for all samples

Sample	Time	Zn Removal Efficiency (%)	Mn Removal Efficiency (%)	Co Removal Efficiency (%)
Commercial-TiO_2	10	8.921	4.436	2.296
	20	14.73	9.498	3.74
	30	19.915	13.1	4.895
	40	23.029	15.292	5.863
	50	24.066	16.336	6.784
	60	24.688	16.805	6.889
Undoped-TiO_2	10	9.983	4.482	2.734
	20	16.306	10.049	4.33
	30	20.965	13.399	5.382
	40	24.292	15.517	6.267
	50	25.623	16.896	6.961
	60	26.123	17.305	7.061
B-TiO_2	10	9.96	8.039	10.376
	20	16.015	14.041	12.677
	30	21.484	17.015	13.68
	40	24.804	19.768	14.506
	50	26.953	22.246	15.281
	60	27.929	22.797	15.591
C-TiO_2	10	13.022	4.427	3.621
	20	24.115	8.258	5.583
	30	30.225	10.646	7.132
	40	33.922	12.984	8.359
	50	34.565	13.084	9.253
	60	35.048	13.184	9.61
N-TiO_2	10	3.883	4.612	1.151
	20	6.601	7.197	1.901
	30	8.737	9.021	2.452
	40	10.485	11.099	2.972
	50	11.262	12.113	3.403
	60	11.65	12.671	3.489

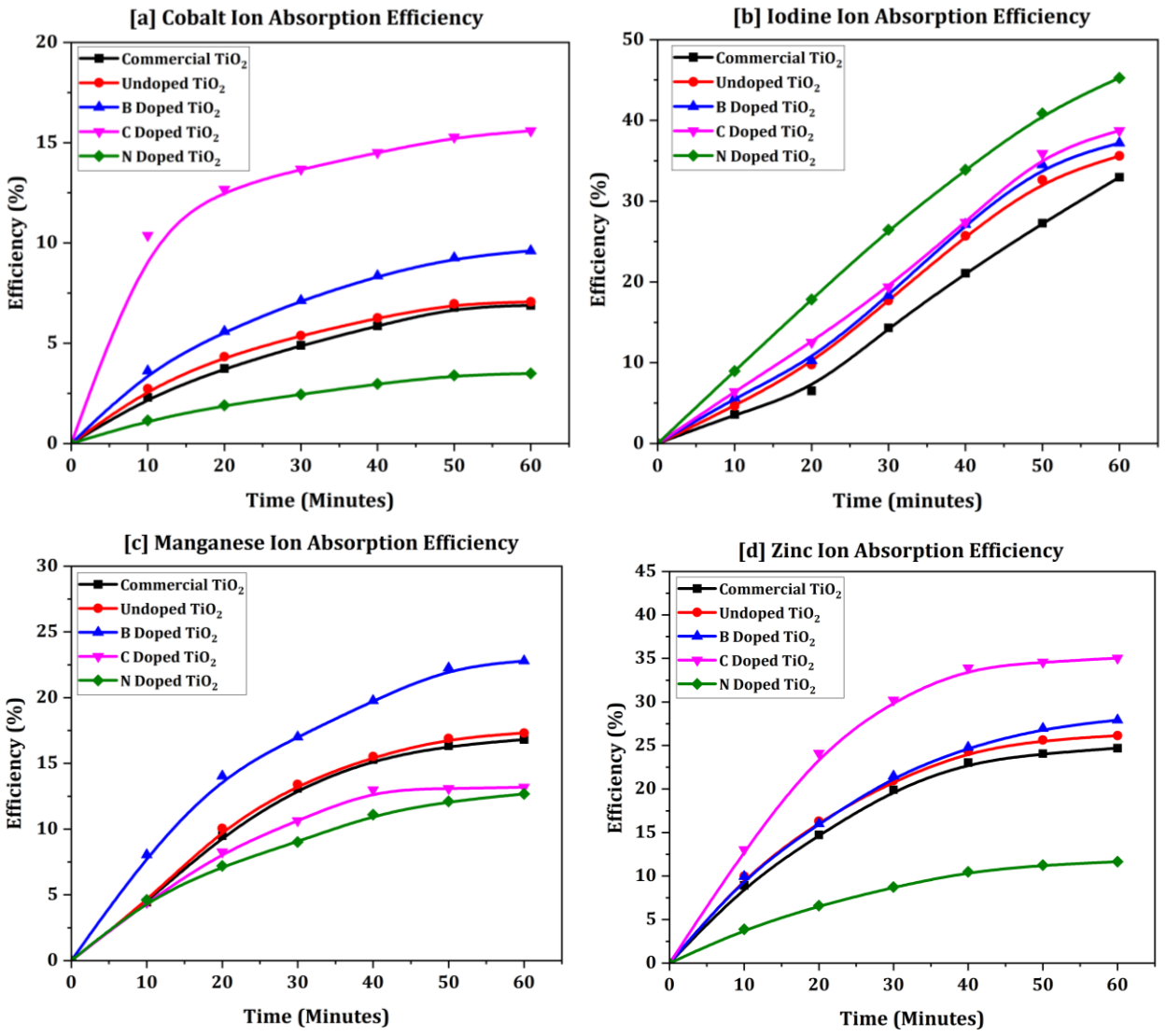

Figure 26: Time-dependent Metal Ion Adsorption Efficiency of Doped and Undoped TiO_2 for (a) Co^{2+}, (b) I^-, (c) Mn^{2+}, and (d) Zn^{2+} Ions

The cobalt ion adsorption efficiency reveals that C-doped TiO_2 exhibits the highest performance, reaching close to 16% efficiency at 60 minutes. In contrast, N-doped TiO_2 shows the lowest efficiency, plateauing around 4%. Both undoped and B-doped TiO_2 samples show moderate adsorption capacities. This trend suggests that carbon doping significantly enhances surface reactivity toward Co^{2+} ions, potentially due to increased surface area or modified charge distribution. In the case of iodine ions, N-doped TiO_2 demonstrates the highest adsorption efficiency, surpassing 40% at 60 minutes. C-doped and B-doped samples follow this. Commercial

TiO_2 exhibits the least efficiency. The enhanced performance of N-doped TiO_2 here may result from improved surface chemistry or increased affinity for iodine ions. Figure 26c shows that B-doped TiO_2 achieves the highest manganese ion adsorption (~23%) after 60 minutes. Undoped and commercial TiO_2 follow closely behind, while C- and N-doped TiO_2 display lower efficiencies. These results suggest that boron doping may introduce favorable sites or pore structures, enhancing Mn^{2+} capture. C-doped TiO_2 again exhibits superior efficiency for zinc ion adsorption, reaching nearly 40%. N-doped TiO_2 shows the weakest performance in this case, while the remaining samples demonstrate intermediate adsorption rates. This trend emphasizes the effectiveness of carbon doping in promoting Zn^{2+} adsorption, likely due to its electronic or structural modifications to the TiO_2 matrix.

Table 9: Summary of Ion Adsorption Efficiency Trends

Ion Type	Best Performing Sample	Worst Performing Sample
Co^{2+}	C-doped TiO_2	N-doped TiO_2
I^-	N-doped TiO_2	Commercial TiO_2
Mn^{2+}	B-doped TiO_2	N-doped TiO_2
Zn^{2+}	C-doped TiO_2	N-doped TiO_2

For Co^{2+} adsorption, B-doped TiO_2 exhibits the highest efficiency, followed by undoped-TiO_2, which aligns with their relatively smaller particle sizes. Interestingly, N-doped TiO_2, despite having the smallest size, shows the lowest CO^{2+} adsorption. This anomaly may be attributed to

changes in surface chemistry or electronic structure due to N-doping, which may not favor Co^{2+} binding.

In the case of I^- adsorption, N-doped TiO_2 exhibits the highest efficiency, consistent with its finest particle size and, consequently, the maximum surface availability. All doped and undoped-TiO_2 samples outperform commercial TiO_2, highlighting the direct influence of reduced particle size and increased surface reactivity.

For Mn^{2+} and Zn^{2+} ions, similar trends are observed, where undoped- and B-doped TiO_2 demonstrate superior adsorption compared to commercial samples. Zn^{2+} adsorption, in particular, is highest for B-doped TiO_2, indicating that both particle size and the specific dopant chemistry contribute synergistically to adsorption behavior.

In summary, DLS analysis confirms that reducing particle size through nanostructuring or doping significantly enhances the adsorption efficiency of TiO_2 for most tested metal ions. However, the relationship is not always linear or straightforward—dopant-specific effects and interactions with individual ions play a critical role. Thus, while smaller size generally improves performance, optimal adsorption depends on a balance of particle size, surface chemistry, and the nature of the dopant.

4.8.1 ZETA POTENTIAL AND ADSORPTION EFFICIENCY CORRELATION:

Commercial TiO_2

Substances Co^{2+}, I^-, and Mn^{2+}, as well as Zn^{2+} ions, demonstrate the least adsorption efficiency when it comes to commercial TiO_2. Furthermore, its low zeta potential signifies reduced surface

charge and decreased stability while suspended. This negatively impacts its interaction with the metal ions that determine the adsorption capacity. Although there is a high conductivity, suggesting some movement of ions, instability in suspension will always be an added disadvantage.

Undoped TiO_2

Compared to commercial TiO_2, undoped-TiO_2 displays better adsorption efficiency, especially for Co^{2+} and I^- ions. Moreover, -5.14 mV negative Zeta potential improves colloidal stability, which can enhance the availability of the bond with metal ions. Also, finer particle size contributes to an increase in adsorption due to a larger surface area.

5% N-Doped TiO_2

For N-doped TiO_2, the order of preference for ion capture (adsorption) was I^- followed by Co^{2+}. The very negative zeta potential suggests considerable instability and enhanced inter-ionic interaction of N-TiO_2, thus augmenting stability overall. Additionally, it is known that doping with Nitrogen may improve surface chemistry, along with its charge distribution, substantially enhancing good adsorption.

5% C-Doped TiO_2

The performance of C-TiO_2 is better in the adsorption of Co^{2+} and Zn^{2+} ions, explained by the highly negative Zeta potential (-5.34 mV), which favors colloidal stability and improves surface reactivity. Carbon doping probably changes the electronic structure, increasing the material's capability of interacting with metal ions.

5% B-Doped TiO_2

B-doped TiO_2 displays the maximum adsorption capability to Mn^{2+}, whereas for Co^{2+}, I^-, and Zn^{2+}, the adsorption efficiency is lower. -2.71 mV in Zeta potential is the least negative compared to the other doped samples, indicating less stability and less ideal ion interaction. Nevertheless, boron doping can develop special active sites or porous structures with improved adsorption for manganese.

4.9 KINETIC MODELING OF RADIONUCLIDE REMOVAL BY DOPED TiO_2 NANOPARTICLES

To analyze the removal efficiency of radionuclide analogs by N-, C-, and B-doped TiO_2 nanoparticles, kinetic models offer critical insight into adsorption dynamics, surface interactions, and rate-controlling mechanisms. The time-dependent uptake of Co^{2+}, I^-, Mn^{2+}, and Zn^{2+} ions over 60 minutes, presented in the UV-Vis and AAS results, allows us to apply pseudo-first-order and pseudo-second-order kinetic models to evaluate adsorption mechanisms for each doped variant.

Pseudo-First-Order Kinetics

The pseudo-first-order equation is expressed as:

$$\frac{dq_t}{dt} = k_1(q_e - q_t)$$

Which integrates to:

$$ln(q_e - q_t) = lnq_e - k_1 t$$

- q_e: adsorption capacity at equilibrium (mg/g)
- q_t: adsorption capacity at time t
- k_1: first-order rate constant (min^{-1})
- t: time

Pseudo-Second-Order Kinetics

The pseudo-second-order model assumes chemisorption as the rate-limiting step and is defined by:

$$\frac{dq_t}{dt} = k_2(q_e - q_t)^2$$

Which integrates to:

$$\frac{t}{q_t} = \frac{1}{k_2 q_e^2} + \frac{t}{q_e}$$

- k_2: second-order rate constant ($g \cdot mg^{-1} \cdot min^{-1}$)

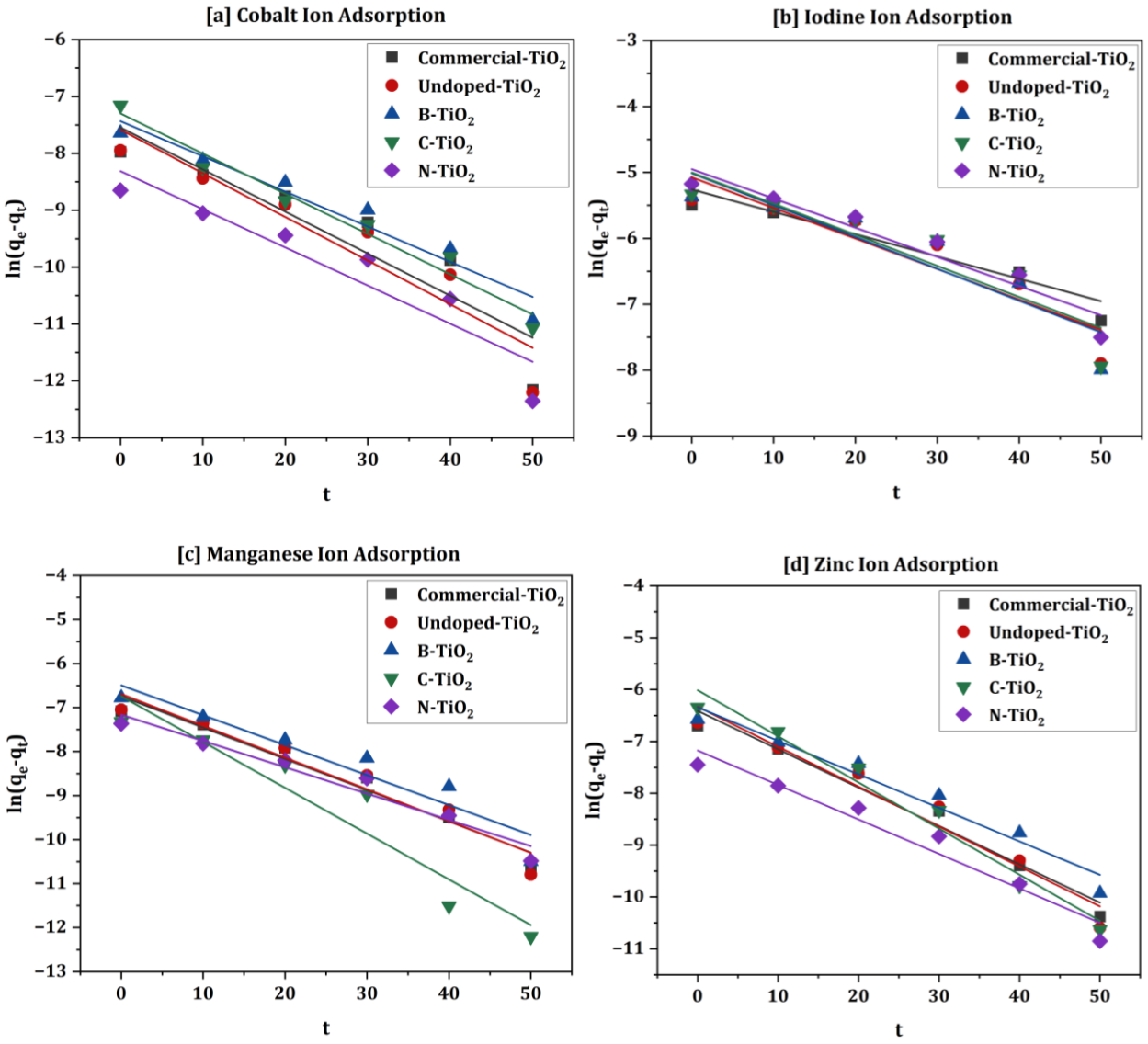

Figure 27: Pseudo-first order kinetics plot comparing (a) Cobalt Ion Adsorption, (b) Iodine Ion Adsorption, (c) Manganese Ion Adsorption, (d) Zinc Ion Adsorption of all samples

Figure 27 shows pseudo-first-order kinetics plots of commercial-TiO_2, undoped-TiO_2, B-doped TiO_2, C-doped TiO_2, and N-doped TiO_2 for four ion adsorptions, which were plotted by $\ln(q_e-q_t)$ vs time, t. The data were then linearly fitted, and the R^2 value was calculated from the linear fitting, as shown in Table 8.

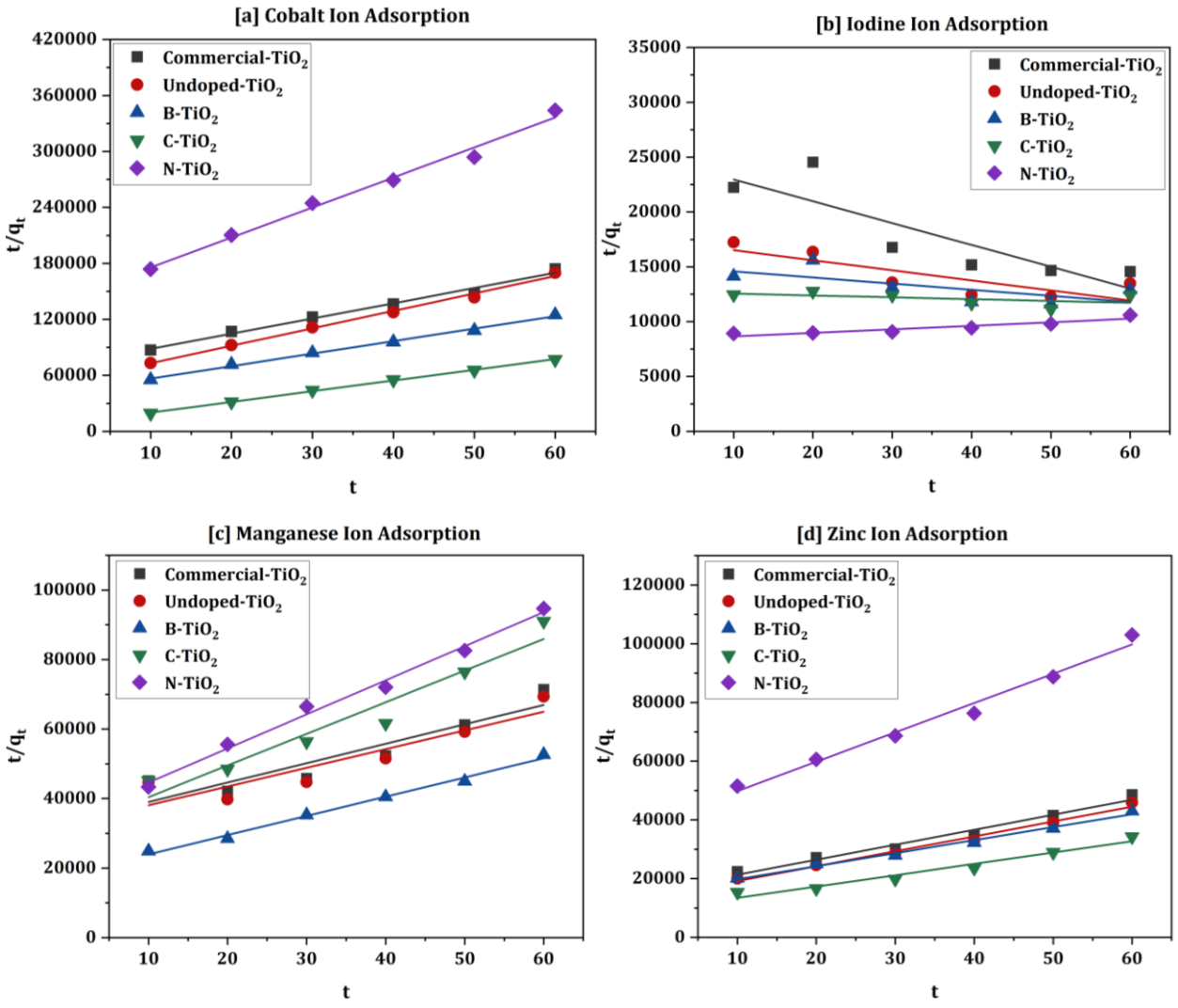

Figure 28: Pseudo-second order kinetics plot comparing (a) Cobalt Ion Adsorption, (b) Iodine Ion Adsorption, (c) Manganese Ion Adsorption, (d) Zinc Ion Adsorption of all samples

Figure 28 shows pseudo-second-order kinetics plots of commercial-TiO_2, undoped-TiO_2, B-doped TiO_2, C-doped TiO_2, and N-doped TiO_2 for four ion adsorptions, plotted as t/qt vs. time (t). The data were then linearly fitted, and the R^2 value was calculated from the linear fitting, as shown in Table 8.

Table 10: R^2 Values for Pseudo-First Order Kinetics and Pseudo-Second Order Kinetics of Ion Adsorption on Different TiO_2 Samples

Ion Adsorption	Commercial-TiO_2		Undoped-TiO_2		B-TiO_2		C-TiO_2		N-TiO_2	
	1st Order	2nd Order	1st Order	2nd Order	1st Order	2nd Order	1st Order	2nd Order	1st Order	2nd Order
Co^{2+}	0.842	0.986	0.886	0.9947	0.9468	0.996	0.97	0.999	0.8832	0.98873
I^-	0.8897	0.743	0.8563	0.6838	0.8407	0.481	0.84	0.2712	0.9272	0.86268
Mn^{2+}	0.9565	0.853	0.939	0.8369	0.9113	0.992	0.91	0.9401	0.9526	0.99133
Zn^{2+}	0.9677	0.972	0.9551	0.9846	0.9596	0.989	0.97	0.9529	0.9548	0.98004

Based on Table 8, the adsorption kinetics of various ions (Co, I, Mn, Zn) on different forms of TiO_2 (commercial, undoped, B-doped, C-doped, N-doped) were evaluated by fitting both pseudo-first-order and pseudo-second-order kinetic models. The selection of the best-fit model was determined by the highest R^2 value, as shown in Table 9, which indicates the best correlation between the experimental data and the kinetic model.

Table 11: Comparison of Pseudo-First-Order and Pseudo-Second-Order Kinetic Model Fits for Ion Adsorption on TiO_2 and Doped TiO_2 Materials Based on R^2 Values

Ion Adsorption	Commercial-TiO_2	Undoped-TiO_2	B-TiO_2	C-TiO_2	N-TiO_2
	Fitted Kinetics	Fitted Kinetics	Fitted Kinetics	Fitted Kinetics	Fitted Kinetics
Co	2nd Order	2nd Order	2nd Order	2nd Order	2nd Order
I	1st Order	1st Order	1st Order	1st Order	1st Order
Mn	1st Order	1st Order	2nd Order	2nd Order	2nd Order
Zn	2nd Order	2nd Order	2nd Order	1st Order	2nd Order

For certain ions and adsorbents (notably Co and Zn on most TiO_2 forms, and Mn on B-, N-, and undoped-TiO_2), the adsorption process consistently followed the pseudo-second-order kinetic model. This suggests that chemisorption, involving valence forces through sharing or exchange of electrons, is the dominant mechanism for these systems.

Dual Model Fit (First and Second Order):

In some cases, such as the adsorption of I and Mn ions on commercial-TiO_2 and C-TiO_2, both pseudo-first-order and pseudo-second-order models were applied. However, the model with the higher R^2 value was considered more appropriate. For these systems, the data may fit both models reasonably well, indicating that the adsorption process could involve both physisorption and chemisorption mechanisms, or that the system does not strictly follow a single kinetic pathway.

Material-Specific Trends:

Commercial-TiO_2 and C-TiO_2 showed both first- and second-order kinetics for certain ions, indicating a more complex adsorption mechanism. Undoped-TiO_2, B-TiO_2, and N-TiO_2 displayed a stronger tendency towards second-order kinetics, especially for Co, Mn, and Zn ions, reflecting enhanced chemisorption due to increased surface area or modified surface chemistry from doping.

CHAPTER 5:

CONCLUSION

In this work, undoped TiO_2 and non-metal-doped titanium dioxide (TiO_2) nanomaterials, i.e., B–TiO_2, C–TiO_2, and N–TiO_2, have been successfully synthesized using gel method employing relatively low-cost and readily available precursors. The structural, morphological, and optical properties of the produced nanoparticles were extensively characterized by XRD, FESEM, EDX, TEM, FTIR, UV–Vis, DLS, zeta potential, and AAS. The observations indicated that nonmetal-doped TiO_2 had a significant effect on crystal size, surface morphology, and light absorption behavior. Specifically, the carbon-doped and nitrogen-doped samples exhibited a lower particle size, a larger surface area, and an enhancement of the photocatalytic activity in the visible light region. Adsorption and photocatalytic experiments were performed with stable isotopes of the radionuclides, cobalt, iodine, manganese, and zinc, based on their chemical similarity to $^{60}Co^{2+}$, $^{131}I^{-}$, $^{54}Mn^{2+}$, and $^{65}Zn^{2+}$, respectively, to investigate the applicability of these materials series for the treatment of radioactive nuclear wastewater. This mimic methodology, although it does not involve real radioactive substances due to safety and facility limitations, has been scientifically proven to profile promising adsorbents and photocatalytic materials. Among all prepared nanoparticles, C and N-TiO_2 exhibit a good fit with each other. These results indicate that nonmetal-doped TiO_2 nanoparticles, particularly those doped with carbon and nitrogen, are prospective, cost-effective, and scalable candidates for treating radioactive wastewater. The zeta potential values of all the synthesized nanoparticles showed a negative surface charge in the aqueous medium, which was essential for the electrostatic attraction with positively charged metal ions of Co^{2+}, Mn^{2+}, and Zn^{2+}. Higher (more negative) specific surface area and zeta potential values in the doped samples, which may reflect better colloidal stability and enhanced surface reactivity, and hence could lead to improved radionuclide analogue removal efficiency. This study generally suggests an eco-friendly and effective approach for removing radionuclides from contaminated water; therefore, it could serve as a basis for studying real radioactive isotopes in controlled and well-equipped laboratory conditions.

REFERENCES

[1] I. Maamoun *et al.*, "Radionuclides Removal from Aqueous Solutions: A Mini Review on Using Different Sorbents," *Proceedings of International Exchange and Innovation Conference on Engineering & Sciences (IEICES)*, vol. 7, pp. 170–177, Oct. 2021, doi: 10.5109/4738585.

[2] K. H. Lieser, *Nuclear and radiochemistry: fundamentals and applications*, 2nd, rev. ed ed. Berlin New York: Wiley-VCH, 2001. doi: 10.1002/9783527612758.

[3] Z. Guo, Y. Chen, and N. L. Lu, *Multifunctional Nanocomposites for Energy and Environmental Applications*, 1st ed. Wiley, 2018. doi: 10.1002/9783527342501.

[4] *Management of low and intermediate level radioactive wastes with regard to their chemical toxicity*. Vienna: International Atomic Energy Agency, 2002.

[5] S. Liu, N. Wang, Y. Zhang, Y. Li, Z. Han, and P. Na, "Efficient removal of radioactive iodide ions from water by three-dimensional Ag2O–Ag/TiO2 composites under visible light irradiation," *Journal of Hazardous Materials*, vol. 284, pp. 171–181, Mar. 2015, doi: 10.1016/j.jhazmat.2014.10.054.

[6] P. Akhter, A. Arshad, A. Saleem, and M. Hussain, "Recent Development in Non-Metal-Doped Titanium Dioxide Photocatalysts for Different Dyes Degradation and the Study of Their Strategic Factors: A Review," *Catalysts*, vol. 12, no. 11, p. 1331, Oct. 2022, doi: 10.3390/catal12111331.

[7] H.-H. Cheng, S.-S. Chen, S.-Y. Yang, H.-M. Liu, and K.-S. Lin, "Sol-Gel Hydrothermal Synthesis and Visible Light Photocatalytic Degradation Performance of Fe/N Codoped TiO2 Catalysts," *Materials*, vol. 11, no. 6, p. 939, Jun. 2018, doi: 10.3390/ma11060939.

[8] J. N. Xu, W. X. Liu, P. Sun, M. Guan, and W. B. Cao, "Preparation of Fe/N Co-Doped TiO_2 Powders by Mild Hydrothermal Method," *MSF*, vol. 804, pp. 217–220, Oct. 2014, doi: 10.4028/www.scientific.net/MSF.804.217.

[9] M. Zhu *et al.*, "New Method to Synthesize S-Doped TiO_2 with Stable and Highly Efficient Photocatalytic Performance under Indoor Sunlight Irradiation," *ACS Sustainable Chem. Eng.*, vol. 3, no. 12, pp. 3123–3129, Dec. 2015, doi: 10.1021/acssuschemeng.5b01137.

[10] C. Negi *et al.*, “Carbon-doped titanium dioxide nanoparticles for visible light driven photocatalytic activity,” *Applied Surface Science*, vol. 554, p. 149553, Jul. 2021, doi: 10.1016/j.apsusc.2021.149553.

[11] N. O. Gopal *et al.*, “Visible Light Active Phosphorus-Doped TiO_2 Nanoparticles: An EPR Evidence for the Enhanced Charge Separation,” *J. Phys. Chem. C*, vol. 116, no. 30, pp. 16191–16197, Aug. 2012, doi: 10.1021/jp212346f.

[12] R. Ghosh Chaudhuri and S. Paria, “Visible light induced photocatalytic activity of sulfur doped hollow TiO2 nanoparticles, synthesized via a novel route,” *Dalton Trans.*, vol. 43, no. 14, p. 5526, 2014, doi: 10.1039/c3dt53311e.

[13] L. Cano-Casanova *et al.*, “Surface-Enriched Boron-Doped TiO_2 Nanoparticles as Photocatalysts for Propene Oxidation,” *ACS Appl. Nano Mater.*, vol. 5, no. 9, pp. 12527–12539, Sep. 2022, doi: 10.1021/acsanm.2c02217.

[14] P. Dao, K. Du, G. Liu, G. Li, M. Tayyib, and K. Wang, “Synthesis and photocatalytic properties of silicon-doped TiO2 nanotubes,” *Materials Letters*, vol. 354, p. 135322, Jan. 2024, doi: 10.1016/j.matlet.2023.135322.

[15] N. O. Eddy *et al.*, “Environmental and public health risk management, remediation and rehabilitation options for impacts of radionuclide mining,” *Discov Sustain*, vol. 6, no. 1, p. 209, Mar. 2025, doi: 10.1007/s43621-025-01047-6.

[16] R. Fukai and Y. Yokoyama, “Natural Radionuclides in the Environment,” in *The Natural Environment and the Biogeochemical Cycles*, vol. 1 / 1B, in The Handbook of Environmental Chemistry, vol. 1 / 1B. , Berlin, Heidelberg: Springer Berlin Heidelberg, 1982, pp. 47–60. doi: 10.1007/978-3-540-38597-4_2.

[17] World Health Organization, *Guidelines for drinking-water quality [electronic resource]: incorporating 1st and 2nd addenda,Vol.1, recommendations*, 3rd ed. Geneva: World Health Organization, 2008. Accessed: Jun. 25, 2025. [Online]. Available: https://iris.who.int/handle/10665/204411

[18] A. Altıkulaç, Ş. Turhan, and H. Gümüş, "The natural and artificial radionuclides in drinking water samples and consequent population doses," *Journal of Radiation Research and Applied Sciences*, vol. 8, no. 4, pp. 578–582, Oct. 2015, doi: 10.1016/j.jrras.2015.06.007.

[19] V. Saenko *et al.*, "The Chernobyl Accident and its Consequences," *Clinical Oncology*, vol. 23, no. 4, pp. 234–243, May 2011, doi: 10.1016/j.clon.2011.01.502.

[20] CONGRESSIONAL RESEARCH SERVICE, *NUCLEAR ENERGY POLICY*. S.l.: EISENBRAUNS, 2014.

[21] R. Prăvălie, "Nuclear Weapons Tests and Environmental Consequences: A Global Perspective," *AMBIO*, vol. 43, no. 6, pp. 729–744, Oct. 2014, doi: 10.1007/s13280-014-0491-1.

[22] S. Grande and S. Risica, "Radionuclides in drinking water: the recent legislative requirements of the European Union," *J. Radiol. Prot.*, vol. 35, no. 1, pp. 1–19, Mar. 2015, doi: 10.1088/0952-4746/35/1/1.

[23] M. Buzynnyi and L. Mykhailova, "Long term studying of uranium and radium-226 activity in drinking water in some regions of Ukraine and assessment of corresponding hypotetical irradiation doses," *Sci Rep*, vol. 14, no. 1, p. 2530, Jan. 2024, doi: 10.1038/s41598-024-53079-z.

[24] M. I. Balonov, "Internal Exposure of Populations to Long-Lived Radionuclides Released into the Environment," in *Novartis Foundation Symposia*, 1st ed., J. V. Lake, G. R. Bock, and G. Cardew, Eds., Wiley, 2007, pp. 120–140. doi: 10.1002/9780470515006.ch9.

[25] M. Pöschl and L. M. L. Nollet, *Radionuclide concentrations in food and the environment*. in Food science and technology. Boca Raton: CRC press, 2007.

[26] J. Guillén Gerada, Ed., *Radionuclides: sources, properties, and hazards*, Online-Ausg. in Physics research and technology. Hauppauge, NY: Nova Science Publishers, 2011.

[27] W. S. Osburn, "Primordial Radionuclides: Their Distribution, Movement, and Possible Effect Within Terrestrial Ecosystems," *Health Physics*, vol. 11, no. 12, pp. 1275–1295, Dec. 1965, doi: 10.1097/00004032-196512000-00005.

[28] N. E. Yanasak *et al.*, "Measurement of the Secondary Radionuclides^{10} Be,^{26} Al,^{36} Cl,^{54} Mn, and^{14} C and Implications for the Galactic Cosmic-Ray Age," *ApJ*, vol. 563, no. 2, pp. 768–792, Dec. 2001, doi: 10.1086/323842.

[29] A. P. Novikov, "Migration and concentration of artificial radionuclides in environmental objects," *Geochem. Int.*, vol. 48, no. 13, pp. 1263–1387, Dec. 2010, doi: 10.1134/S001670291013001X.

[30] M. Hatch and E. Cardis, "Somatic health effects of Chernobyl: 30 years on," *Eur J Epidemiol*, vol. 32, no. 12, pp. 1047–1054, Dec. 2017, doi: 10.1007/s10654-017-0303-6.

[31] C. Joshi, S. Dhanesar, J. Darko, A. Kerr, P. Vidyasagar, and Lj. Schreiner, "Practical and clinical considerations in Cobalt-60 tomotherapy," *J Med Phys*, vol. 34, no. 3, p. 137, 2009, doi: 10.4103/0971-6203.54847.

[32] M. Długosz-Lisiecka and K. Isajenko, "Am-241 in the urban air – Monitoring and simulation results," *Process Safety and Environmental Protection*, vol. 186, pp. 639–644, Jun. 2024, doi: 10.1016/j.psep.2024.03.124.

[33] F. Khechekhouche, A. Ararem, M. Salhi, H. Benkharfia, M. Kadouma, and M. Touiza, "Production of^{192} Ir sealed sources in Es Salam research reactor for non-destructive testing," *Radiochimica Acta*, vol. 111, no. 6, pp. 471–479, Jun. 2023, doi: 10.1515/ract-2022-0125.

[34] A. Ammar, A. Nouira, Z. El Mouridi, and S. Boughribil, "Recent trends in the phytoremediation of radionuclide contamination of soil by cesium and strontium: Sources, mechanisms and methods: A comprehensive review," *Chemosphere*, vol. 359, p. 142273, Jul. 2024, doi: 10.1016/j.chemosphere.2024.142273.

[35] D. A. DiLek, E. Eren BelgiN, and G. A. Ayçik, "Prediction of I-131 Influence in the Aegean Region by Chernobyl Accident Using the Ratio of I-129/I-127 in the Lake Sediments," *Iğdır Üniversitesi Fen Bilimleri Enstitüsü Dergisi*, vol. 12, no. 1, pp. 306–316, Mar. 2022, doi: 10.21597/jist.984099.

[36] L. S. Keith and O. M. Faroon, "Uranium," in *Handbook on the Toxicology of Metals*, Elsevier, 2022, pp. 885–936. doi: 10.1016/B978-0-12-822946-0.00032-5.

[37] A. M. Scott and L. Bodei, "Pharmacogenomics in Radionuclide Therapy: Impact on Response to Theranostics," *J Nucl Med*, vol. 62, no. 7, pp. 884–885, Jul. 2021, doi: 10.2967/jnumed.120.254995.

[38] K. Zaletel, A. Mihovec, and S. Gaberscek, "Characteristics of exposure to radioactive iodine during a nuclear incident," *Radiology and Oncology*, vol. 58, no. 4, pp. 459–468, Dec. 2024, doi: 10.2478/raon-2024-0051.

[39] B. Zheng *et al.*, "Radionuclides in marine food web along China's coastal waters: Activity, distribution and trophic level bio-magnification," *Environmental Research*, vol. 275, p. 121370, Jun. 2025, doi: 10.1016/j.envres.2025.121370.

[40] K. P. Pradhoshini *et al.*, "Biological effects of ionizing radiation on aquatic biota – A critical review," *Environmental Toxicology and Pharmacology*, vol. 99, p. 104091, Apr. 2023, doi: 10.1016/j.etap.2023.104091.

[41] E. Dufourcq Sekatcheff *et al.*, "Developing adverse outcome pathways to support radioecological risk assessment: challenges and insights," *Environmental Toxicology and Chemistry*, p. vgaf031, Jan. 2025, doi: 10.1093/etojnl/vgaf031.

[42] H. Funaki, H. Tsuji, T. Nakanishi, K. Yoshimura, K. Sakuma, and S. Hayashi, "Remobilisation of radiocaesium from bottom sediments to water column in reservoirs in Fukushima, Japan," *Science of The Total Environment*, vol. 812, p. 152534, Mar. 2022, doi: 10.1016/j.scitotenv.2021.152534.

[43] S. Kasar *et al.*, "Sorption-desorption coefficients of uranium in contaminated soils collected around Fukushima Daiichi Nuclear Power Station," *Journal of Environmental Radioactivity*, vol. 233, p. 106617, Jul. 2021, doi: 10.1016/j.jenvrad.2021.106617.

[44] A. Ivanets, A. Radkevich, I. Shashkova, N. Kitikova, A. Zarubo, and E. Venhlinskaya, "Study of dynamic adsorption and desorption kinetics of cesium, strontium, cobalt radionuclides on granular phosphate adsorbent," *J Radioanal Nucl Chem*, vol. 327, no. 3, pp. 1291–1298, Mar. 2021, doi: 10.1007/s10967-020-07584-w.

[45] J. N. Whetter, D. Śmiłowicz, and E. Boros, "Exploring Aqueous Coordination Chemistry of Highly Lewis Acidic Metals with Emerging Isotopes for Nuclear Medicine," *Acc. Chem. Res.*, vol. 57, no. 6, pp. 933–944, Mar. 2024, doi: 10.1021/acs.accounts.3c00781.

[46] E. Strub *et al.*, "Technetium - The Unknown Center of the Periodic Table," *Eur J Inorg Chem*, vol. 28, no. 9, p. e202400780, Mar. 2025, doi: 10.1002/ejic.202400780.

[47] A. J. Williamson, M. Binet, and C. Sergeant, "Radionuclide biogeochemistry: from bioremediation toward the treatment of aqueous radioactive effluents," *Critical Reviews in Biotechnology*, vol. 44, no. 4, pp. 698–716, May 2024, doi: 10.1080/07388551.2023.2194505.

[48] P. Baják *et al.*, "Refining the conceptual model for radionuclide mobility in groundwater in the vicinity of a Hungarian granitic complex using geochemical modeling," *Applied Geochemistry*, vol. 137, p. 105201, Feb. 2022, doi: 10.1016/j.apgeochem.2022.105201.

[49] Q. Tan *et al.*, "Mechanistic model for the cotransport of colloids and radionuclides in saturated porous systems based on the interaction forces between colloids," *Applied Geochemistry*, vol. 184, p. 106381, May 2025, doi: 10.1016/j.apgeochem.2025.106381.

[50] A. Scheklaukov, "Development and evaluation of new analytical concepts for the determination of ^{89}Sr and ^{90}Sr in a variety of applications to sample matrices with a high calcium content," 2023, doi: 10.5283/EPUB.54477.

[51] R. Lin *et al.*, "Targeted radioimmunotherapy with the iodine-131-labeled caerin 1.1 peptide for human anaplastic thyroid cancer in nude mice," *Ann Nucl Med*, vol. 35, no. 7, pp. 811–822, Jul. 2021, doi: 10.1007/s12149-021-01618-3.

[52] O. Yermishev, "Ecological and toxicological features of the effect of stable cesium on striated muscle tissue (myocardium and skeletal muscles) of mammals," *Regul. Mech. Biosyst.*, vol. 14, no. 3, pp. 415–423, Aug. 2023, doi: 10.15421/10.15421/022361.

[53] P. T. Greiner, R. York, and J. A. McGee, "When are fossil fuels displaced? An exploratory inquiry into the role of nuclear electricity production in the displacement of fossil fuels," *Heliyon*, vol. 8, no. 1, p. e08795, Jan. 2022, doi: 10.1016/j.heliyon.2022.e08795.

[54] A. Rehman, H. Ma, I. Ozturk, and M. Radulescu, "Revealing the dynamic effects of fossil fuel energy, nuclear energy, renewable energy, and carbon emissions on Pakistan's economic

growth," *Environ Sci Pollut Res*, vol. 29, no. 32, pp. 48784–48794, Jul. 2022, doi: 10.1007/s11356-022-19317-5.

[55] M. T. Kartal, "The role of consumption of energy, fossil sources, nuclear energy, and renewable energy on environmental degradation in top-five carbon producing countries," *Renewable Energy*, vol. 184, pp. 871–880, Jan. 2022, doi: 10.1016/j.renene.2021.12.022.

[56] T. Maystrenko and A. Rybak, "Radiation exposure and risk assessment to earthworms in areas contaminated with naturally occurring radionuclides," *Environ Monit Assess*, vol. 194, no. 10, p. 706, Oct. 2022, doi: 10.1007/s10661-022-10382-4.

[57] L. B. An *et al.*, "Activity Concentrations of Natural Radionuclides in Soil and Water Around Some Quarries and Potential Human Health Effects," *Water Air Soil Pollut*, vol. 234, no. 2, p. 122, Feb. 2023, doi: 10.1007/s11270-023-06147-5.

[58] M. B. Adedokun, M. A. Aweda, P. P. Maleka, R. I. Obed, and A. Z. Ibitoye, "Evaluation of natural radionuclides and associated radiation hazard indices in soil and water from selected vegetable farmlands in Lagos, Nigeria," *Environmental Forensics*, vol. 23, no. 3–4, pp. 301–313, Jul. 2022, doi: 10.1080/15275922.2020.1850557.

[59] M. Stylo, D. S. Alessi, P. P. Shao, J. S. Lezama-Pacheco, J. R. Bargar, and R. Bernier-Latmani, "Biogeochemical Controls on the Product of Microbial U(VI) Reduction," *Environ. Sci. Technol.*, vol. 47, no. 21, pp. 12351–12358, Nov. 2013, doi: 10.1021/es402631w.

[60] D. K. Singh, K. N. Hareendran, S. T., V. Kain, and G. K. Dey, "Development of a phosphate precipitation method for the recovery of uranium from lean tenor alkaline leach liquor," *Hydrometallurgy*, vol. 171, pp. 228–235, Aug. 2017, doi: 10.1016/j.hydromet.2017.05.021.

[61] P. Li *et al.*, "Highly Efficient Interception and Precipitation of Uranium(VI) from Aqueous Solution by Iron-Electrocoagulation Combined with Cooperative Chelation by Organic Ligands," *Environ. Sci. Technol.*, vol. 51, no. 24, pp. 14368–14378, Dec. 2017, doi: 10.1021/acs.est.7b05288.

[62] X. Zhang *et al.*, "Selective separation of metals from wastewater using sulfide precipitation: A critical review in agents, operational factors and particle aggregation," *Journal of*

Environmental Management, vol. 344, p. 118462, Oct. 2023, doi: 10.1016/j.jenvman.2023.118462.

[63] K. Zhu *et al.*, "Gamma-ferric oxide nanoparticles decoration onto porous layered double oxide belts for efficient removal of uranyl," *Journal of Colloid and Interface Science*, vol. 535, pp. 265–275, Feb. 2019, doi: 10.1016/j.jcis.2018.10.005.

[64] X. Wang *et al.*, "Retraction notice to 'High sorption of U(VI) on graphene oxides studied by batch experimental and theoretical calculations' [Chem. Eng. J. 287 (2015) 448–455]," *Chemical Engineering Journal*, vol. 390, p. 124272, Jun. 2020, doi: 10.1016/j.cej.2020.124272.

[65] M. I. Ojovan, A. Pankov, and W. E. Lee, "The ion exchange phase in corrosion of nuclear waste glasses," *Journal of Nuclear Materials*, vol. 358, no. 1, pp. 57–68, Nov. 2006, doi: 10.1016/j.jnucmat.2006.06.016.

[66] S. Tripatanasuwan, Z. Zhong, and D. H. Reneker, "Effect of evaporation and solidification of the charged jet in electrospinning of poly(ethylene oxide) aqueous solution," *Polymer*, vol. 48, no. 19, pp. 5742–5746, Sep. 2007, doi: 10.1016/j.polymer.2007.07.045.

[67] J. Shen and A. Schäfer, "Removal of fluoride and uranium by nanofiltration and reverse osmosis: A review," *Chemosphere*, vol. 117, pp. 679–691, Dec. 2014, doi: 10.1016/j.chemosphere.2014.09.090.

[68] P. Sylvester, T. Milner, and J. Jensen, "Radioactive liquid waste treatment at Fukushima Daiichi," *J of Chemical Tech & Biotech*, vol. 88, no. 9, pp. 1592–1596, Sep. 2013, doi: 10.1002/jctb.4141.

[69] I. Stenina, D. Golubenko, V. Nikonenko, and A. Yaroslavtsev, "Selectivity of Transport Processes in Ion-Exchange Membranes: Relationship with the Structure and Methods for Its Improvement," *IJMS*, vol. 21, no. 15, p. 5517, Aug. 2020, doi: 10.3390/ijms21155517.

[70] L. K. Wang, D. A. Vaccari, Y. Li, and N. K. Shammas, "Chemical Precipitation," in *Physicochemical Treatment Processes*, L. K. Wang, Y.-T. Hung, and N. K. Shammas, Eds., Totowa, NJ: Humana Press, 2005, pp. 141–197. doi: 10.1385/1-59259-820-x:141.

[71] I. G. A.-A. Rashed, H. A. Afify, A. E.-M. Ahmed, and M. A. E.-S. Ayoub, "Optimization of chemical precipitation to improve the primary treatment of wastewater," *Desalination and*

Water Treatment, vol. 51, no. 37–39, pp. 7048–7056, Nov. 2013, doi: 10.1080/19443994.2013.792147.

[72] S. B. Pillai and N. V. Thombre, "Coagulation, Flocculation, and Precipitation in Water and Used Water Purification," in *Handbook of Water and Used Water Purification*, J. Lahnsteiner, Ed., Cham: Springer International Publishing, 2023, pp. 1–25. doi: 10.1007/978-3-319-66382-1_63-1.

[73] D. Rana, T. Matsuura, M. A. Kassim, and A. F. Ismail, "Radioactive decontamination of water by membrane processes — A review," *Desalination*, vol. 321, pp. 77–92, Jul. 2013, doi: 10.1016/j.desal.2012.11.007.

[74] X. Deng, Y. Ge, Y. He, and X. Cui, "A low-cost photo-evaporation inorganic membrane preparation and treatment of the simulated high salinity radioactive waste water," *Journal of Hazardous Materials*, vol. 424, p. 127433, Feb. 2022, doi: 10.1016/j.jhazmat.2021.127433.

[75] C. Hou, W. Lin, L. Yang, and H. Zhang, "Experimental performance evaluation and model-based optimal design of a mechanical vapour recompression system for radioactive wastewater treatment," *Energy Conversion and Management*, vol. 252, p. 115087, Jan. 2022, doi: 10.1016/j.enconman.2021.115087.

[76] K. Yu *et al.*, "Superhydrophilic and highly elastic monolithic sponge for efficient solar-driven radioactive wastewater treatment under one sun," *Journal of Hazardous Materials*, vol. 392, p. 122350, Jun. 2020, doi: 10.1016/j.jhazmat.2020.122350.

[77] V. V. Milyutin, N. A. Nekrasova, V. O. Kaptakov, and E. A. Kozlitin, "Adsorption techniques for decontaminating liquid radioactive waste and radionuclide-contaminated natural water," *Adsorption*, vol. 29, no. 5–6, pp. 323–334, Aug. 2023, doi: 10.1007/s10450-023-00407-w.

[78] A. J. Francis, "Biotechnology of Radioactive Wastes: A General Overview," in *Biotechnology for Waste Management and Site Restoration*, C. Ronneau and O. Bitchaeva, Eds., Dordrecht: Springer Netherlands, 1997, pp. 19–28. doi: 10.1007/978-94-009-1467-4_3.

[79] C. Ding, W. Cheng, and X. Nie, "Microorganisms and radionuclides," in *Interface Science and Technology*, vol. 29, Elsevier, 2019, pp. 107–139. doi: 10.1016/B978-0-08-102727-1.00003-0.

[80] P. Kumar, S. Yadav, and A. Yadav, "Radioactive waste minimization and management," in *Green Chemistry Approaches to Environmental Sustainability*, Elsevier, 2024, pp. 165–184. doi: 10.1016/B978-0-443-18959-3.00003-3.

[81] E. R. Vance, B. D. Begg, and D. J. Gregg, "Immobilization of high-level radioactive waste and used nuclear fuel for safe disposal in geological repository systems," in *Geological Repository Systems for Safe Disposal of Spent Nuclear Fuels and Radioactive Waste*, Elsevier, 2017, pp. 269–295. doi: 10.1016/B978-0-08-100642-9.00010-4.

[82] N. Yanikomer, S. Asal, S. Haciyakupoglu, and S. A. Erenturk, "New Solidification Materials in Nuclear Waste Management," *IJET*, vol. 2, no. 2, p. 76, Jun. 2016, doi: 10.19072/ijet.54627.

[83] J.-H. Jeon, J.-H. Lee, W.-C. Lee, S.-W. Lee, and S.-O. Kim, "Solidification of Radioactive Wastes Using Recycled Cement Originating from Decommissioned Nuclear-Energy Facilities," *Applied Sciences*, vol. 14, no. 5, p. 1781, Feb. 2024, doi: 10.3390/app14051781.

[84] L. R. Khanal, J. A. Sundararajan, and Y. Qiang, "Advanced Nanomaterials for Nuclear Energy and Nanotechnology," *Energy Tech*, vol. 8, no. 3, p. 1901070, Mar. 2020, doi: 10.1002/ente.201901070.

[85] T. Zhang *et al.*, "*In situ* remediation of subsurface contamination: opportunities and challenges for nanotechnology and advanced materials," *Environ. Sci.: Nano*, vol. 6, no. 5, pp. 1283–1302, 2019, doi: 10.1039/C9EN00143C.

[86] M. T. Amin, A. A. Alazba, and U. Manzoor, "A Review of Removal of Pollutants from Water/Wastewater Using Different Types of Nanomaterials," *Advances in Materials Science and Engineering*, vol. 2014, pp. 1–24, 2014, doi: 10.1155/2014/825910.

[87] M. G. Lines, "Nanomaterials for practical functional uses," *Journal of Alloys and Compounds*, vol. 449, no. 1–2, pp. 242–245, Jan. 2008, doi: 10.1016/j.jallcom.2006.02.082.

[88] E. L. Dreizin, "Metal-based reactive nanomaterials," *Progress in Energy and Combustion Science*, vol. 35, no. 2, pp. 141–167, Apr. 2009, doi: 10.1016/j.pecs.2008.09.001.

[89] H. F. Lecoanet, J.-Y. Bottero, and M. R. Wiesner, "Laboratory Assessment of the Mobility of Nanomaterials in Porous Media," *Environ. Sci. Technol.*, vol. 38, no. 19, pp. 5164–5169, Oct. 2004, doi: 10.1021/es0352303.

[90] A. Shaji and A. K. Zachariah, "Surface Area Analysis of Nanomaterials," in *Thermal and Rheological Measurement Techniques for Nanomaterials Characterization*, Elsevier, 2017, pp. 197–231. doi: 10.1016/B978-0-323-46139-9.00009-8.

[91] X. Li *et al.*, "Effects of physicochemical properties of nanomaterials on their toxicity: Effects of Physicochemical Properties of Nanomaterials on Their Toxicity," *J. Biomed. Mater. Res.*, vol. 103, no. 7, pp. 2499–2507, Jul. 2015, doi: 10.1002/jbm.a.35384.

[92] L. Giraldo, A. Erto, and J. C. Moreno-Piraján, "Magnetite nanoparticles for removal of heavy metals from aqueous solutions: synthesis and characterization," *Adsorption*, vol. 19, no. 2–4, pp. 465–474, Apr. 2013, doi: 10.1007/s10450-012-9468-1.

[93] R. Wang, J. Lou, J. Fang, J. Cai, Z. Hu, and P. Sun, "Effects of heavy metals and metal (oxide) nanoparticles on enhanced biological phosphorus removal," *Reviews in Chemical Engineering*, vol. 36, no. 8, pp. 947–970, Nov. 2020, doi: 10.1515/revce-2018-0076.

[94] C. Prasse and T. Ternes, "Removal of Organic and Inorganic Pollutants and Pathogens from Wastewater and Drinking Water Using Nanoparticles – A Review," in *Nanoparticles in the Water Cycle*, F. H. Frimmel and R. Niessner, Eds., Berlin, Heidelberg: Springer Berlin Heidelberg, 2010, pp. 55–79. doi: 10.1007/978-3-642-10318-6_5.

[95] N. B. Singh, R. G. Chaudhary, and N. Singh, "Nano-Based Adsorbents for Wastewater Treatment," in *Nanotechnology*, M. F. Desimone, R. B. Jotania, R. B. Khomane, and R. G. Chaudhary, Eds., in Nanotechnology in the Life Sciences. , Cham: Springer Nature Switzerland, 2025, pp. 265–286. doi: 10.1007/978-3-031-86508-4_12.

[96] J. A. Naser, Z. W. Ahmed, and E. H. Ali, "Nanomaterials usage as adsorbents for the pollutants removal from wastewater; a review," *Materials Today: Proceedings*, vol. 42, pp. 2590–2595, 2021, doi: 10.1016/j.matpr.2020.12.584.

[97] J. N. Tiwari, R. N. Tiwari, and K. S. Kim, "Zero-dimensional, one-dimensional, two-dimensional and three-dimensional nanostructured materials for advanced electrochemical energy

devices," *Progress in Materials Science*, vol. 57, no. 4, pp. 724–803, May 2012, doi: 10.1016/j.pmatsci.2011.08.003.

[98] Y. Li, X.-Y. Yang, Y. Feng, Z.-Y. Yuan, and B.-L. Su, "One-Dimensional Metal Oxide Nanotubes, Nanowires, Nanoribbons, and Nanorods: Synthesis, Characterizations, Properties and Applications," *Critical Reviews in Solid State and Materials Sciences*, vol. 37, no. 1, pp. 1–74, Jan. 2012, doi: 10.1080/10408436.2011.606512.

[99] H. Zhang, "Ultrathin Two-Dimensional Nanomaterials," *ACS Nano*, vol. 9, no. 10, pp. 9451–9469, Oct. 2015, doi: 10.1021/acsnano.5b05040.

[100] R. K. Joshi and J. J. Schneider, "Assembly of one dimensional inorganic nanostructures into functional 2D and 3D architectures. Synthesis, arrangement and functionality," *Chem. Soc. Rev.*, vol. 41, no. 15, p. 5285, 2012, doi: 10.1039/c2cs35089k.

[101] T. J. Mays, "A new classification of pore sizes," in *Studies in Surface Science and Catalysis*, vol. 160, Elsevier, 2007, pp. 57–62. doi: 10.1016/S0167-2991(07)80009-7.

[102] M. P. Attfield, "Microporous Materials," *Science Progress*, vol. 85, no. 4, pp. 319–345, Nov. 2002, doi: 10.3184/003685002783238771.

[103] D. M. Antonelli and J. Y. Ying, "Mesoporous materials," *Current Opinion in Colloid & Interface Science*, vol. 1, no. 4, pp. 523–529, Aug. 1996, doi: 10.1016/S1359-0294(96)80122-1.

[104] A. Vinu, T. Mori, and K. Ariga, "New families of mesoporous materials," *Science and Technology of Advanced Materials*, vol. 7, no. 8, pp. 753–771, Jan. 2006, doi: 10.1016/j.stam.2006.10.007.

[105] F. Wen and W. Liu, "Three-dimensional ordered macroporous materials for photocatalysis: design and applications," *J. Mater. Chem. A*, vol. 9, no. 34, pp. 18129–18147, 2021, doi: 10.1039/D1TA04127D.

[106] L. Dai, D. W. Chang, J. Baek, and W. Lu, "Carbon Nanomaterials for Advanced Energy Conversion and Storage," *Small*, vol. 8, no. 8, pp. 1130–1166, Apr. 2012, doi: 10.1002/smll.201101594.

[107] N. Choudhary, S. Hwang, and W. Choi, "Carbon Nanomaterials: A Review," in *Handbook of Nanomaterials Properties*, B. Bhushan, D. Luo, S. R. Schricker, W. Sigmund, and S. Zauscher, Eds., Berlin, Heidelberg: Springer Berlin Heidelberg, 2014, pp. 709–769. doi: 10.1007/978-3-642-31107-9_37.

[108] H. Kamyab *et al.*, "Exploring the potential of metal and metal oxide nanomaterials for sustainable water and wastewater treatment: A review of their antimicrobial properties," *Chemosphere*, vol. 335, p. 139103, Sep. 2023, doi: 10.1016/j.chemosphere.2023.139103.

[109] A. B. Sengul and E. Asmatulu, "Toxicity of metal and metal oxide nanoparticles: a review," *Environ Chem Lett*, vol. 18, no. 5, pp. 1659–1683, Sep. 2020, doi: 10.1007/s10311-020-01033-6.

[110] A. C. Grimsdale and K. Müllen, "The Chemistry of Organic Nanomaterials," *Angew Chem Int Ed*, vol. 44, no. 35, pp. 5592–5629, Sep. 2005, doi: 10.1002/anie.200500805.

[111] K. Khalid *et al.*, "Advanced in developmental organic and inorganic nanomaterial: a review," *Bioengineered*, vol. 11, no. 1, pp. 328–355, Jan. 2020, doi: 10.1080/21655979.2020.1736240.

[112] D. Tasis, N. Tagmatarchis, A. Bianco, and M. Prato, "Chemistry of Carbon Nanotubes," *Chem. Rev.*, vol. 106, no. 3, pp. 1105–1136, Mar. 2006, doi: 10.1021/cr050569o.

[113] X. Zhang and Y. Liu, "Nanomaterials for radioactive wastewater decontamination," *Environ. Sci.: Nano*, vol. 7, no. 4, pp. 1008–1040, 2020, doi: 10.1039/C9EN01341E.

[114] K. E. Geckeler and H. Nishide, Eds., *Advanced Nanomaterials*, 1st ed. Wiley, 2009. doi: 10.1002/9783527628940.

[115] Á. Kukovecz, G. Kozma, and Z. Kónya, "Multi-Walled Carbon Nanotubes," in *Springer Handbook of Nanomaterials*, R. Vajtai, Ed., Berlin, Heidelberg: Springer Berlin Heidelberg, 2013, pp. 147–188. doi: 10.1007/978-3-642-20595-8_5.

[116] T. Saito, K. Matsushige, and K. Tanaka, "Chemical treatment and modification of multi-walled carbon nanotubes," *Physica B: Condensed Matter*, vol. 323, no. 1–4, pp. 280–283, Oct. 2002, doi: 10.1016/S0921-4526(02)00999-7.

[117] C. L. Chen, X. K. Wang, and M. Nagatsu, "Europium Adsorption on Multiwall Carbon Nanotube/Iron Oxide Magnetic Composite in the Presence of Polyacrylic Acid," *Environ. Sci. Technol.*, vol. 43, no. 7, pp. 2362–2367, Apr. 2009, doi: 10.1021/es803018a.

[118] Q. H. Fan, D. D. Shao, J. Hu, C. L. Chen, W. S. Wu, and X. K. Wang, "Adsorption of humic acid and Eu(III) to multi-walled carbon nanotubes: Effect of pH, ionic strength and counterion effect," *Radiochimica Acta*, vol. 97, no. 3, Jan. 2009, doi: 10.1524/ract.2009.1586.

[119] P. Liu *et al.*, "Adsorption of thorium(IV) on magnetic multi-walled carbon nanotubes," *Sci. China Chem.*, vol. 57, no. 11, pp. 1483–1490, Nov. 2014, doi: 10.1007/s11426-014-5204-x.

[120] Y. Zheng, J. Qiao, J. Yuan, J. Shen, A. Wang, and L. Niu, "Electrochemical Removal of Radioactive Cesium from Nuclear Waste Using the Dendritic Copper Hexacyanoferrate/Carbon Nanotube Hybrids," *Electrochimica Acta*, vol. 257, pp. 172–180, Dec. 2017, doi: 10.1016/j.electacta.2017.09.179.

[121] C. Su and K. P. Loh, "Carbocatalysts: Graphene Oxide and Its Derivatives," *Acc. Chem. Res.*, vol. 46, no. 10, pp. 2275–2285, Oct. 2013, doi: 10.1021/ar300118v.

[122] A. Yu. Romanchuk, A. S. Slesarev, S. N. Kalmykov, D. V. Kosynkin, and J. M. Tour, "Graphene oxide for effective radionuclide removal," *Phys. Chem. Chem. Phys.*, vol. 15, no. 7, p. 2321, 2013, doi: 10.1039/c2cp44593j.

[123] Z. Li *et al.*, "Uranium(VI) adsorption on graphene oxide nanosheets from aqueous solutions," *Chemical Engineering Journal*, vol. 210, pp. 539–546, Nov. 2012, doi: 10.1016/j.cej.2012.09.030.

[124] X. Liu, J. Sun, X. Xu, A. Alsaedi, T. Hayat, and J. Li, "Adsorption and desorption of U(VI) on different-size graphene oxide," *Chemical Engineering Journal*, vol. 360, pp. 941–950, Mar. 2019, doi: 10.1016/j.cej.2018.04.050.

[125] Department of Chemistry, Illinois Institute of Technology, 3101 South Dearborn Street, Chicago, IL 60616, USA, H. Liu, School of Nuclear Science and Technology, University of South China, Hengyang, 421001, China, Y. Mao, and Department of Chemistry, Illinois Institute of Technology, 3101 South Dearborn Street, Chicago, IL 60616, USA, "Graphene Oxide-based

Nanomaterials for Uranium Adsorptive Uptake," *ES Mater. Manuf.*, 2021, doi: 10.30919/esmm5f453.

[126] Y.-Y. Chen, S.-H. Yu, Q.-Z. Yao, S.-Q. Fu, and G.-T. Zhou, "One-step synthesis of Ag2O@Mg(OH)2 nanocomposite as an efficient scavenger for iodine and uranium," *Journal of Colloid and Interface Science*, vol. 510, pp. 280–291, Jan. 2018, doi: 10.1016/j.jcis.2017.09.073.

[127] M. Y. Li *et al.*, "Out-of-Substrate Ag–Ag_2 O Nanoplates: Surfactantless Photochemical Synthesis, Structural Evolution, and Mechanistic Study," *ACS Omega*, vol. 1, no. 4, pp. 696–705, Oct. 2016, doi: 10.1021/acsomega.6b00149.

[128] S. M. Siddeeg, M. A. Tahoon, N. S. Alsaiari, M. Shabbir, and F. B. Rebah, "Application of Functionalized Nanomaterials as Effective Adsorbents for the Removal of Heavy Metals from Wastewater: A Review," *CAC*, vol. 17, no. 1, pp. 4–22, Dec. 2020, doi: 10.2174/1573411016999200719231712.

[129] M. F. Attallah, S. E. Rizk, and E. M. El Afifi, "Efficient removal of iodine and chromium as anionic species from radioactive liquid waste using prepared iron oxide nanofibers," *J Radioanal Nucl Chem*, vol. 317, no. 2, pp. 933–945, Aug. 2018, doi: 10.1007/s10967-018-5938-6.

[130] A. M. Muliwa, T. Y. Leswifi, M. S. Onyango, and A. Maity, "Magnetic adsorption separation (MAS) process: An alternative method of extracting Cr(VI) from aqueous solution using polypyrrole coated Fe 3 O 4 nanocomposites," *Separation and Purification Technology*, vol. 158, pp. 250–258, Jan. 2016, doi: 10.1016/j.seppur.2015.12.021.

[131] H. Shagholani, M. T. Goldani, E. F. Talooki, A. Y. Lehi, and M. Aliabadi, "Evaluative study on supercapacitance behaviors of polypyrrole-based ternary nanocomposite electrodes," *Ionics*, Jun. 2025, doi: 10.1007/s11581-025-06448-1.

[132] F.-L. Fan *et al.*, "Rapid removal of uranium from aqueous solutions using magnetic Fe3O4@SiO2 composite particles," *Journal of Environmental Radioactivity*, vol. 106, pp. 40–46, Apr. 2012, doi: 10.1016/j.jenvrad.2011.11.003.

[133] S.-H. Wu, C.-Y. Mou, and H.-P. Lin, "Synthesis of mesoporous silica nanoparticles," *Chem. Soc. Rev.*, vol. 42, no. 9, p. 3862, 2013, doi: 10.1039/c3cs35405a.

[134] Y. Wang *et al.*, "Characterizations and catalytic properties of Cr-MCM-41 prepared by direct hydrothermal synthesis and template-ion exchange," *Journal of Catalysis*, vol. 220, no. 2, pp. 347–357, Dec. 2003, doi: 10.1016/S0021-9517(03)00278-1.

[135] Y. Jung, S. Kim, S.-J. Park, and J. M. Kim, "Application of polymer-modified nanoporous silica to adsorbents of uranyl ions," *Colloids and Surfaces A: Physicochemical and Engineering Aspects*, vol. 313–314, pp. 162–166, Feb. 2008, doi: 10.1016/j.colsurfa.2007.04.087.

[136] S. Yang, J. Qian, L. Kuang, and D. Hua, "Ion-Imprinted Mesoporous Silica for Selective Removal of Uranium from Highly Acidic and Radioactive Effluent," *ACS Appl. Mater. Interfaces*, vol. 9, no. 34, pp. 29337–29344, Aug. 2017, doi: 10.1021/acsami.7b09419.

[137] F. Fan *et al.*, "Highly selective separation of medical isotope 99mTc from irradiated 100Mo target using PEG-based resins," *J Radioanal Nucl Chem*, vol. 332, no. 4, pp. 1113–1123, Apr. 2023, doi: 10.1007/s10967-023-08771-1.

[138] S. Wang, L. Tan, J. Jiang, J. Chen, and L. Feng, "Preparation and characterization of nanosized TiO2 powder as an inorganic adsorbent for aqueous radionuclide Co(II) ions," *J Radioanal Nucl Chem*, vol. 295, no. 2, pp. 1305–1312, Feb. 2013, doi: 10.1007/s10967-012-2296-7.

[139] M. Olsson, A.-M. Jakobsson, and Y. Albinsson, "Sorption of Pu(VI) onto TiO2," *Journal of Colloid and Interface Science*, vol. 266, no. 2, pp. 269–275, Oct. 2003, doi: 10.1016/S0021-9797(03)00756-2.

[140] X. Tan, M. Fang, J. Li, Y. Lu, and X. Wang, "Adsorption of Eu(III) onto TiO2: Effect of pH, concentration, ionic strength and soil fulvic acid," *Journal of Hazardous Materials*, vol. 168, no. 1, pp. 458–465, Aug. 2009, doi: 10.1016/j.jhazmat.2009.02.051.

[141] X. Tan, X. Wang, M. Fang, and C. Chen, "Sorption and desorption of Th(IV) on nanoparticles of anatase studied by batch and spectroscopy methods," *Colloids and Surfaces A: Physicochemical and Engineering Aspects*, vol. 296, no. 1–3, pp. 109–116, Mar. 2007, doi: 10.1016/j.colsurfa.2006.09.032.

[142] J. Sangeetha, M. David, J. Naik, D. Thangadurai, S. S. Dabire, and S. C. Thimmappa, "Removal of Radioactive Wastes Using Nanomaterials," in *Handbook of Nanomaterials and*

Nanocomposites for Energy and Environmental Applications, O. V. Kharissova, L. M. Torres-Martínez, and B. I. Kharisov, Eds., Cham: Springer International Publishing, 2021, pp. 1291–1308. doi: 10.1007/978-3-030-36268-3_80.

[143] T. A. Todd, K. N. Brewer, D. J. Wood, P. A. Tullock, N. R. Mann, and L. G. Olson, "EVALUATION AND TESTING OF INORGANIC ION EXCHANGE SORBENTS FOR THE REMOVAL OF CESIUM-137 FROM ACTUAL IDAHO NUCLEAR TECHNOLOGY AND ENGINEERING CENTER ACIDIC TANK WASTE," *Separation Science and Technology*, vol. 36, no. 5–6, pp. 999–1016, Jun. 2001, doi: 10.1081/SS-100103633.

[144] D. Yang, H. Liu, Z. Zheng, S. Sarina, and H. Zhu, "Titanate-based adsorbents for radioactive ions entrapment from water," *Nanoscale*, vol. 5, no. 6, p. 2232, 2013, doi: 10.1039/c3nr33622k.

[145] Y. Salwadi and S. K. Kurapati, "The Role of Nanomaterials in Radioactive Waste Reduction and Decontamination: A Concise Review," in *Recent Trends in Nanotechnology for Sustainable Living and Environment*, R. Mukherjee, C. Janiak, Z. Khan, S. Chatterjee, B. Roy, S. Ghosh, and K. Etika, Eds., in Lecture Notes in Mechanical Engineering. , Singapore: Springer Nature Singapore, 2023, pp. 141–157. doi: 10.1007/978-981-99-3386-0_12.

[146] T. Nishikawa, T. Nakajima, and Y. Shinohara, "An exploratory study on effect of the isomorphic replacement of Ti 4+ ions by various metal ions on the light absorption character of TiO 2," *Journal of Molecular Structure: THEOCHEM*, vol. 545, no. 1–3, pp. 67–74, Jul. 2001, doi: 10.1016/S0166-1280(01)00394-3.

[147] P. S. Basavarajappa, S. B. Patil, N. Ganganagappa, K. R. Reddy, A. V. Raghu, and Ch. V. Reddy, "Recent progress in metal-doped TiO2, non-metal doped/codoped TiO2 and TiO2 nanostructured hybrids for enhanced photocatalysis," *International Journal of Hydrogen Energy*, vol. 45, no. 13, pp. 7764–7778, Mar. 2020, doi: 10.1016/j.ijhydene.2019.07.241.

[148] S. Chang and W. Liu, "The roles of surface-doped metal ions (V, Mn, Fe, Cu, Ce, and W) in the interfacial behavior of TiO2 photocatalysts," *Applied Catalysis B: Environmental*, vol. 156–157, pp. 466–475, Sep. 2014, doi: 10.1016/j.apcatb.2014.03.044.

[149] F. Chekin, S. Bagheri, and S. B. Abd Hamid, "Synthesis of Pt doped TiO2 nanoparticles: Characterization and application for electrocatalytic oxidation of l-methionine," *Sensors and Actuators B: Chemical*, vol. 177, pp. 898–903, Feb. 2013, doi: 10.1016/j.snb.2012.12.002.

[150] J. Vargas Hernández, S. Coste, A. García Murillo, F. Carrillo Romo, and A. Kassiba, "Effects of metal doping (Cu, Ag, Eu) on the electronic and optical behavior of nanostructured TiO2," *Journal of Alloys and Compounds*, vol. 710, pp. 355–363, Jul. 2017, doi: 10.1016/j.jallcom.2017.03.275.

[151] J. Ohyama, A. Yamamoto, K. Teramura, T. Shishido, and T. Tanaka, "Modification of Metal Nanoparticles with TiO_2 and Metal−Support Interaction in Photodeposition," *ACS Catal.*, vol. 1, no. 3, pp. 187–192, Mar. 2011, doi: 10.1021/cs100072k.

[152] J. P. Holmberg, E. Ahlberg, J. Bergenholtz, M. Hassellöv, and Z. Abbas, "Surface charge and interfacial potential of titanium dioxide nanoparticles: Experimental and theoretical investigations," *Journal of Colloid and Interface Science*, vol. 407, pp. 168–176, Oct. 2013, doi: 10.1016/j.jcis.2013.06.015.

[153] R. Ravi and A. K. Golder, "A tuneable bioinspired process of Pt-doping in TiO2 for improved photoelectrochemical and photocatalytic functionalities," *Colloids and Surfaces A: Physicochemical and Engineering Aspects*, vol. 663, p. 131034, Apr. 2023, doi: 10.1016/j.colsurfa.2023.131034.

[154] T. Ali, A. Ahmed, U. Alam, I. Uddin, P. Tripathi, and M. Muneer, "Enhanced photocatalytic and antibacterial activities of Ag-doped TiO2 nanoparticles under visible light," *Materials Chemistry and Physics*, vol. 212, pp. 325–335, Jun. 2018, doi: 10.1016/j.matchemphys.2018.03.052.

[155] G. Colón, M. Maicu, M. C. Hidalgo, and J. A. Navío, "Cu-doped TiO2 systems with improved photocatalytic activity," *Applied Catalysis B: Environmental*, vol. 67, no. 1–2, pp. 41–51, Sep. 2006, doi: 10.1016/j.apcatb.2006.03.019.

[156] T. Ali *et al.*, "Photocatalytic performance of Fe-doped TiO_2 nanoparticles under visible-light irradiation," *Mater. Res. Express*, vol. 4, no. 1, p. 015022, Jan. 2017, doi: 10.1088/2053-1591/aa576d.

[157] X. Gong *et al.*, "Introduction of cation vacancies and iron doping into TiO2 enabling efficient uranium photoreduction," *Journal of Hazardous Materials*, vol. 423, p. 126935, Feb. 2022, doi: 10.1016/j.jhazmat.2021.126935.

[158] R. Beranek *et al.*, "Exploring the electronic structure of nitrogen-modified TiO2 photocatalysts through photocurrent and surface photovoltage studies," *Chemical Physics*, vol. 339, no. 1–3, pp. 11–19, Oct. 2007, doi: 10.1016/j.chemphys.2007.05.022.

[159] X. Pan, M.-Q. Yang, X. Fu, N. Zhang, and Y.-J. Xu, "Defective TiO2 with oxygen vacancies: synthesis, properties and photocatalytic applications," *Nanoscale*, vol. 5, no. 9, p. 3601, 2013, doi: 10.1039/c3nr00476g.

[160] Y. Cong, J. Zhang, F. Chen, and M. Anpo, "Synthesis and Characterization of Nitrogen-Doped TiO_2 Nanophotocatalyst with High Visible Light Activity," *J. Phys. Chem. C*, vol. 111, no. 19, pp. 6976–6982, May 2007, doi: 10.1021/jp0685030.

[161] T. Ohno, M. Akiyoshi, T. Umebayashi, K. Asai, T. Mitsui, and M. Matsumura, "Preparation of S-doped TiO2 photocatalysts and their photocatalytic activities under visible light," *Applied Catalysis A: General*, vol. 265, no. 1, pp. 115–121, Jun. 2004, doi: 10.1016/j.apcata.2004.01.007.

[162] Y. Park, W. Kim, H. Park, T. Tachikawa, T. Majima, and W. Choi, "Carbon-doped TiO2 photocatalyst synthesized without using an external carbon precursor and the visible light activity," *Applied Catalysis B: Environmental*, vol. 91, no. 1–2, pp. 355–361, Sep. 2009, doi: 10.1016/j.apcatb.2009.06.001.

[163] R. Rescigno *et al.*, "Photocatalytic activity of P-doped TiO2 photocatalyst," *Photochem Photobiol Sci*, vol. 22, no. 6, pp. 1223–1231, Jun. 2023, doi: 10.1007/s43630-023-00363-y.

[164] W. Yu *et al.*, "Enhanced visible light photocatalytic degradation of methylene blue by F-doped TiO2," *Applied Surface Science*, vol. 319, pp. 107–112, Nov. 2014, doi: 10.1016/j.apsusc.2014.07.038.

[165] A. Purabgola, N. Mayilswamy, and B. Kandasubramanian, "Graphene-based TiO2 composites for photocatalysis & environmental remediation: synthesis and progress," *Environ Sci Pollut Res*, vol. 29, no. 22, pp. 32305–32325, May 2022, doi: 10.1007/s11356-022-18983-9.

[166] C. Montero-Ocampo, J. R. V. Garcia, and E. A. Estrada, “Comparison of TiO2 and TiO2-CNT as Cathode Catalyst Supports for ORR,” *International Journal of Electrochemical Science*, vol. 8, no. 12, pp. 12780–12800, Dec. 2013, doi: 10.1016/S1452-3981(23)13307-4.

[167] L. J. Kusumawardani, Y. Syahputri, A. Apriansyah, and M. Fathurrahman, “TiO2/Zeolite Coal Fly Ash Nanocomposite for Photodegradation of Naphthol Blue Black Dye: Optimization and Mechanism under Visible Light,” *Valensi*, vol. 11, no. 1, pp. 92–104, Jun. 2025, doi: 10.15408/jkv.v11i1.45036.

[168] W. Singsang, P. Suttiwattana, K. Nakaravarayut, N. Prasoetsopha, P. Kongsong, and I. Sittitanadol, “Comparison of Photocatalytic Degradation Performance of TiO2-Polymer Based Composites in Wastewater Treatment,” *Indochin. Appl. Sci.*, vol. 14, no. 2, p. 260765, May 2025, doi: 10.55674/ias.v14i2.260765.